New AlterBBN:

A Code for Big Bang Nucleosynthesis with Light Dark Matter

Espen Sem Jenssen

Thesis submitted for the degree of
Master of Science in Astronomy

Institute of Theoretical Astrophysics
University of Oslo

June 1, 2016

Abstract

The universe is full of stuff we cannot see, neither directly or indirectly. We do not understand the nature of the mysterious dark matter and how it interacts with normal matter. Big Bang Nucleosynthesis (BBN) provides one of the major evidences for the standard model of cosmology, but important questions are yet to be answered. Using known physics we are able to predict most of the light element abundances we observe in the universe today. However, large uncertainties are present, and there is a major discrepancy between the predicted and observed abundance of ^7Li, known as the lithium problem. Moreover, we are confident that the standard model of particle physics is not complete. The question is whether or not extensions to this model, and in particular extensions involving the elusive dark matter, may alter the conditions during BBN. With high precision observations we need high precision predictions, thus the task of predicting the primordial element abundances relies heavily on precisely measured reaction rates and accurate numerical modeling.

In this thesis I present an updated AlterBBN, a public available code for predicting the light element abundances with percentage precision. It has been modified to include generic dark matter candidates, and I analyze the effect of light WIMPs with a non-vanishing constant chemical potential. The general trend of the results is an increase in the ^7Li abundance, extending the gap between the predicted and observed value, as well as an increased favoring of neutrino coupled WIMPs compared to previous studies where the chemical potential have been neglected. I have also made additional changes to the code, including an extension of the nuclear network and an update of six important reaction rates. This have lowered the deuterium yield by $\sim 4.5\%$, now being $2.456 \pm 0.057 \cdot 10^{-5}$, but still within the presently suggested observational constraint. Also here we see an increase in the ^7Li abundance.

Finding accurate estimates on the primordial abundances from an observational point of view is not a trivial task. The elements have evolved since BBN ended, as they have been produced and destroyed in stars and other astrophysical processes. The primordial deuterium abundance is an important tracer for the conditions during BBN, and we are able to obtain precise estimates of it by analyzing absorption features in gas clouds in the line of sight to distant quasars. However, extrapolating back to zero metallicity imposes systematic uncertainties, and for a statistically significant estimate we need many measurements. Using the Absorption LIne Software *ALIS* I have conducted a measurement of the deuterium abundance, based on an analysis of the absorption system towards the quasar *Q1009+2956* at redshift $z = 2.407$. This is an ongoing process and is yet to be finished. I present in this thesis the present status of the work, as well as a *PYTHON* program I have written as an add-on to *ALIS*. This program creates composite spectra and models for a better representation of the results from *ALIS*, compared to its inbuilt plotting environment.

Contents

Introduction

Despite observational evidence for the existence of dark matter, we do not know its identity. It has been intensively searched for in direct detection experiments (like Xenon and LUX), particle accelerators (LHC) and gamma rays (Fermi telescope), but without success. A new approach is to study the effects of dark matter candidates on the chemical abundances from the Big Bang Nucleosynthesis (BBN). Primordial nucleosynthesis provides the earliest test of the standard model of particle physics, and serves as a potential window on non-standard physics. In a brief window of time substantial amounts of the lightest elements like ^2H, ^4He, ^3He and ^7Li were produced by nuclear fusion reactions. By comparing predictions of the primordial abundances with observations we are able to probe the conditions in the universe around the time of BBN, which may hint to new physics.

Early on, the total energy density of universe was dominated by that in the relativistic species. The standard model of cosmology suggests that $\sim 69\%$ of the universe is made up by dark energy, $\sim 26\%$ dark matter, with the remaining $\sim 5\%$ being luminous matter [1]. The dark matter is in the most popular models considered to be non-relativistic at the time of BBN. Moreover, at the relevant times, the dark energy contribution to the total energy density is suppressed by that of the relativistic particles. However, the presence of a very light dark matter particle is not ruled out, and the idea is that if such a particle has a relativistic nature at the time of BBN, it will affect the production of the light elements. As well as contributing to an increased energy density, the particle may annihilate during BBN and, depending on their coupling to the standard model particles, heat the neutrinos or the photons and the $e^{\pm}$-pairs. Our approach is to include four generic types of WIMPs to *AlterBBN*, which are real and complex scalars, as well as Majorana and Dirac fermions. In chapter 3 we discuss the effect that the different WIMP types will have on the relic abundances of the light elements, which also depend on their mass (relativistic nature) as well as their coupling to the standard model particles. The textbook assumption of a vanishing chemical potential for the dark matter particles is also investigated by allowing for a constant value of the degeneracy parameter $\phi_\chi \equiv \mu_\chi / T$. Before we get there I present an introduction to the basic physics relevant for BBN in chapter 1, followed by a review of *AlterBBN* and a discussion of the changes and updates made to the program in chapter 2, which goes beyond the implementation of new physics.

In theory, each of the light elements produced during BBN may be used as a probe of the baryon density, which we are able to predict to less than one percent accuracy through observations of the Cosmic Microwave Background (CMB). In practice however, as we will discuss in chapter 1.2, deuterium is by far the best baryometer and thus the main focus of BBN research. There are no known sources of significant deuterium production in the universe. Any measurement of it will therefore serve as a lower bound on the relic abundance from the BBN. Its abundance is measured in metal-poor absorption clouds in the line of sight to distant quasars. In chapter 4 I discuss the work I have conducted in analyzing such an absorption system, not yet arriving at a good estimate. The model fitting is done using the Absorption LIne Software (*ALIS*), written by R. Cooke [2]. As an attempt to improve the representation of the results from *ALIS* I have written a *PYTHON* program for stacking the data from different observations and the model fits for each of them, discussed in chapter 4.1 together with a short introduction to *ALIS*.

Chapter 1

Probing the BBN

Ever since the discovery of "an excess antenna temperature at $\lambda = 7.3\ cm$", made by Arno Penzias and Robert Wilson in 1965 [3] and explained in terms of the Cosmic Microwave Radiation (CMB) by Dicke, Peebles, Roll and Wilkinson the same year [4], the prevailing cosmological model describing the universe from its earliest moments through its subsequent large scale evolution is the Big Bang Theory. It is capable of describing the expansion of the universe, the observation and measurement of the CMB [5], observations of galaxy formation and evolution (e.g. [6]), and the distribution of large-scale cosmic structures (e.g. [7]). Moreover, it predicts the post-BBN abundances of the lightest elements produced in observationally accessible amounts. These elements primarily include deuterium (^2H), helium-4 (^4He), helium-3 (^3He), lithium-7 (^7Li), but also small traces of tritium (^3H), lithium-6 (^6Li) and beryllium-7 (^7Be).

Prior to the recombination period at ~ 380 000 years after the Big Bang, the universe was opaque due to the interplay between photons and electrons by Thompson scattering. For this reason we cannot directly observe any of the physical processes governing the very early universe. Instead, we must rely on CMB measurements to indirectly observe the conditions at the earliest times, as well as simulations of the physical processes, using both known and hypothesized physics. Joint analyses can constrain important parameters, and are used to probe new physics by for example including dark matter candidates or sterile neutrinos in the simulations and comparing with the results from the CMB. The European Space Agency's *Planck Surveyor* satellite was launched in May 2009 and scanned the microwave and sub-millimeter sky continuously between 12 August 2009 and 23 October 2013. In February 2015, ESA and the *Planck* Collaboration released the latest set of results based on data from the entire *Planck* mission. The results are given in 28 separate papers, all available at their website [1]. An overview of the data and results are given in ref. [5], while ref. [1] provides all results concerning the cosmological parameters [2].

The prediction of the light element abundances is made from one of the major implications of the Big Bang Theory; the universe once had to be much smaller than today, a hot and dense soup consisting of radiation and elementary particles, quickly cooling due to the universal expansion. For our purpose we do not have to start the discussion at the earliest times. After all the forces had separated, and protons and neutrons started popping in and out of existence, the combination of high temperature and density ensured that the collision rates were high enough to make sure that thermodynamic equilibrium was established among the key BBN constituents: neutrinos, $e^{\pm}$ pairs, photons and nucleons (protons and neutrons) [8], and possibly unknown weakly interacting particles. Exotic particles interacting only

---

[1] http://www.cosmos.esa.int/web/planck/publications#Planck2015

[2] There are several sets of values given for the cosmological parameters in this reference, emerging from different likelihood estimation involving differing number of variables. For the parameters that are listed in table 4 in the Planck paper, I have consistently used the column corresponding to the *TT+lowP+lensing* analysis.

gravitationally with these constituents must be tracked separately.

In a narrow window of cosmic time the conditions were just right for hydrogen (protons) to fuse into helium, creating small amounts of other elements in the process. Figure 1.1 shows the evolution of the light element abundances in the first $\sim 10^4$ seconds, and we see that most of the action happened in a brief time interval from a couple of minutes to ~ 20 minutes into the history of the universe. Apart from the unstable elements ^3H and ^7Be decaying into ^3He and ^7Li respectively, the resulting element abundances stayed basically unchanged until the onset of the first galaxies and stars several hundreds thousands of years later. Elements heavier than ^9Be was not created in significant amounts before stars started to synthesize elements on their own, due to the bottlenecks at atomic mass numbers $A = 5$ and $A = 8$ (see next section). The abundances predicted from BBN depends on the temperature, nucleon density, neutrino content, neutrino-anti-neutrino asymmetry, the universal expansion rate and possible new physics, and are largely independent of the processes that established them. The thermodynamic equilibrium between all the BBN-relevant constituents therefore serves as an excellent starting point for BBN calculations. [8].
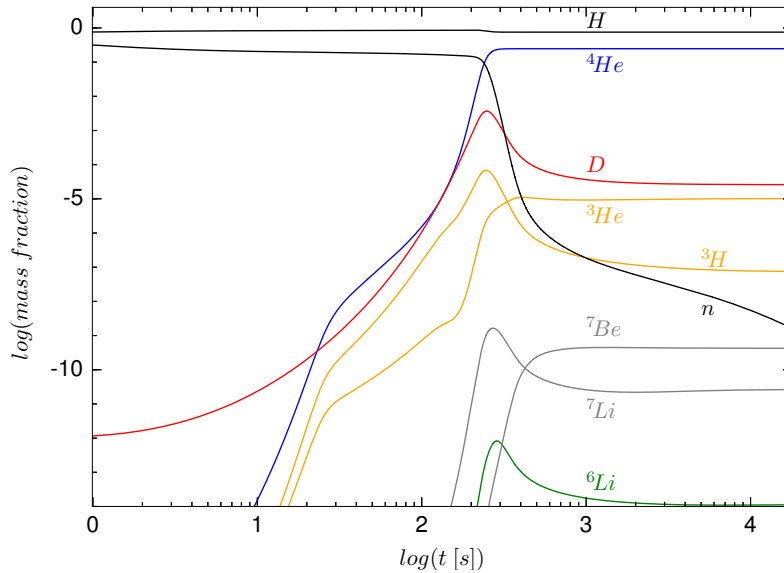
Figure 1.1: *Evolution in time of the light element abundances for the most abundant nuclides during BBN. The plot is the result from an AlterBBN run with the Standard Big Bang Nucleosynthesis (SBBN) parameters $\eta_{10} = 6.10$, $\tau_n = 880.3$ and $N_{\text{eff}} = 3.046$ (see later discussion of these parameters).*

BBN may tell us a lot about both the known and yet unknown physics of the early universe. It can test the standard models of cosmology (section 1.1.2) and particle physics (section 1.1.1) and constrain their parameters, as well as serving as a window on new physics. The primordial abundances of the lightest elements is very sensitive to the conditions in the early universe, which may be altered by the presence of non-standard particles and/or processes. This chapter will introduce the basic BBN physics, and what we may learn from the different element abundances. In addition, a quick overview of the present observational data and how it is obtained will be presented.

1.1 Introduction to BBN Physics

As mentioned, we do not have to start our discussion at the very beginning; describing the unification of the forces, the inflationary period or the transition from a pure energy-filled universe to the creation of particles due to their interaction with the Higgs field, giving them mass. Our discussion starts as thermodynamic equilibrium has been established among the standard model particles relevant for the physics concerning BBN, soon after the "freeze-out" of the total baryon abundance. At temperatures between $\sim 1\ GeV$ and a few hundred MeV, protons and neutrons formed through pair production of particles-antiparticles, but immediately annihilated. Due to not yet fully understood mechanisms, instabilities in the pair production process led to an excess of particles over anti-particles (see e.g. [9]). As the universe reached a temperature of $\sim 0.4\ GeV$ this pair production gradually stopped, and all particles/anti-particles annihilated except for the small excess of particles, which makes up all the baryons in the universe. The universe now consisted of radiation and particles in the form of photons, hadrons and ultra-relativistic leptons, possibly accompanied by yet unknown particles.

In the standard model of cosmology we subsume the standard model of particle physics to describe the constituent particles in the primordial plasma and the forces acting between them. In the next section we will briefly discuss the basics of the standard model of particle physics, followed by the basic features of the standard model of cosmology, as well as the simplest extensions to this. Extensions involving dark matter will be discussed in chapter 3.

1.1.1 The Standard Model of Particle Physics

Figure 1.2 shows a table of all the particles that makes up the standard model of particle physics. They are divided into three families, vertically arranged, so that the up- and down quark, the electron and the electron neutrino makes up family I, the charm- and strange quark, the muon and the muon neutrino makes up family II, and the top- and bottom quark, the tau and the tau neutrino makes up family III. The gluon is the mediator of the strong nuclear force, confining quarks into hadrons, and keeping nuclei together in atoms. The photon is the transmitter of the electromagnetic force, and is the main contributor to the total energy of the radiation dominated early universe. Weak nuclear interactions are caused by the emission or absorption of Z and W bosons, which is the source of radioactive decay. The Higgs boson, discovered in 2012 by the ATLAS and CMS experiments at CERN's Large Hadron Collider [10], is the quantum excitation of the Higgs field, permeating the whole universe. Due to the huge masses of the family II and III particles (with the exception of the neutrinos) they decay into lighter particles at temperatures corresponding to their rest mass. Thus, at times earlier than relevant to our discussion all the charm-, strange-, top- and bottom quarks decayed into up- and down quarks. That is why we don't see much of these particles in our universe today. They can only be created in high energy collisions, such as those involving cosmic rays and in particle accelerators, only to decay very rapidly.

Hadrons are a common description of all particles made up of quarks, which are held together by the strong nuclear force. They are sub-categorized into baryons, which are made up of three quarks, and mesons, which are made up of one quark and one anti-quark. The mesons are bosons (integer spin) and include pions and kaons, and they are all unstable, with the longest-lived lasting for a few hundredths of a microsecond. The baryons are fermions (half-integer spin) and consists of protons and neutrons. Baryons with other quark-arrangements have been hypothesized, and in July 2015 the LHCb collaboration claimed to have discovered two types of pentaquarks [11], which has an extra quark-anti-quark pair. The only stable baryon in a free state is the proton (and the anti-proton), while the neutron is stable only when bound within atomic nuclei. Free neutrons have an average life-time of 880.3 seconds [12]. This number is crucial for the abundances of the elements produced during BBN, in particular the relic helium abundance, in the way that it controls the number of neutrons available for the production of atomic nuclei. Later in this chapter, in section 1.1.2 we will discuss this in more detail.
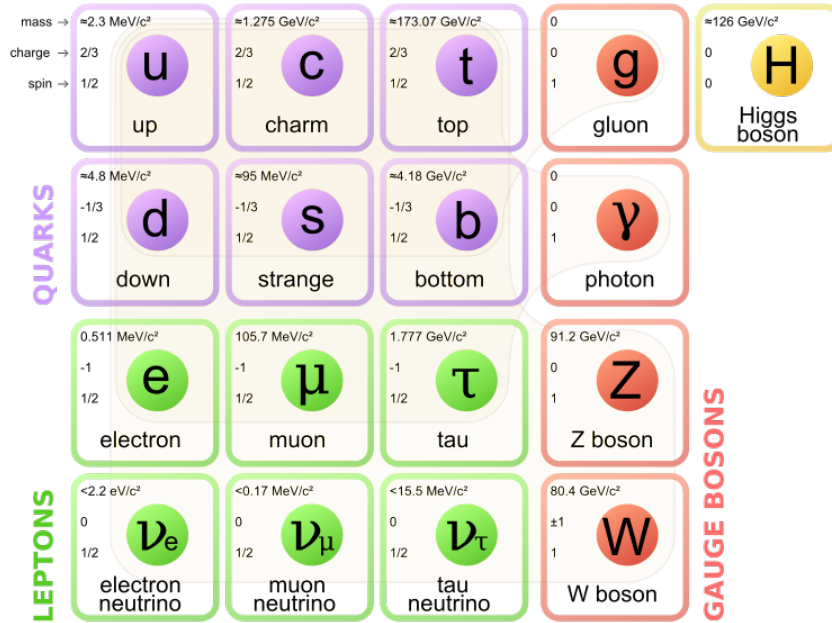
Figure 1.2: Particles of the standard model of particle physics. Source: Wikipedia

The leptons are elementary particles, all fermions, and are sub-categorized into charged leptons (electron-like leptons) and neutral leptons (neutrinos). The charged leptons consists of the electron (e^-), the muon (μ^-) and the tau (τ^-), along with their antiparticles, where the anti-electron (e^+) is called a positron. The electron is the lightest of the three charged leptons, whose masses are arranged as $m_e < m_\mu < m_\tau$. The standard model of physics describes three neutrino species which are all considered massless, despite the fact that observed neutrino oscillations require that at least two of the species must have a non-zero mass [13]. The three neutrino species are the electron neutrino (ν_e), the mu neutrino (ν_μ) and the tau neutrino (ν_τ), and even though we know from experiments that at least two of the flavors need to have a small mass, we do not know which of them that are massive [14]. The neutrino masses stated in figure 1.2 are therefore only experimentally inferred upper limits. Additionally, recent experiments in both particle physics and cosmology indicates that there could be more than three neutrino species. Although we know that the standard model neutrinos only interact through the weak force (except from the gravitational interaction from the massive neutrinos), some experiments have been conducted that allow, or even prefer the existence of neutrinos that do not interact through the weak force (see e.g. [14]). Such hypothetical particles are called sterile neutrinos, and we will discuss those in detail in chapter 3.

For a more extensive discussion of the standard model of particle physics and popular extensions to it, see the 2014 release of the Particle Data Group's booklet [12], or visit their web-page for the latest updates (link found in the reference).

1.1.2 The Standard ΛCDM Model of Cosmology

Our current best description of the universe is based upon the assumption of the *cosmological principle*. The cosmological principle states that the universe is the same in every location (homogeneous) and in every direction (isotropic), viewed on large enough scales, and that the same physical laws apply everywhere in the universe. On scales compared to the size of galaxies and galaxy clusters ($\lesssim 10\ Mpc$) the universe is obviously not homogeneous and isotropic. On such scales matter is not uniformly distributed, rather collected in structures of varying masses and sizes. In this context, "large enough scales" thus means scales much larger than the size of super-clusters (several hundred Mpc). With the improvement

in measurements of the CMB anisotropies there have recent years been claims that the universe actually may have a preferred axis (see e.g. [15]), casting doubt about the assumption of isotropy. For now, however, our current best understanding of the universe relies on the assumption of the cosmological principle.

The large scale dynamics of the cosmos is described by Einsteins general theory of relativity, which relates the geometry of the universe with its matter and energy content. A wide analytic discussion of this theory is out of the scope of this project, but see e.g. the book "The Early Universe" by *Kolb* and *Turner* [16] for a nice review of the topic. The book covers most of the basic physics governing the early universe, and has been used as a reference throughout this chapter. For an even more extensive analysis of Einstein's general theory of relativity, as well as other topics of interest, see references therein. In this discussion it suffices to merely state the Einstein field equations, which may be contracted into the tensor equation

$$G_{\mu\nu} \equiv R_{\mu\nu} - \frac{1}{2}Rg_{\mu\nu} = -\frac{8\pi G}{c^4}T_{\mu\nu} + \Lambda g_{\mu\nu} \, , \tag{1.1}$$

where $G_{\mu\nu}$ is the Einstein tensor and $g_{\mu\nu}$ is the metric of choice. $R_{\mu\nu}$ is the Ricci tensor and R the Ricci scalar, while $T_{\mu\nu}$ is the energy-momentum tensor (including shear- and stress-forces) for all fields present (matter, radiation etc.). The last term, Λ is the cosmological constant, and concerns the vacuum energy of space. This was originally introduced by Einstein to allow for a universe that is not expanding or contracting, since the accepted cosmological model at the time was that of a static, *steady state* [17] universe. As it was realized that this model actually would lead to an unstable universe, Einstein called the cosmological constant "the blunder of his life". Since then, observations suggest that the universe is expanding in an accelerating rate, which was considered proved with the discovery of a supernova type Ia in 1998 [18]. This requires a positive value of the Λ-term in Einstein's field equations, thus being an essential part of the ΛCDM model. If we model the matter and energy in the universe by a perfect fluid, we find for the zero component of the conservation of the energy-momentum tensor ($\nabla^\mu T_{\mu\nu} = 0$)

$$\frac{\dot{\rho}}{\rho} = -3(1 + w)\frac{\dot{a}}{a} \, , \tag{1.2}$$

where the dot means the time-derivative of the variable, and the equation of state

$$P = w\rho c^2 \tag{1.3}$$

is assumed, which is true for essentially all perfect fluids relevant to cosmology [19]. Its most relevant values are

$$w = \begin{cases} 0 & \text{for matter energy} \\ \frac{1}{3} & \text{for radiation energy} \\ -1 & \text{for vacuum energy} \, . \end{cases}$$

Integrating the equation for energy conservation (equation 1.2) yields

$$\rho \propto a^{-3(1+w)} \, , \tag{1.4}$$

which leads to $\rho \propto a^{-3}$ in a matter-dominated universe, $\rho \propto a^{-4}$ in a radiation-dominated universe, and $\rho \propto const.$ in a universe dominated by vacuum energy.

The geometric properties of a spacetime with homogeneous and isotropic spatial parts that can be time-dependent are described by the *Friedmann-Robertson-Walker* (FRW) metric. Written in spherical coordinates, this metric may be expressed as [16] [3]

$$ds^2 = -c^2dt^2 + a^2(t)\left[\frac{dr^2}{1 - kr^2} + r^2\left(d\theta^2 + \sin^2\theta d\phi^2\right)\right] \, , \tag{1.5}$$

---

[3] Note the difference in sign convention between the reference and this work. In the reference, a *timelike* sign convention is used while here, a *spacelike* sign convention is used.

where (t, r, θ, ϕ) are the comoving spacetime coordinates (t is the proper time), and k is a constant representing the curvature of the space, which has one of the values $(-1, 0, 1)$ (negative-, zero-, positive curvature). All of the time dependence enters through the scale factor $a(t)$, which describes the expansion evolution of the universe. The metric applies to any metric theory of gravity, not just general relativity, and is deduced purely on the assumptions of a homogeneous and isotropic universe. It provides an exact solution to Einstein's field equations, yielding the *Friedmann* equations [16]

$$\left(\frac{\dot{a}}{a}\right)^2 = \frac{8\pi G}{3}\rho - \frac{kc^2}{a^2} \qquad\qquad \text{First Friedmann eq.} \qquad (1.6)$$

$$\frac{\ddot{a}}{a} = -\frac{4\pi G}{3}\left(\rho + 3\frac{P}{c^2}\right) \qquad\qquad \text{Second Friedmann eq. ,} \qquad (1.7)$$

where ρ and P is the total energy density and pressure respectively, including the contribution from the cosmological constant, which we from now on will call dark energy. It is convenient to parameterize the expansion of the universe in terms of the *Hubble parameter* $H \equiv \dot{a}/a$. Its present epoch value is $H_0 = 100h \ km \ s^{-1} \ Mpc^{-1}$, where h is known as the "unit-less" Hubble parameter. The present best estimate of this parameter comes from the *Planck 2015 results* [1] and is given as 0.6781 ± 0.0092 (1σ [4]). The critical density is the density which gives a zero curvature k:

$$\rho_{\text{cr}} = \frac{3H^2}{8\pi G} , \qquad (1.8)$$

with a present day value of $\rho_{\text{cr},0} \approx 1.88 \cdot 10^{-29} \ g \ cm^{-3}$. It is also useful to introduce the density parameter $\Omega \equiv \rho/\rho_{\text{cr}}$, which measures the density relative to the critical density. We may then write the first Friedmann equation as

$$\Omega - 1 = \frac{k}{H^2 a^2} , \qquad (1.9)$$

which enables us to make the following distinctions:

$$\rho < \rho_{\text{cr}} \leftrightarrow \Omega < 1 \leftrightarrow k = -1 : \text{open universe}$$
$$\rho = \rho_{\text{cr}} \leftrightarrow \Omega = 1 \leftrightarrow k = 0 \ \ : \text{flat universe}$$
$$\rho > \rho_{\text{cr}} \leftrightarrow \Omega > 1 \leftrightarrow k = +1 : \text{closed universe}$$

Observations suggest that the universe is close to flat. The *Planck 2015 results* [1] states that the curvature density parameter $\Omega_k = -0.005^{+0.016}_{-0.017}$. In the ΛCDM model it is therefore assumed that $\Omega_k = k = 0$, and the Friedmann equation becomes

$$H^2 \equiv \left(\frac{\dot{a}}{a}\right)^2 = \frac{8\pi G}{3}\rho \qquad (1.10)$$

$$= H_0^2 \left((\Omega_b + \Omega_{\text{DM}})a^{-3} + \Omega_R a^{-4} + \Omega_\Lambda\right) . \qquad (1.11)$$

In the last equality the equation is written out in terms of the density parameter for each field, where Ω_b, Ω_{DM}, Ω_R and Ω_Λ is the density parameter for baryons, dark matter, relativistic constituents (radiation) and vacuum energy (dark energy) respectively. In the early universe, a is very small, and we can see that the radiation term dominates over the other terms. This is why we may neglect the contribution from dark energy and non-relativistic matter to the total energy density in BBN calculations. Well before the epoch of recombination, but long after the times relevant for BBN, the non-relativistic matter term "caught up" with the radiation term and the universe became matter-dominated. In the present epoch, dark energy dominates the energy density budget, meaning the universe is undergoing accelerated expansion, and the radiation term have become insignificant. According to the *Planck 2015 results* [1] we now estimate

$$\Omega_{b,0} = 0.0484^{+0.0019}_{-0.0018} , \qquad \Omega_{\text{DM},0} = 0.2579^{+0.0116}_{-0.0111} , \qquad \Omega_{\Lambda,0} = 0.6920 \pm 0.0120 , \qquad (1.12)$$

---

[4] 1σ corresponds to a 68.3% level of statistical confidence. Another commonly used measure of statistical confidence is 2σ, which corresponds to a 95.5% confidence level.

for the present day values of the density parameters, which we see add up to 1 within the stated uncertainties (photons contribute about $\sim 10^{-5}$ today).

As the name suggest, the ΛCDM model assumes the dark matter content to be *cold* (non-relativistic at the time of dark matter decoupling). It does not say that *all* dark matter is cold, merely that most of the non-luminous mass in the universe is the form of relatively heavy, possibly supersymmetric particles. Later, in chapter 3 we will discuss different types of dark matter, and look into the possibility that some of the missing matter may be in the form of lighter particles that where relativistic or semi-relativistic at the time of BBN, which may have affected the light element production.

1.1.3 Equilibrium Thermodynamics

In order to understand the dynamics of the universe and the interplay between its contents during BBN it is necessary to cover some key aspects of statistical physics. As previously mentioned, we start our BBN discussion at the time when we can consider all the key BBN constituents being in thermodynamic equilibrium (see beginning of this chapter). This means that for all particles, the interaction rate Γ is much higher than the expansion rate ($\Gamma \gg H$), and there is no net energy flow, meaning all particles share the same temperature. It also requires that the particles maintain *chemical equilibrium*, which means that the sum of the chemical potentials of reacting particles equals the sum of the chemical potentials of the products. For example, $e^{\pm}$ pair production happens through the reaction

$$e^- + e^+ \longleftrightarrow \gamma + \gamma \,. \tag{1.13}$$

Chemical equilibrium then implies that there are no net production of electrons over positrons and that their chemical potentials are related through $\mu_{e^-} = -\mu_{e^+}$. Since the number of photons is not conserved (e.g. double Compton scattering $e^- + \gamma \longleftrightarrow e^- + \gamma + \gamma$ happens in equilibrium at high temperatures) we know that $\mu_\gamma = 0$.

The plasma equilibrium statistics is given by the Fermi-Dirac (fermions) and Bose-Einstein (bosons) distribution functions, which tells us what fraction of the particles is in a state with momentum **p** at a given temperature T, and is given by [16]

$$f_i(\mathbf{p}) = \frac{1}{\exp\left[(E_i(p) - \mu_i)/(k_B T)\right] \pm 1} \,, \tag{1.14}$$

where μ_i is the chemical potential of particle i, the plus sign is for fermions (half-integer spin), and the minus sign is for bosons (integer spin). $E_i = \sqrt{\mathbf{p}^2 c^2 + m_i^2 c^4}$ is the energy, and m_i the rest mass of the particle. Since $E_i(p)$ depends only on $p = \sqrt{\mathbf{p}^2}$ we can write $f_i = f_i(p)$. Noting that $E_i dE_i = c^2 p dp$ and that $p^2 = (E_i - m_i^2 c^4)/c^2$ we can calculate the equilibrium properties of the plasma [16]:

$$n_i = \frac{g_i}{(2\pi\hbar)^3} \int f_i(p) d^3 p$$
$$= \frac{g_i}{2\pi^2 (\hbar c)^3} \int_{m_i c^2}^{\infty} \frac{(E^2 - m_i^2 c^4)^{1/2} E dE}{\exp\left[(E - \mu_i)/(k_B T)\right] \pm 1} \tag{1.15}$$

$$\rho_i c^2 = \frac{g_i}{(2\pi\hbar)^3} \int E_i(p) f_i(p) d^3 p$$
$$= \frac{g_i}{2\pi^2 (\hbar c)^3} \int_{m_i c^2}^{\infty} \frac{(E^2 - m_i^2 c^4)^{1/2} E^2 dE}{\exp\left[(E - \mu_i)/(k_B T)\right] \pm 1} \tag{1.16}$$

$$P_i = \frac{g_i}{(2\pi\hbar)^3} \int \frac{p^2}{3 E_i(p)} f_i(p) d^3 p$$
$$= \frac{g_i}{6\pi^2 (\hbar c)^3} \int_{m_i c^2}^{\infty} \frac{(E^2 - m_i^2 c^4)^{3/2} dE}{\exp\left[(E - \mu_i)/(k_B T)\right] \pm 1} \,. \tag{1.17}$$

In the ultra-relativistic limit ($m_i c^2 / k_B T \ll 1$), assuming a zero chemical potential, the equations may be approximated by [16]

$$n_i = \frac{g_i \zeta(3)}{\pi^2} \left(\frac{k_B T}{\hbar c} \right)^3 \times \begin{cases} 1 & \text{for bosons} \\ \frac{3}{4} & \text{for fermions} \end{cases} \tag{1.18}$$

$$\rho_i c^2 = \frac{g_i \pi^2}{30} \frac{(k_B T_i)^4}{(\hbar c)^3} \times \begin{cases} 1 & \text{for bosons} \\ \frac{7}{8} & \text{for fermions} \end{cases} \tag{1.19}$$

$$P_i = \frac{1}{3} \rho_i c^2 \quad \text{for fermions and bosons} \tag{1.20}$$

where $\zeta(3) = 1.20206...$ is the Riemann zeta function of 3, and g_i is the internal degrees of freedom for particle i, which is $g_\gamma = 2$ for photons, $g_e = 2$ for both electrons and positrons, and $g_\nu = 2 N_\nu$ for neutrinos. Since the photons are still with us at the present epoch it is useful to express the equations in terms of the photon temperature. For the energy density this leads to

$$\rho_i c^2 = \frac{\pi^2}{30} g_* \frac{(k_B T)^4}{(\hbar c)^3} \,, \tag{1.21}$$

where

$$g_* = \sum_{i=\text{bos.}} g_i \left(\frac{T_i}{T} \right)^4 + \frac{7}{8} \sum_{i=\text{ferm.}} g_i \left(\frac{T_i}{T} \right)^4 \tag{1.22}$$

is the *effective number of relativistic degrees of freedom.*

Approximations in the non-relativistic limit yields [16]

$$n_i = g_i \left(\frac{m_i k_B T}{2 \pi \hbar^2} \right)^{3/2} \exp \left(\frac{\mu_i - m_i c^2}{k_B T} \right) \tag{1.23}$$

$$\rho_i c^2 = n_i m_i c^2 \tag{1.24}$$

$$P_i = n_i k_B T \ll \rho_i c^2 \,, \tag{1.25}$$

where the latter equations justifies our use of $P = 0$ as the equation of state for non-relativistic matter. We note that the number density, energy density and pressure of a non-relativistic particle become exponentially suppressed compared to that of the relativistic species as the temperature drops below the mass of the particle. We interpret this as the annihilation of particles and anti-particles. At higher temperatures these annihilations also occur, but they are balanced by pair production.

Some particles present in the early universe are at the borderline between relativistic and non-relativistic (e.g. $e^\pm$-pairs and hypothetical WIMPs). More accurate approximations in this limit are obtained by using modified Bessel functions, and the derivation of those can be found in appendix C.

1.1.4 Entropy

For a system in thermodynamic equilibrium the *entropy per co-moving volume*, given by (see e.g. [16] for derivation)

$$S = \frac{a^3 (\rho c^2 + P)}{T} \,, \tag{1.26}$$

is conserved. Here we have taken $V = a^3$ to be the volume of the system in thermodynamic equilibrium. The conservation of entropy provides a powerful tool in the case where a particle specie annihilates and

transfers its entropy to the remaining thermodynamic equilibrium plasma. It is useful to introduce the *entropy density*, defined as

$$s = \frac{S}{V} = \frac{\rho c^2 + P}{T} \,.$$

(1.27)

In the early universe the entropy content is dominated by the relativistic species, as in the case of the energy density. Inserting equation 1.21 together with equation 1.20 and normalizing to the photon temperature we get

$$s = \frac{2\pi^2}{45} k_B g_{*s} \left(\frac{k_B T}{\hbar c} \right)^3 \,,$$

(1.28)

where

$$g_{*s} = \sum_{i=\text{bos.}} g_i \left(\frac{T_i}{T} \right)^3 + \frac{7}{8} \sum_{i=\text{ferm.}} g_i \left(\frac{T_i}{T} \right)^3$$

(1.29)

is the *effective number of relativistic degrees of freedom for entropy*. Note that as long as all relevant species are in thermodynamic equilibrium and thus share the same temperature, $g_{*s} = g_*$ (see equation 1.22.

The conservation of entropy per co-moving volume implies that $dS = 0$, thus

$$sa^3 = constant \,,$$

(1.30)

which we also may write as $g_{*s} T^3 a^3 = constant$, and we note that for a fluid in thermodynamic equilibrium $s \propto a^{-3}$.

1.1.5 Chemical Potential

For a system in thermodynamical equilibrium we may apply the thermodynamic identity

$$dU = T\,dS + P\,dV + \mu\,dN \,.$$

(1.31)

This relation describes the change in internal energy in terms of the change in entropy, volume and the number of particles, and is valid for infinitesimal, reversible processes. μ is the chemical potential, and we see that we may define this as being the change in internal energy of the system when one more particle is added, holding the entropy and volume fixed. That is,

$$\mu = \left(\frac{\partial U}{\partial N} \right)_{S,V} \,.$$

(1.32)

For charged particles (or more specifically, for particles that have a conserved charge) the chemical potential is non-zero if the number densities of particles and anti-particles are different. That means that for e.g. electrons/positrons, the chemical potential is a measure of the asymmetry between them. However, for particles that have zero charge (e.g. neutrinos and WIMPs), a non-zero chemical potential does not necessarily imply that there is a degeneracy in the number of particles/anti-particles. In section 1.1.6 we discuss the possibility that there might be a degeneracy among the neutral leptons. Similarly, in chapter 3.3.2 we investigate the implications a non-zero chemical potential for WIMPs may have on the primordial light element abundances. Common for both cases is that we do not have any limitations on the value of the chemical potential, contrary to the degeneracy in the charged lepton sector. In that case, we know that there is a non-zero chemical potential, and that it is limited by the universal charge neutrality.

13

1.1.6 Big Bang Nucleosynthesis

During the Big Bang Nucleosynthesis (BBN) the conditions (temperature and pressure) were just right for nuclear fusions involving protons and neutrons to take place, resulting in the production of the lightest elements. In this section we will discuss the standard model for BBN, and the simplest extensions to it.

Standard Big Bang Nucleosynthesis
The baryon-to-photon-ratio:

Standard Big Bang Nucleosynthesis (SBBN) subsumes the ΛCDM model of cosmology and the standard model of particle physics, which implies three flavors of very light, left-handed neutrinos and their right-handed anti-neutrinos. The only free parameter in SBBN is the baryon density, parametrized through the baryon-to-photon ratio η. It is defined as the ratio between the baryon number density n_b and the photon number density n_γ, as [20]

$$\eta_{10} \equiv 10^{10} \frac{n_b - n_{\bar{b}}}{n_\gamma}, \tag{1.33}$$

where b denotes baryons and $\bar{b}$ anti-baryons. After baryon - anti-baryon annihilation the excess baryons survive and $n_b - n_{\bar{b}} \to n_b$. The factor of 10^{10} is just a matter of convenient scaling, since the ratio of the number densities is of the order of $\sim 10^{-9} - 10^{-10}$. Rewriting n_b in terms of the density parameter, and inserting for today's value of the photon number density (using the CMB measured photon temperature $T_\gamma = 2.725\ K$) the present epoch value of the baryon-to-photon ratio can be written as

$$\eta_{10} = 10^{10} \frac{n_{b,0}}{n_{\gamma,0}} \approx 273.9 \Omega_{b,0} h^2\ , \tag{1.34}$$

where the factor $\Omega_b h^2$ is often denoted by ω_b in the literature. Note that I have dropped the index 0 for η here. Unless stated otherwise, η, or equivalently η_{10}, refers to the present epoch value of the baryon-to-photon ratio. It is common to write the energy density on the form $\Omega_b h^2$ since one can derive a more stringent constraint on ω than the one that follows by using the individual constraints on Ω and h [16]. With the launch of the *Planck Surveyor* in 2009, and the high-quality data it has provided, the best estimates of η now comes from CMB measurements. The presently most up to date value is the 1σ confidence level value of $\omega_b = 0.02226 \pm 0.00023$ [1], leading to $\eta_{10} = 6.10 \pm 0.06$. The *Planck* analysis assumes a specific relationship between the helium abundance and the the baryon density. Cyburt et al. [21] did a marginalization over ω_b and Y_p (the helium mass fraction), finding their covariance and producing likelihood functions for η. Since the ^4He abundance is very weakly linked to the baryon density, the impact of the analysis on Y_p was not significant. However, the uncertainty on η was reduced to ± 0.04, which I have adopted in this project.

We may write the baryon-to-photon ratio as a function of temperature by using conservation of entropy. In a system in thermodynamic equilibrium entropy is conserved, and is thus related to the scale factor through $s \propto a^{-3}$ (equation 1.30). Moreover, there is no net production/destruction of particles so the number of baryons N_b must also be conserved. This means that $N \equiv a^3 n_b \propto n_b/s = constant$. By relating the number density of photons (equation 1.18) to the entropy density in the relativistic species (equation 1.28) we may write the baryon-to-photon ratio for an arbitrary time as

$$\eta(T) \equiv \frac{n_b}{n_\gamma} \approx 1.8 g_{*s}(T) \left(\frac{n_b(T)}{s(T)} \right)\ . \tag{1.35}$$

Since $n_b/s = constant$ we finally arrive at an expression for the baryon-to-photon ratio for a given temperature as a function of its present epoch value:

$$\eta(T) = \frac{g_{*s}(T)}{g_{*s}(T_0)} \eta(T_0)\ . \tag{1.36}$$

The implication of this relation is that the baryon-to-photon ratio changes only when the entropy of the thermal bath changes, that is, when a particle decouples or annihilates. In the standard cosmological scenario we therefore have $\eta(T) = \eta(T_0) = constant$ after $e^\pm$ annihilation.

The neutron-to-proton ratio and the neutron mean lifetime:

Above temperatures around a few MeV ($\sim 3 \cdot 10^{10}\ K$) protons and neutrons are in equilibrium through the charged current weak interactions:

$$\nu_e + n \longleftrightarrow e^- + p$$
$$e^+ + n \longleftrightarrow \bar{\nu}_e + p$$
$$n \longleftrightarrow e^- + \bar{\nu}_e + p. \tag{1.37}$$

Neutrons and protons are now non-relativistic, so we may use equation 1.23 to find the equilibrium ratio between their number densities, yielding

$$\frac{n_n}{n_p} = \left(\frac{m_p}{m_n}\right)^{3/2} \exp\left[-\frac{(m_n - m_p)c^2}{k_B T}\right] \approx e^{-Q/k_B T}, \tag{1.38}$$

where $Q = (m_n - m_p)c^2 \approx 1.293$ MeV. At temperatures $k_B T \gg Q$ the ratio is 1:1, but as the temperature drops, the weak interactions that interconvert neutrons and protons favors neutron decay. When the temperature reaches $\sim 2 - 3$ MeV these weak interactions freeze out, at a point where the neutron-to-proton ratio is $\sim 1/6$. Two-body reactions involving n, p, $e^\pm$, ν_e and $\bar{\nu}_e$ still continue to influence the n/p ratio, although they are not happening at a high enough rate to track the equilibrium value. As the universe enters the nucleosynthesis era the ratio has therefore decreased to $\sim 1/7$ [16]. Since the amount of ^4He produced during BBN by far outnumber the production of heavier elements, essentially all the neutrons entering BBN ends up in ^4He. This means that finding the primordial helium abundance is practically equivalent to finding the number of neutrons in the universe, which is very sensitive to the mean neutron lifetime, one of the key parameters going into BBN calculations.

The neutron lifetime rely on precise experimental measurements, and have historically been a source of frustration for experimentalists, since its value has been very difficult to establish to a high degree of confidence. Since the 1970's the experimentally accepted values have fluctuated wildly in the rather large interval of $877 - 937$ seconds. In the years between 1990 and 2005 the value varied very little, settling at 885.6 ± 0.8. However, recent years have seen a shift towards lower values, and the *Particle Data Group* released in 2014 the currently accepted mean lifetime of 880.3 ± 1.1 seconds (1σ) [12], which is the value I have used in this project. The value is an average of the seven most precise experiments made over the recent years (the average value and a listing of the experiments used to obtain this value is found in [12], while a full review of the experimental methods and results can be found in [22]).

Neutrino decoupling and $e^\pm$ annihilation:

At a temperature around $T \sim 2 - 3$ MeV [23] [24] the weak interactions freeze out and the neutrinos drop out of equilibrium. After decoupling, the neutrino temperature will simply evolve as $T_\nu \propto a^{-3}$, where a is the universal scale factor. This is also true for the photon/$e^\pm$ plasma between the time of neutrino decoupling and $e^\pm$ annihilation. However, when the temperature drops below the electron/positron rest mass energy of 0.511 MeV the $e^\pm$-pairs annihilate and transfer their entropy to the remaining photons. This means that the photons will be heated relative to the decoupled neutrinos [5], and by entropy conservation (equation 1.30) we find that post $e^\pm$ annihilation we have

$$T_\nu = \left(\frac{4}{11}\right)^{1/3} T_\gamma . \tag{1.39}$$

---

[5] Note the use of *relative* here. The temperature of both the neutrinos and photons decrease due to the expansion and cooling of the universe, but the photon temperature decrease *less* than the neutrino temperature at the time the $e^\pm$-pairs annihilate.

Here we have used that after neutrino decoupling, but before $e^\pm$ annihilation, the total entropy is given by the entropy in photons and $e^\pm$-pairs, and after $e^\pm$ annihilation (but before the universe becomes matter dominated) the total entropy is given by the entropy in the photons. It is further assumed that the neutrino decoupling happens instantaneously, and that the electrons/positrons are ultra-relativistic. However, the neutrino decoupling is not an abrupt process, and the electron neutrinos (and anti-neutrinos) continue to interact with the baryons via the charged-current weak interactions until a temperature of ~ 0.8 MeV has been reached. In the standard model of cosmology we assume a universal charge neutrality. This means that the charged lepton asymmetry (the excess of electrons over positrons) is of the same order as the baryon asymmetry, and the surviving electrons equal in number to the surviving protons. Via Compton scattering processes the electrons remain coupled to the photons all the way to photon decoupling at the Last Scattering Surface (LSS), when the temperature is low enough for electrons to bind to atomic nuclei, and the photons start free-streaming, which we observe today as the CMB. Since the decoupling of the neutrinos does not happen instantaneously, some high-energy neutrinos are still in thermodynamic equilibrium with the photons via weak interactions even after $e^\pm$ annihilation, and those are also reheated. Moreover, the temperature is now such that the electrons/positrons are not fully relativistic [23], and these two effects will lead to a slightly higher T_ν.
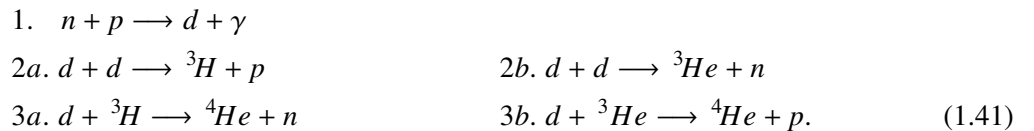
The neutrino sector of particle physics is not yet fully understood, and is one of the possible shortcomings of the standard model. Not only are we unable to determine the masses of the standard model neutrinos, we also do not know if there are more species of neutrinos. In chapter 3 we will encounter the *sterile neutrino*, which is a hypothetical neutrino-like particle that do not take part in the weak interactions, but still have the right properties to affect BBN. Possible light WIMPs might also annihilate after neutrino decoupling, affecting the T_ν/T_γ ratio. To account for additional neutrino species or other effects that may disturb the standard model T_ν/T_γ ratio we use the notion of an *effective number of neutrino species* $N_{\text{eff}} = N_\nu + \Delta N_\nu$, where ΔN_ν is the *equivalent number of neutrinos* $\Delta N_\nu = N_\nu - 3$. In the standard model of cosmology we include only the neutrinos that are part of the standard model of particle physics, thus $\Delta N_\nu = 0$. If we further assume instantaneous neutrino decoupling and ultra-relativistic $e^\pm$-pairs we have $N_{\text{eff}} = N_\nu = 3$. However, the combined effect of a small departure in entropy due to the semi-relativistic nature of the $e^\pm$-pairs (contributes 0.018) and the non-abrupt neutrino decoupling is absorbed into the definition of N_{eff}, leading to [25]

$$N_{\text{eff}} = 3 + \Delta N_\nu \to N_{\text{eff}} = 3.046 + \Delta N_\nu. \tag{1.40}$$

It is important to note that N_{eff} is a late-time quantity, with its value corresponding to the one as measured from the CMB.

Element production:

In heavy stars, helium can be produced by using carbon and other metals as catalysts (e.g. the CNO cycle), avoiding the need to produce deuterium as an intermediate step. However, since such metals were not present in the early universe, and the density was way too low to allow for 3-body reactions to happen, the only way of producing helium was through two-body reaction chains like

$$
\begin{aligned}
&1. \quad n + p \longrightarrow d + \gamma \\
&2a. \ d + d \longrightarrow {}^3H + p \qquad\qquad\qquad 2b. \ d + d \longrightarrow {}^3He + n \\
&3a. \ d + {}^3H \longrightarrow {}^4He + n \qquad\qquad\quad\ 3b. \ d + {}^3He \longrightarrow {}^4He + p.
\end{aligned}
\tag{1.41}
$$

Alternatively, ${}^3He$ can be produced by deuterium fusing with a proton through the reaction $d(p,\gamma){}^3He$, where I have introduced a new notation for describing nuclear reactions. In this description the elements are arranged by atomic number. The comma separates the left and the right hand side of the reaction, while the element with the largest atomic number on each side is found outside the parenthesis. A third way of producing helium goes through the production of ${}^7Li$ from ${}^3H$, and a set of the most relevant BBN reactions can be seen in figure 1.3. Naively, one would think that these reactions would take place as

soon as the mean photon energy was comparable to the binding energy of deuterium, just after protons and neutrons fell out of equilibrium. However, since photons outnumber the baryons by a factor of $\sim 10^9$ there were enough photons in the high-energy tail to photo-dissociate any deuterium produced before reactions like 2a and 2b in 1.41 could take place. Consequently, helium would not be produced until about three minutes after the Big Bang, when the photon temperature had dropped to ~ 0.08 MeV. This is called the "deuterium bottleneck" and had the consequence that the early universe nucleosynthesis was constrained to take place between three and twenty minutes after the Big Bang [8]. Figure 1.3 shows an illustration of the nuclear network for the elements up to ^7Be, where the main reactions involved during BBN are seen. Note that for high precision BBN calculations we need to extend the network to include elements up to $\sim$ oxygen, since occasional nuclear reactions involving heavier elements do occur. Although these elements are not produced in significant amounts they may influence the lighter element production, and extending the network is essential for e.g. ruling out a nuclear fix to the lithium problem (to be discussed in section 1.2).
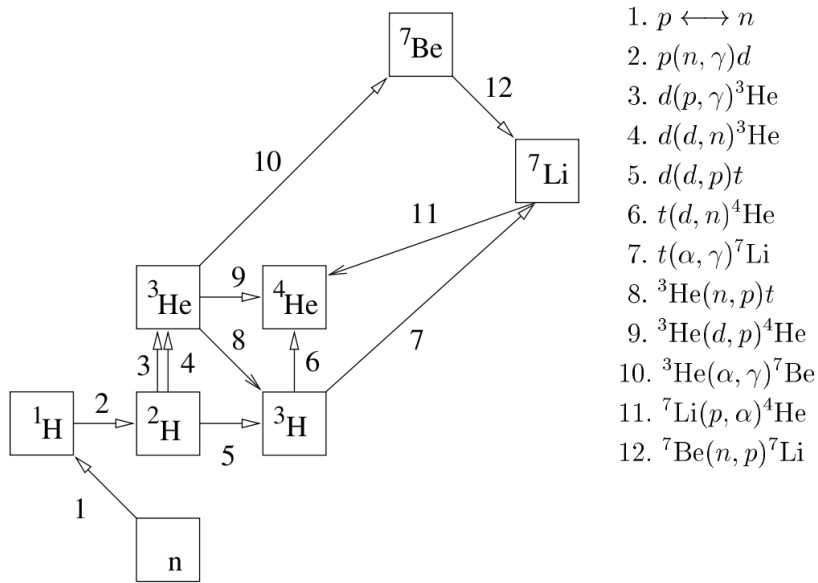

1. $p \longleftrightarrow n$
2. $p(n, \gamma)d$
3. $d(p, \gamma)^3\text{He}$
4. $d(d, n)^3\text{He}$
5. $d(d, p)t$
6. $t(d, n)^4\text{He}$
7. $t(\alpha, \gamma)^7\text{Li}$
8. $^3\text{He}(n, p)t$
9. $^3\text{He}(d, p)^4\text{He}$
10. $^3\text{He}(\alpha, \gamma)^7\text{Be}$
11. $^7\text{Li}(p, \alpha)^4\text{He}$
12. $^7\text{Be}(n, p)^7\text{Li}$

Figure 1.3: Nuclear network of the dominant reactions taking place during BBN. Source: [26]

An approximation of the BBN relic ^4He mass fraction can be obtained by assuming that all available neutrons at the time of BBN end up in ^4He. This is justified by the fact that D and ^3He are produced at the level of about 10^{-5} relative to hydrogen, ^7Li at the level of about 10^{-10} relative to hydrogen, and even less for the rest of the elements. We then have

$$Y_p = \frac{2(n/p)}{1 + (n/p)} \approx 0.25, \tag{1.42}$$

where $n/p = 1/7$ have been used (see discussion of equation 1.38). The reason that most neutrons end up in a helium atom, or more precisely, why helium outnumber the rest of the BBN-produced elements to the degree it does, is that it is the most tightly bound of the light nuclides, and that a new bottleneck appears at ^4He. This bottleneck emerges from the fact that there are no stable mass-5 nuclides, thus very few reactions manage to jump the Coulomb-suppressed mass-5 gap. Those who do, mainly lead to the mass-7 elements ^7Li and ^7Be, where the latter decays into the first with a half-life of 53.22 *days*. This decay is an electron capture process, and will not happen until the universe has cooled even further, at around the start of the recombination epoch [21]. The lack of stable mass-8 nuclides provides yet another Coulomb-suppressed gap, and ensures that insignificant amounts of heavier elements are produced during BBN [8].

Extensions To The Standard Big Bang Nucleosynthesis

Since the universe is radiation dominated at the times of interest, the total energy density in the first Friedmann equation (equation 1.6) may be written in terms of the relativistic species ρ_R, so that $\rho_{\text{tot}} = \rho_\gamma + \rho_{e^-} + \rho_{e^+} + \rho_\nu = \rho_R$. New particles, or generally, new physics, may lead to $\rho_R \to \rho_R'$ (dark radiation) or $G \to G'$ (modified gravity). This results in a deviation from the standard model so that $H \to H'$, which may be parameterized by an expansion rate parameter $\mathcal{S} \equiv H'/H$. Since the total energy density in the early universe is determined by the energy density in relativistic particles, deviations from the standard cosmology ($\mathcal{S} \neq 1$) may equally well be quantified by the equivalent number of neutrinos, so that

$$\rho_R \to \rho_R' \equiv \rho_R + \Delta N_\nu \rho_\nu. \tag{1.43}$$

Prior to neutrino decoupling, photons, $e^\pm$ pairs and neutrinos are in thermodynamic equilibrium, and thus share the same temperature. By combining the expressions for the energy densities with equation 1.43 and assuming that the $e^\pm$-pairs are extremely relativistic and that the equivalent neutrino(s) decouple with the standard model neutrinos, we find that [20]

$$\frac{\rho_R'}{\rho_\gamma} = \frac{43}{8} + \frac{7}{8}\Delta N_\nu = \frac{43}{8}\left(1 + \frac{7\Delta N_\nu}{43}\right). \tag{1.44}$$

Using the Friedman equation 1.6 we can relate the expansion rate factor $\mathcal{S}$ directly to ΔN_ν:

$$\mathcal{S} \equiv \frac{H'}{H} = \left(\frac{\rho_R'}{\rho_R}\right)^{1/2} = \left(1 + \frac{7\Delta N_\nu}{43}\right)^{1/2}. \tag{1.45}$$

It is common to use the effective number of neutrino species N_{eff} to describe deviations from standard cosmology in terms of ΔN_ν, which then becomes a parameterization of anything that would change the expansion rate. In equations 1.44 and 1.45 it is assumed that ΔN_ν only consist of extra neutrinos, that is, fermions with internal degrees of freedom $g = 2$. One sterile neutrino would, for example, contribute $\Delta N_\nu = 1$. In chapter 3 we will discuss N_{eff} in the case of light WIMP candidates that need not have these physical properties. Such contribution of radiation energy from yet unknown sources is commonly dubbed "dark radiation". At late times, e.g. as measured by the CMB, the contributors to the relativistic energy are the photons, the Standard Model (SM) neutrinos, and possible equivalent neutrinos/dark radiation. We first introduced the notion of an effective number of neutrino species in section 1.1.6, and saw that under the assumption of SBBN, but relaxing the assumptions of instantaneous neutrino decoupling and ultra-relativistic $e^\pm$-pairs, we have $N_{\text{eff}} = 3.046$. Although still in agreement with SBBN within the uncertainties stated from CMB measurements (e.g. [1]), there have recent years been indications that both BBN and the CMB favor values of $N_{\text{eff}} > 3.046$ [27], which implies physics beyond the Standard Model of Cosmology.

There might also be an asymmetry among the neutrinos and anti-neutrinos, and unlike the degeneracy in the charged leptons it is not limited by the baryon asymmetry. As η is a measure of the baryon asymmetry, the neutrino asymmetry may be quantified in the same manner: [8]

$$L_{\nu_\alpha} \equiv \left(\frac{n_{\nu_\alpha} - n_{\bar{\nu}_\alpha}}{n_\gamma}\right) = \frac{\pi^2}{12\zeta(3)}\left(\frac{T_{\nu_\alpha}}{T_\gamma}\right)^3 \xi_{\nu_\alpha}\left(1 + \left(\frac{\xi_{\nu_\alpha}}{\pi}\right)^2\right), \tag{1.46}$$

where $\xi_{\nu_\alpha} \equiv \mu_{\nu_\alpha}/k_B T$ is the dimensionless neutral lepton chemical potential, $\zeta(3) \approx 1.202$ is the Riemann zeta function of 3, T_{ν_α} is the temperature of neutrino flavor α and T_γ is the photon temperature. The total neutral lepton asymmetry is thus the sum over all neutrino flavors, that is,

$$L \equiv \sum_{\alpha=e,\mu,\tau} L_{\nu_\alpha}. \tag{1.47}$$

The measured neutrino oscillations indicate that the standard model neutrinos reach approximate chemical equilibrium before a possible degeneracy can affect BBN. This mixing allows us to assume that

$\xi \equiv \xi_{\nu_e} = \xi_{\nu_\mu} = \xi_{\nu_\tau}$ [28]. Any neutrino degeneracy will always have the effect of increasing the energy density in the neutrinos, leading to $\Delta N_\nu > 0$. An estimate found from equating the chemical potentials is [20]

$$\Delta N_\nu(\xi) = \frac{90}{7}\left(\frac{\xi}{\pi}\right)^2\left[1 + \frac{1}{2}\left(\frac{\xi}{\pi}\right)^2\right]. \tag{1.48}$$

This increased energy density will increase the expansion rate of the universe (equation 1.6), but the range of $|\xi|$ of interest to BBN is limited to such small values that any significant effect on the modified expansion rate $\mathcal{S}$ is questionable. A value of $|\xi|$ around unity would drive the observed and predicted abundances of the elements so far apart that it is safe to assume that $|\xi| \ll 1$ (see for example Ichimasa et. al [29])[6]. To illustrate the negligible effect a neutrino degeneracy would have on $\mathcal{S}$, we use equation 1.48 with $|\xi| \lesssim 0.1$ (quite unreasonable high value). This yields $\Delta N_\nu(\xi) \lesssim 0.013$, which is small compared with anticipated uncertainties in ΔN_ν inferred from BBN or the CMB. Although very large compared to the baryon and charged lepton asymmetry, one cannot exclude neutrino degeneracies of the order of $|\xi| \sim 10^{-2}$. This may have a significant impact on the n/p ratio prior to BBN, through the charged current weak interactions, modifying primarily the relic abundance of ^4He [8]. Using observational constraints on the helium-4 abundance one may obtain the allowed 1σ range of [30]

$$-0.008 < \xi_e < 0.013 \,, \tag{1.49}$$

for the electron neutrino asymmetry. In the case of a neutrino degeneracy the n/p equilibrium value is modified to [8]

$$\frac{n_n}{n_p} \approx e^{-Q/k_B T - \xi_e} \,, \tag{1.50}$$

since only the electron neutrinos take part in the charged current weak interactions (see reactions 1.37).

As we learn from the above discussion the relic deuterium abundance is very sensitive to the photon-to-baryon ratio. We saw that this also affects the helium abundance, but only indirectly. In addition, as we discussed, the helium abundance is also very sensitive to the neutron lifetime. This is what makes deuterium the preferred "baryometer". By measuring the relic deuterium abundance we are actually measuring the baryon content in the universe through the photon-to-baryon ratio. The importance of deuterium in BBN studies is discussed in more detail in section 1.2.

1.1.7 Overview

The combined effect of a low temperature (on the order of $10^7\ K$, or ~ 1 keV) and a low energy density and pressure ended the nuclear fusion processes after about twenty minutes of cosmic time, and apart from some unstable elements decaying into others, the production of new elements stopped. The mass-5 and mass-8 bottlenecks, combined with the short time-span of BBN prevented the creation of significant amounts of stable elements heavier than mass-7, and the tight bounding of the helium nuclei ensures that practically all neutrons end up in ^4He. We learned that the n/p ratio sets an important initial condition for BBN, its value being sensitive to essentially every known physical reaction in the early universe. The neutron and proton masses, and consequently Q, are determined by both strong and electromagnetic interactions, while the temperature depends on weak and gravitational interactions. New physics is therefore almost certainly prone to influence the number of neutrons available for nucleosynthesis, primarily affecting the post-BBN helium abundance. Since the BBN departure of n/p from its equilibrium value is given by the competition between the weak interaction rates and the early universe expansion rate, as well as a possible neutrino asymmetry, the BBN relic abundance of helium serves as the most sensitive probe of any departure from the standard model when it comes to $\mathcal{S}$ and ξ_ν. Actually,

---

[6]Constraints for ξ and η from detailed comparison of calculated abundances with the observational data of ^4He and D gave a limiting interval of $-4.6 \cdot 10^{-2} < \xi_{\nu_e} < -0.4 \cdot 10^{-2}$ for $6.02 < \eta_{10} < 6.54$ (2σ)

at present, BBN provides the only window to a neutral lepton asymmetry [20].

With the best estimates of the baryon-to-photon ratio η now coming from CMB measurement, SBBN is effectively a parameter-free theory. In addition to η, the theory relies on precise measurements of the mean neutron lifetime τ_n and the effective number of neutrino species N_{eff}. In table 1.1 I have listed the present most up-to-date estimates of these three important parameters. The observational constraints on N_{eff} will be used in chapter 3, to compare the results from BBN computations where equivalent number of neutrinos and light WIMPs are included.

Parameter	Value	Reference
η_{10} (1σ)	6.10 ± 0.04 *	[1]
N_{eff} (1σ)	3.15 ± 0.23	[1]
N_{eff} (2σ)	3.13 ± 0.62	[1]
τ_n (1σ)	880.3 ± 1.1	[12]

Table 1.1: Present most updated values of the baryon-to-photon ratio η_{10} and the effective number of neutrinos N_{eff} as measured through the CMB, in addition to the adopted average of the mean neutron lifetime τ_n as determined by laboratory experiments. Most CMB-measured values referred to in this project are taken from the TT+lowP+lensing *analysis as summarized in table 4 in the stated reference. This includes the present epoch value of η (found by using the measured value of $\Omega_b h^2$ in combination with equation 1.34). However, the 1σ value of N_{eff} is not stated in any tables, and I will therefore use the value found in the abstract of the paper. The 2σ is taken from the* TT+lensing *analysis summarized in table 5.*
* Error reduced from ± 0.06 by Cyburt et al. [21].

In figure 1.4 we see the effect on the resulting element abundances for D, ^4He, ^3He and ^7Li by changing η. Note that the deuterium abundance is very sensitive to the total baryon abundance, which is related to η through $[D/H]_p \propto \eta_{10}^{-1.6}$ [8]. A higher baryon density results in a more effective burning of D (and ^3He), reducing its primordial abundance. Increasing η also leads to an earlier breaching of the deuterium bottleneck, which means that more neutrons are available for BBN, resulting in an increased ^4He abundance. However, unlike the curves for D, ^3He and ^7Li, the ^4He curve is not plotted logarithmically, and this tells us that the dependence of the ^4He abundance on η is rather weak (close to logarithmically). The dependence of ^7Li (and ^7Be) on η is a bit more involved. As we see from the figure, the ^7Li curve has a "dip" at $\eta_{10} \approx 3.5$, which reflects the two paths to mass-7 nuclei. The direct path to ^7Li through ^3H dominates at low baryon density. The lithium is further synthesized to ^4He, a process that happens more rapidly with increasing baryon density. Hence the decrease of the ^7Li abundance towards higher η for low values of η. However, at even higher η, ^7Be-production dominates the mass-7 budget. Most of the ^7Be is synthesized to ^4He, but some of it survives the BBN. The higher the baryon density, the more ^7Be survives and, as mentioned earlier, ^7Be will later decay into ^7Li, which explains the increase in ^7Li with increasing η, for high values of η.

It is also worth mentioning the effects that a modified expansion rate parameter $\mathcal{S}$ will have on the light element abundances. Adding relativistic energy will increase the expansion rate of universe, and this will leave less time for neutrons to decay into protons, resulting in a higher ^4He relic abundance. It will also shorten the time available for D and ^3He destruction, increasing the post-BBN abundances of these elements. Decreasing the expansion rate, on the other hand, will naturally have the opposite effect. For the mass-7 abundances, the effect of changing the expansion rate will depend on η. Direct production/destruction of ^7Li dominates the mass-7 budget for low η ($\eta_{10} \gtrsim 3$) [8]. A faster-than-standard expansion leads to less destruction of the element, increasing both the ^7Li and the total mass-7 abundance, although there will be produced less ^7Be. For higher η direct production of ^7Be dominates, and most of the contribution to the primordial ^7Li comes from post-BBN decay of ^7Be. A faster-than-standard expansion rate thus leads to both element abundances being reduced.
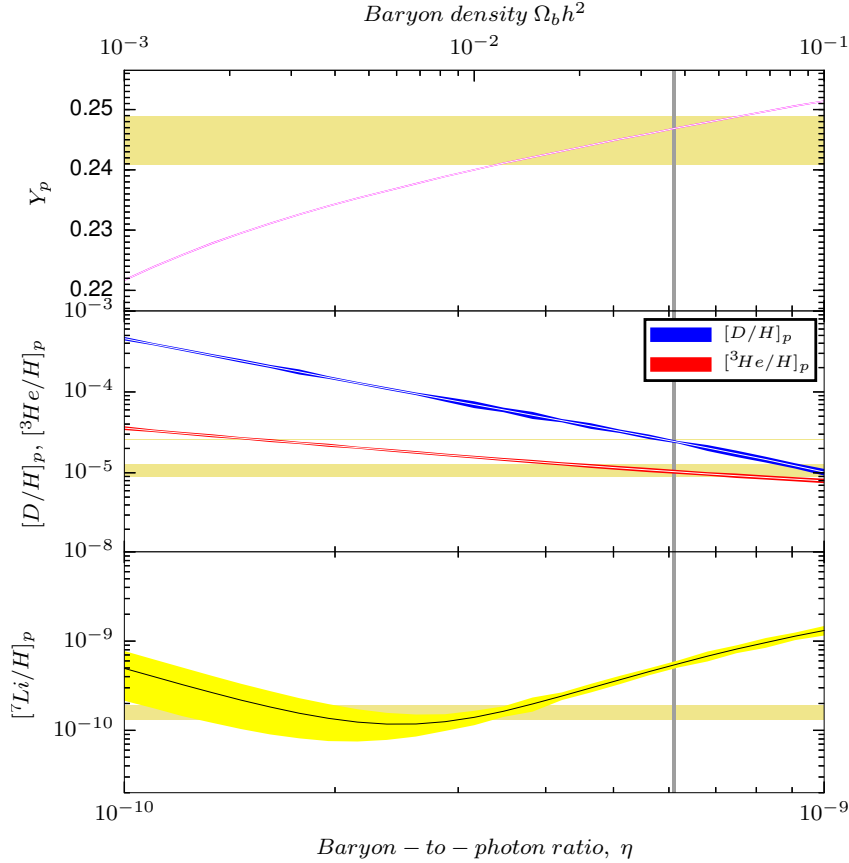
Figure 1.4: The figure shows the abundances of the most relevant light elements as a function of η. The plots are from a SBBN run with made AlterBBN, with η and τ_n as given in table 1.1 and $N_{eff} = 3.046$. The vertical band is the 1σ CMB measured value, while the horizontal bands are the observational constraints on the element abundances (see section 1.2). For the middle plot, the top/bottom band corresponds to the observed deuterium/helium-3 abundance. Uncertainties in the nuclear rates (high/low rates) are shown as colored bands around the central values. Note the generally good agreement between the observed and predicted abundances, except from the discrepancy of a factor ~3 in the ^7Li yield.

1.2 Observed Abundances

After the conditions were no longer right for sustaining further nuclear reactions, the abundances of D and ^4He remained constant until the onset of galaxy formation. As mentioned earlier, the abundances of ^3He and ^7Li would increase due to the decay of ^3H and ^7Be. Knowing the light element content in the first galaxies will therefore serve as a window on the relic abundances from the primordial nucleosynthesis. Any of the elements could in principle be used to constrain the cosmological parameters. However, they have differing dependences on η and most important, their abundances have undergone very different cosmological evolutions since the end of BBN. All the observed abundances are subject to uncontrolled systematic uncertainties, but since they are observed in completely different astronomical objects by different observational techniques, the errors are not correlated. Ideally we should therefore seek out to predict all abundances and compare with the observed ones, but as we will soon discuss, good estimates of ^3He and ^7Li are very hard to obtain. In the following we will go through all these elements and see why deuterium stands out as the most ideal "baryometer" of the four.

1.2.1 Deuterium

The low binding energy of 2.23 MeV of deuterium means that it is easily destroyed in astrophysical processes. During the collapse of pre-stellar nebulae it is completely burned into ^3He. Once the star has ignited, deuterium will be produced by nuclear fusion. However, all of this is burned to ^3He and beyond, so during the whole lifetime of a star, the net result is that the deuterium that went into the pre-stellar nebula is destroyed [8]. To our knowledge, there are no astrophysical sources of significant deuterium production. This leads to a simple and monotonic post-BBN evolution of the element, where all the deuterium we observe is of primordial origin [31]. Moreover, in regions of very low metallicity, the observed abundance is expected to approach its primordial value since matter have been less cycled through stars [8] [21].

The deuterium abundance is measured in absorption clouds along the line of sight to distant quasars
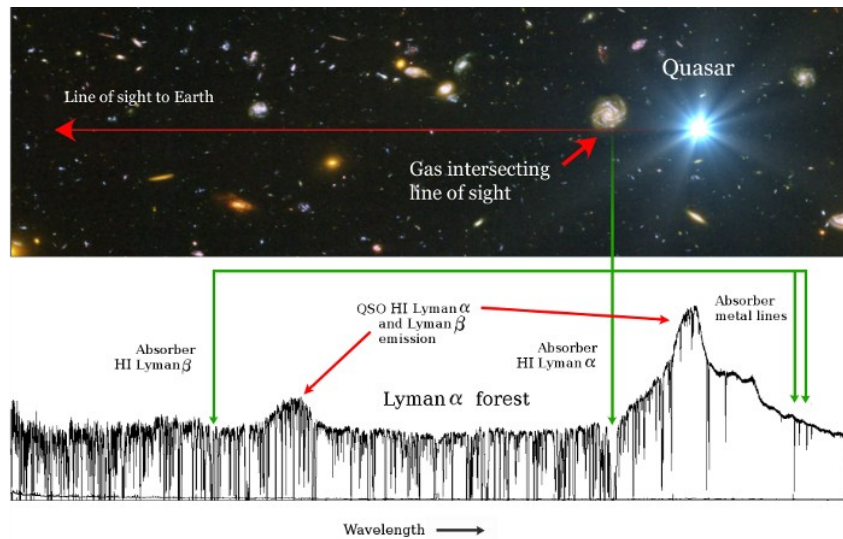

Figure 1.5: An illustration of the method of measuring the deuterium abundance in gas clouds in the intergalactic medium. The absorption of light emitted from a quasar will make its imprint on the Lyman α forest. Source: `http://nhmc.github.io/research.html`

(see figure 1.5). Light from the quasars are absorbed in intervening clouds, leading to a unique fingerprint from hydrogen, deuterium and other "metals" such as carbon, oxygen, silicon, iron etc. What we measure is the absorption of deuterium relative to hydrogen, that is, the D/H abundance. These two elements have a similar absorption signature, but is offset by $\sim 81\ km/s$. Practically, there are two factors that complicate the process. First, the small offset of the absorption features can make them difficult to separate, since they tend to blend into each other. Therefore, damped Lyman α absorbers (DLAs) are preferred in the analysis, as the absorption in such clouds is high enough to be detected, but still low enough to prevent a lot of blending ($N(H) > 2 \cdot 10^{20}$, but not a lot higher). Secondly, several clouds along the line of sight might absorb and their absorption lines blend together, making the process of identifying all the sources and separating them from one another a potentially challenging task.

Systems with a particularly simple kinematic structure are desired in analysis to avoid uncertainties with complex, only partially resolved components. The Particle Data Group's 2014 release of *Review of Particle Physics* [12] gives the value

$$[D/H]_p = (2.53 \pm 0.04) \cdot 10^{-5} \ ,$$

based on an analysis of a recently measured DLA showing 13 resolved D absorption lines, together with 4 older measurements. A more recent re-measurement [32] of an earlier analyzed DLA, now with significantly higher signal-to-noise reveals a value of

$$[D/H]_p = (2.55 \pm 0.03) \cdot 10^{-5} \ .$$

Since deuterium is destroyed with time, one would naturally seek to observe the element at the highest possible redshifts, in the limit where the metallicity approaches zero. However, the farther we observe the less photons we receive, imposing higher uncertainties on the data. This complicates the picture, but with accurate observations over a range of redshifts we may be able to get good estimates by extrapolating back to zero metallicity. In a recently published paper [33], *Dvorkin et al.* predicts a tight correlation between the the deuterium and metal abundances in any observed region. This finding suggest that even DLA's that are poor in deuterium might be studied at high sensitivity for Population III signatures and used together with samples from different environments in an extrapolation to zero metallicity, and that this might actually yield better estimates than targeting only metal-poor environments.

In chapter 4 we discuss the process of analyzing absorption clouds in the line of sight to distant quasars in the search for the primordial deuterium abundance. There I present the status of an analysis of the absorption system at $z = 2.407$ towards the quasar $Q1009 + 2956$, conducted parallel with the work on *AlterBBN*. I have yet to arrive at a new precise estimate of the deuterium abundance, but hope that this will be completed in the near future.

1.2.2 Helium-4

The ^4He abundance is measured in extragalactic HII (ionized hydrogen) regions, by observing ^4He and H emission lines. In stars ^4He is created from hydrogen through nuclear fusion, and subsequently used to create heavier elements such as carbon, nitrogen and oxygen. On average, the rate of ^4He production exceeds the rate of destruction of the element, meaning that the ^4He abundance increases with time. By tracking the stellar-produced ^4He as a function of metallicity, one can extrapolate back to zero metallicity and get good estimates. There is now a large body of data on ^4He and CNO from extragalactic HII systems, meaning that the statistical uncertainty on the primordial estimate is very low. However, these systems are very complex, and several physical parameters enter the $^4He/H$ determination. This induces quite large systematic errors, affecting the correlation between the helium and metal (e.g. oxygen) abundance, making the extrapolations to zero metallicity largely model dependent. For this reason, many differing estimates of the primordial abundance of ^4He have been proposed, not all being consistent with each other. Here I will use the estimate given by *Aver et al. 2015* [34], who reports a reduction of over 50% in the uncertainty compared to previous estimates. Their estimate is

$$Y_p = 0.2449 \pm 0.004 \ .$$

Note that the helium abundance is popularly given as a fraction of the total baryon content, while the other element abundances are given as the fraction of the element abundance by number to the hydrogen abundance by number.

Although the ^4He abundance is of great importance in the quest for new physics influencing the conditions in the early universe (sensitive to practically everything that might affect the n/p ratio), its logarithmic dependence on the baryon density makes it a rather poor baryometer. Consequently, since the ^4He abundance is very sensitive to the n/p ratio and possible new physics, while the deuterium abundance is very sensitive to the baryon density, combining the predictions of the two provides us with essentially all the desired information. The predictions of the other light elements therefore serves as a mere consistency check.

1.2.3 Helium-3

As mentioned, ^3He is produced in pre-stellar nebulae, by the burning of the more loosely bound deuterium. This new ^3He could either become part of the outer layers of the star, or be a part of the fusion

engine in the core. Inside stars, ^3He is both produced and destroyed, but unlike for the case with ^4He, the net result may be that ^3He is destroyed. ^3He is observed via its hyperfine emission line in HII regions in our own galaxy, but only a handful of observations have been made [35], and all the regions are quite metal-rich. Even if the observed gas clouds are quite old, one might suspect that its abundance has evolved a lot since the BBN. The inferred ^3He abundances show no correlation with metallicity or location in our galaxy, making the extrapolation to zero metallicity far too model dependent and uncertain. Also, since the abundance of the element is less sensitive to the baryon density than the deuterium abundance is, it is a poor baryometer compared to deuterium. Due to these facts it is not appropriate to use ^3He as a cosmological probe. Instead, one might hope to turn the problem around and constrain stellar astrophysics using the predicted primordial ^3He abundance [36]. As for consistency check purposes we will adopt the value

$$[^3He/H]_P = 1.1 \pm 0.2 ,$$

taken from *Bania et al.* [35], as an estimate for the primordial ^3He abundance.

1.2.4 Lithium-7

Lithium has a rather complex post-BBN evolution. As discussed, and similar to the case of ^3He, all the BBN-produced ^7Be decays into ^7Li well before stars and galaxies are created, thus the observed ^7Li abundance is actually the sum of the abundances of both mass-7 isotopes. Most of the ^7Li in the interior of stars will be burned away, but observations suggest that some of the element created in the hotter interiors may be transported to the cooler exteriors before being destroyed [8]. In the outer layers of the coolest, lowest-mass stars most of the element survives, and in stars undergoing the late, asymptotic giant branch phase of evolution, ^3He burning may lead to high surface ^7Li abundances. This may, or may not (depending on the stellar parameters like temperature and mass) lead to surviving ^7Li being ejected into the Interstellar Medium (ISM) as the star dies, resulting in a net increase in the lithium abundance over the lifetime of the star. Moreover, ^7Li is synthesized in non-stellar processes involving collisions of cosmic ray nuclei (protons, α-particles and CNO nuclei) with their counterparts in the ISM. Even though the relatively low binding energy of ^7Li (11.21 MeV) means that it is easily destroyed in the hot interior of stars, theoretical expectations, backed by observational data suggest that the overall trend is an increase of the galactic abundance with time [8].

^7Li is the most problematic of the observable BBN elements, and this may be due to its complex post-BBN evolution. Its primordial value is deduced by observations of metal-poor galactic globular cluster (GGC) stars and of very old, metal-poor Population II dwarf stars in the halo of our galaxy where the lithium abundance is almost independent of metallicity, displaying the so-called "Spite plateau" [37]. Most of the halo star observations measure only elemental lithium because thermal broadening in the stellar atmospheres exceeds the isotope separation between ^7Li and ^6Li. The latter is not synthesized in stars, only in cosmic ray interactions [38], and is a factor of $\sim 10^3$ less abundant than ^7Li.

The constant lithium abundance evident as the Spite Plateau is interpreted as corresponding to the BBN ^7Li yield, provided that the host stars in the observations have not destroyed any of their lithium. This is, of course, a questionable assumption, and some recent work by *Cyburt et al.* [21] seems to demand that at least some halo stars have destroyed their lithium. The authors uses new observations of small and thus highly convective stars, which leads to large uncertainties when extrapolating to zero metallicity. Disregarding these observations, and only including the ones consistent with the Spite Plateau, the *Review of Particle Physics 2014* [12] gives the value

$$[^7Li/H]_P = (1.6 \pm 0.3) \cdot 10^{-10} .$$

While the primordial abundances adopted from SBBN are in very good agreement with the observed values for D, ^4He and ^3He, the SBBN-predicted abundance of ^7Li is a factor ≈ 3 higher than its observed value. This is known as the "lithium problem", and a variety of suggestions have been proposed to

remedy this discrepancy between the predicted and the observed value. The most popular explanations are [39]:

- **Inaccurate stellar modeling** - As explained, the evolution of ^7Li in the outer layers of stars are quite complicated, and this is the areas from which it is observed. Complex stellar models are required to account for all the processes involved, and there is a possibility that those are simply not accurate enough. Stellar depletion of ^7Li in the outer layers due to mixing with the inner layers (due to convection, rotational mixing or diffusion) remains a possible solution, especially regarding the fact that the observations are made of the oldest stars that have had the longest time to deplete lithium in the outer layers. Additionally, there are uncertainties in the stellar parameters (e.g. the determined abundance of ^7Li is very sensitive to the assumed surface temperature of the star) that go into the calculations. However, the lack of dispersion in the observed data and the apparent presence of the Spite Plateau make it unlikely that this alone can explain the discrepancy.

- **The nuclear rates** - The uncertainties in BBN calculations are dominated by uncertainties in the nuclear rates. Overlooked reactions or inaccurate determinations of their uncertainties may lead to wrong BBN predictions of the abundance. Even though the abundances of D and ^4He are well determined by a mere 12 reactions, BBN codes usually include a lot more reactions (*AlterBBN* includes 100), all the way up to CNO (some codes even further). The main reason for doing so is to exclude a "nuclear solution" to the lithium problem. For example, the reaction $^7Be + {}^4He \rightarrow {}^{11}C$ is insignificant for the relic ^4He abundance since other reactions involving ^4He dominates its production/destruction, but since the ^7Li abundance is a factor $\sim 10^9$ lower than the ^4He abundance and since post-BBN decay of ^7Be is important for the late-time ^7Li abundance, it may have a huge indirect impact on the lithium we observe. However, re-examinations of the most important $^7Li + {}^7Be$ producing/destructing reactions, including $^7Be(d,p)2\alpha$, $^3He(\alpha,\gamma)^7Be$ and $^7Be(p,\gamma)^8Be$, have more or less ruled out a nuclear fix to the problem (e.g. [39] [40]). Although improved nuclear reaction rates and uncertainties may shorten the gap between the predicted and observed value, it seems that it is unable to close it.

- **New physics** - It may well be the case that the discrepancy between the predicted and observed abundance of ^7Li is indeed real, and that the SBBN scenario is insufficient in the prediction of the element abundances. Since we already have a very good agreement for D, ^4He and ^3He (bearing in mind that the ^3He abundance is inferred only from high-metallicity regions in our galaxy, and is therefore very uncertain), including any new physics is constrained to have a larger affect on the ^7Li abundance than for the other elements. There are several examples of new physics that have the potential of influencing BBN. Later, in chapter 3, we will look into the possibility that dark matter annihilation in the early universe may change the relic abundances of the lightest elements. Supersymmetry provides well-motivated candidates for decaying dark matter, and although most candidates emerging from this theory is non-relativistic and weakly interacting, one cannot exclude the existence of dark matter particles that are relativistic at the time of BBN, and thus having the potential of influencing BBN. Other suggestions range from changing cosmological constants to non-standard cosmologies, summarized in e.g. [41].

Chapter 2

AlterBBN

AlterBBN [42] was created by Alexandre Arbey in 2011, and is a public *C* program for evaluating the abundances of the elements generated during BBN. Several similar codes exists, and with the development of cosmology and nuclear physics comes the need for continuously updating the software. The first real attempt to deduct numerical experiments with the "early universe fusion reactor" came with the *Wagoner code* in 1969, based on a general numerical method published in 1968 by Robert V. Wagoner [43]. This code had a number of severe drawbacks, and was difficult to use, but it set the scene for a new era in BBN calculations. With the rapid increase in computer technology that followed, several improvements were made, and in 1988 Lawrence Kawano published the *Fortran-77* program *NUC123* [44], often referred to as the *Kawano code*. This code has later served as a reference for most of the preceding codes that have been published, and the underlying numerical methods are based on the ones laid out by Wagoner in 1968.

AlterBBN is structured very similar to that of *NUC123* and uses the same calculation techniques, driven by a *Runge Kutta* solver to compute the set of differential equations governing the BBN. It is also inspired by the *Fortran-77* program *PArthENoPE* [45] published in 2007, with a similar purpose as *AlterBBN*. *PArthENoPE* is a popular code for computing the BBN-created abundances, but uses a separate library (NAG) for the evaluation of some special functions and algebraic operations. This library is not included in the *PArthENoPE* package, and is quite expensive. The purpose of updating *AlterBBN* to the same standard as *PArthENoPE* is therefore to have a free, open source code that can do the same job. Moreover, some new reaction rates have been published since the release of *PArthENoPE*, which I have added to the updated *AlterBBN* code, and described later in this chapter. The source code for *PArthENoPE* can be obtained by request (but cannot be run without the NAG library), and I have used this as a reference for the implementation of the extended nuclear network.

The latest release of *AlterBBN* is *AlterBBN v1.4* of 28 June 2013 [1]. In the following I will refer to this as *the original code*. The program predicts the abundances of the light elements for various cosmological models, that can be compared to observations. It consists of five main programs which, except from the standard cosmological model program, requires that the different free parameters are given as input arguments. The five different programs are:

- **stand_cosmo.x**, which computes the abundances of the elements in the standard ΛCDM cosmological model, with a pre-defined default value of η;

- **alter_eta.x**, which computes the abundance of the elements in the standard cosmological model,

---

[1] May be downloaded from `http://superiso.in2p3.fr/relic/alterbbn`

with the required input argument
- η: baryon-to-photon ratio;

- **alter_neutrinos.x**, which computes the abundance of the elements in the standard cosmological model, with the required input argument
  - N_ν: the number of neutrino families,

  and the optional arguments
  - ξ_{ν_e}: the electron neutrino degeneracy parameter,
  - ξ_{ν_μ}: the muon neutrino degeneracy parameter,
  - ξ_{ν_τ}: the tau neutrino degeneracy parameter;

- **alter_standmod.x**, which computes the abundance of the elements in cosmological scenarios with modified expansion rates and entropy contents, with the required arguments
  - κ_ρ: the ratio of dark energy density over radiation energy density at BBN time,
  - n_ρ: the dark energy density decrease exponent,
  - κ_s: the ratio of dark entropy density over radiation entropy density at BBN time,
  - n_s: the dark entropy density decrease exponent,

  and the optional arguments
  - T_ρ: the temperature in GeV below which the dark energy density is set to 0,
  - T_s: the temperature in GeV below which the dark entropy density is set to 0;

- **alter_reheating.x**, which computes the abundance of the elements in cosmological scenarios with modified expansion rates and entropy contents, with the addition of entropy production. The required arguments are
  - κ_ρ: the ratio of dark energy density over radiation energy density at BBN time,
  - n_ρ: the dark energy density decrease exponent,
  - κ_Σ: the ratio of dark entropy production over radiation entropy production at BBN time,
  - n_Σ: the dark entropy production exponent,
  - T_r: the temperature in GeV below which the dark energy density and the entropy production are set to 0.

The different parameters concerning the non-standard cosmological scenarios above will be discussed in more detail in section 2.1.

Some changes to the original code, regarding its layout, were made prior to my work. I have built on this modified version and made some further changes to the layout, in addition to an update of the nuclear reactions and the inclusion of new physics.

2.1   Structure of the Original Code

A basic, general description of the BBN physics was given in section 1.1. We will now extend the discussion to include all the relevant equations needed to compute the light element abundances, and how they are implemented in *AlterBBN*. Modifications and extensions to the latest version of the program will be discussed in section 2.2. This review is a more detailed version of that found in the *AlterBBN* manual [42]. New physics that I have implemented in the program will be discussed in chapter 3. Notice that in general expressions or definitions I try to use the standard notation of the temperature, where T is in units of Kelvin, whereas in expressions specific for, or important for the code itself I use the dimensionless variable

$$T_9 = \frac{T}{10^9 \ K} \ .$$
(2.1)

2.1.1 Standard Big Bang Nucleosynthesis

Nuclear Reactions

In the original code, all the implemented nuclear reactions have evolution equations on the form

$$N_i \, ^{A_i}Z_i + N_j \, ^{A_j}Z_j \longleftrightarrow N_k \, ^{A_k}Z_k + N_l \, ^{A_l}Z_l, \tag{2.2}$$
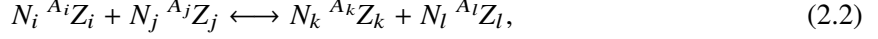
where $A_i \geq A_j$, $A_l \geq A_k$, and the exothermic direction is from left to right. The abundance change of a nuclide i is given by the sum over all forward and reverse reactions involving nuclide i, that is

$$\frac{dY_i}{dt} = \sum_{j,k,l} N_i \left(-\frac{Y_i^{N_i} Y_j^{N_j}}{N_i! N_j!} \Gamma_{ij \to kl} + \frac{Y_l^{N_l} Y_k^{N_k}}{N_l! N_k!} \Gamma_{kl \to ij} \right). \tag{2.3}$$

Here, the nuclide abundance is defined as $Y_i = X_i / A_i$, where $X_i = n_i / n_B$ is the mass fraction in nuclide i and A_i its atomic number. N_i is the number of nuclides i, $\Gamma_{ij \to kl}$ is the forward reaction rate and $\Gamma_{kl \to ij}$ is the reverse rate (see appendix A for a brief review of the theory regarding the reaction rates). The numerical implementation of this equation is thoroughly explained in both [43] and [46] and will not be further discussed here.

The program tracks the evolution of 26 nuclides from an initial temperature $T_{9,i}$ to a final temperature $T_{9,f}$. Following the numbering of *AlterBBN*, the nuclides that are a part of the code are

- 1: n
- 2: p
- 3: ^2H
- 4: ^3H
- 5: ^3He
- 6: ^4He
- 7: ^6Li
- 8: ^7Li
- 9: ^7Be
- 10: ^8Li
- 11: ^8B
- 12: ^9Be
- 13: ^{10}B
- 14: ^{11}B
- 15: ^{11}C
- 16: ^{12}B
- 17: ^{12}C
- 18: ^{12}N
- 19: ^{13}C
- 20: ^{13}N
- 21: ^{14}C
- 22: ^{14}N
- 23: ^{14}O
- 24: ^{15}N
- 25: ^{15}O
- 26: ^{16}O

Due to the mass-8 bottleneck explained in chapter 1, insignificant amounts of metals heavier than ^9Be were created in the Big Bang Nucleosynthesis. However, although the relic abundances of the heavier elements are negligible even compared to that of ^6Li ($^6Li/H \sim 10^{-14}$), some reactions involving carbon, nitrogen, oxygen etc. will break the bottleneck and influence BBN through sub-sequent reactions with the lighter elements. Including more reactions is important to rule out a nuclear fix to the lithium problem (see chapter 1.2.4) and provides an overall better accuracy of the code.

Iteration Variables

The program time-evolves the photon temperature T_9, the electron chemical potential μ_e parameterized through the degeneracy parameter $\phi_e \equiv \mu_e / k_B T$, and the quantity h_η [43][44][47]. The latter is a lowest order parametric representation of the baryon density (see equations 2.19 and 2.20 with discussion), used for convenience as it is proportional to η and remains fairly constant as the universe expands, under the assumption of adiabatic expansion. It is time-evolved from an initial value given by (initial value is here denoted by i and is not to be confused with the nuclide number i in equations 2.2 and 2.3)

$$h_{\eta,i} = M_u \frac{n_{b,i}}{T_{9,i}^3} = M_u \frac{n_{\gamma,i}}{T_{9,i}^3} \eta_i \approx 33685.519 \cdot \eta_0 \left(1 + \frac{s_{e^\pm}(T_i)}{s_\gamma(T_i)} \right) \tag{2.4}$$

where M_u is the atomic mass unit and η_0 the late-time (CMB measured) value of the baryon-to-photon ratio. The relation between the initial and late-time value of η is found from equation 1.36 through entropy conservation. In the original code the initial ratio between the entropy of the electrons/positrons and the photons is approximated to 7/4, assuming $m_e \to 0$. Since the $e^\pm$-pairs are not fully relativistic this imposes a small error in $h_{\eta,i}$. At $T = 2$ MeV Nollett & Steigman [48] estimate that an accurate treatment of the $e^\pm$ entropy gives $s_{e^\pm}$ a value about 2% below its relativistic approximation. In the updated *AlterBBN* the assumption of $m_e \to 0$ is relaxed, leading to a more accurate initial estimate of

h_η. This modification of the original code is further discussed in section 2.2.5. In the last equality in equation 2.4 I have inserted the physical constants to reveal the *AlterBBN*-implemented expression, which is in units of $g\ cm^{-3}\ K^{-3}$. I will also do so in some other cases later, and this is done to clarify the origin of some of the numerical factors that the reader may encounter if consulting the program code.

T_9, ϕ_e and h_η are used to find the density and pressure of the relevant particles, described in the following. First, the equation of energy conservation may be written as

$$\frac{d}{dt}(\rho_{\text{tot}}a^3) + P_{\text{tot}}\frac{d}{dt}(a^3) - a^3\frac{d\rho_{\text{tot}}}{dt}\bigg|_{T=const} = 0\,, \tag{2.5}$$

from which we may obtain [44]

$$\frac{dr}{dT_9} = -\frac{\frac{d\rho_{\text{tot}}}{dT_9}}{\rho_{\text{tot}} + \frac{P_{\text{tot}}}{c^2} + \left(\frac{1}{dr/dt}\right)\frac{d\rho_{\text{tot}}}{dt}\big|_{T_9}}\,, \tag{2.6}$$

where $r \equiv ln(a^3)$, which incorporates the thermodynamic effect of the universal expansion on the particle temperatures. If we assume that the neutrinos have already decoupled the total energy density and pressure is given by

$$\rho_{\text{tot}} = \rho_\gamma + \rho_b + (\rho_{e^-} + \rho_{e^+})\,, \tag{2.7}$$

and

$$P_{\text{tot}} = P_\gamma + P_b + (P_{e^-} + P_{e^+})\,. \tag{2.8}$$

This is needed to find the time-derivatives of the temperature:

$$\frac{dT_9}{dt} = \frac{dr/dt}{dr/dT_9}\,, \tag{2.9}$$

and the electron degeneracy parameter:

$$\frac{d\phi_e}{dt} = \frac{\partial\phi_e}{\partial T_9}\frac{dT_9}{dt} + \frac{\partial\phi_e}{\partial r}\frac{dr}{dt} + \frac{\partial\phi_e}{\partial S}\frac{dS}{dt}\,, \tag{2.10}$$

where $S = \sum_i Z_i Y_i$, Z_i being the charge number of nuclei i. The numerical implementation of this expression requires a detailed review of the different derivatives, which will not be given here. Instead, I refer to appendix D in *Kawano 1992* [44] where all relevant information can be found. The time derivative of h_η is found by the reasoning that $h_\eta \sim \rho_b/T^3 \sim 1/a^3/T^3$ (see equation 2.19 with discussion), that is

$$\frac{dh_\eta}{dt} = -3h_\eta\left(\frac{1}{a}\frac{da}{dt} + \frac{1}{T_9}\frac{dT_9}{dt}\right)\,. \tag{2.11}$$

The energy density of the photons is given by the bosonic part of equation 1.19, thus

$$\rho_\gamma = \frac{1}{c^2}\frac{g_\gamma\pi^2}{30}\frac{(k_BT)^4}{(\hbar c)^3} = 8.41828 \cdot T_9^4\,, \tag{2.12}$$

since $g_\gamma = 2$. The last equality is how it is implemented in *AlterBBN*, and is in units of $g\ cm^{-3}$. The pressure is related to the density by

$$\frac{P_\gamma}{c^2} = \frac{1}{3}\rho_\gamma. \tag{2.13}$$

In the case that the neutrino asymmetry is zero, the energy density of the neutrinos is given by the fermionic part of equation 1.19, yielding

$$\rho_\nu = \frac{1}{c^2}g_\nu N_{\text{eff}}\frac{7}{8}\frac{\pi^2}{30}\frac{(k_BT_\nu)^4}{(\hbar c)^3} = 12.79384\left[g_\nu N_{\text{eff}}\frac{\pi^2}{30}T_{9,\nu}^4\right]\,, \tag{2.14}$$

given in units of $g\ cm^{-3}$. For the SBBN scenario $g_\nu = 2$ and $N_{\text{eff}} = 3$ or, if relaxing the assumptions of instantaneous neutrino decoupling and extremely relativistic $e^\pm$ pairs, $N_{\text{eff}} = 3.046$, as explained in chapter 1.1. Any neutrino degeneracy will lead to a non-zero chemical potential and a bit more involved evaluation of the expression in the square brackets, which will be discussed in section 2.1.2. The neutrino temperature is found by the assumption that the baryon number is conserved, such that $n_b a^3 = constant$, combined with the requirement that the neutrinos simply redshift with the expansion of the universe, leading to

$$T_{\nu 9} = T_{9,i} \left(\frac{h_\eta T_9^3}{\rho_{b,0}} \right)^{1/3} . \tag{2.15}$$

Note that the assumption that $T_\nu \propto a^{-1}$ is true only in the standard scenario. In the presence of e.g. a neutrino coupled WIMP the neutrinos will be heated relative to the photons as the WIMP annihilates, and equation 2.15 is no longer valid. This will be further discussed in chapter 3.

Since the assumption of extremely relativistic electrons and positrons is not entirely accurate at the time of BBN, one cannot simplify the expressions 1.15, 1.16 and 1.17 the same way as was done to find the photon and neutrino densities. Inspired by the method described by Wagoner [43] and the Kawano code [44] the expressions are approximated by using the modified Bessel functions of second type through the definitions

$$L(z) = \frac{K_2(z)}{z}, \qquad M(z) = \frac{1}{z}\left[\frac{3}{4}K_3(z) + \frac{1}{4}K_1(z)\right], \qquad N(z) = \frac{1}{z}\left[\frac{1}{2}K_4(z) + \frac{1}{2}K_2(z)\right], \quad (2.16)$$

where $z = m_e c^2 / k_B T$ and K_α are the modified Bessel function of order α. Using these approximations the expressions for the sum of the electron/positron densities and pressures then reads (see appendix C for derivation)

$$\rho_{e^-} + \rho_{e^+} = \frac{1}{c^2} \frac{g_e}{\pi^2} \frac{(m_e c^2)^4}{(\hbar c)^3} \sum_{n=1}^{\infty} (-1)^{n+1} \cosh(n\phi_e) M(nz) \tag{2.17}$$

$$\frac{P_{e^-} + P_{e^+}}{c^2} = \frac{1}{c^2} \frac{g_e}{\pi^2} \frac{(m_e c^2)^4}{(\hbar c)^3} \sum_{n=1}^{\infty} \frac{(-1)^{n+1}}{nz} \cosh(n\phi_e) L(nz) \tag{2.18}$$

Using that $g_e = 2$ and that $m_e c^2 = 0.51100$ MeV $= 8.18700 \cdot 10^{-7}$ erg $= 8.18700 \cdot 10^{-7}\ g\ cm^2\ s^{-2}$ (electrons and positrons), the pre-factor is equal to $3205.724\ g\ cm^{-3}$. Note that the electron and positron chemical potentials have the opposite sign, thus $\phi_e = \phi_{e^-} = -\phi_{e^+}$. The expressions 2.16 are further used to approximate the derivatives of these quantities, among others, needed to compute equations 2.11, 2.9 and 2.10.

Baryon Density Derivative
The baryon density is given by the first order approximation (from equation 2.4)

$$\rho_b \approx h T_9^3. \tag{2.19}$$

This approximation is, however, not accurate enough when calculating the derivative of the baryon density, which would drop out of equation 2.6. Including higher order terms, Wagoner [43] describes a more complete expression for the baryon density, given by

$$\begin{aligned} \rho_b &= n_b \left[M_u + \sum_i \left(\Delta M_i + \frac{3k_b T}{2c^2} \right) Y_i \right] \\ &= h_\eta T_9^3 \left[1 + \sum_i \left(\frac{\Delta M_i}{M_u} + \zeta T_9 \right) Y_i \right], \end{aligned} \tag{2.20}$$

where ΔM_i is the mass excess [2] of nuclide i and $\zeta = 1.388 \cdot 10^{-4}$. The non-zero part of the temperature-derivative of the baryon energy density is then

$$\frac{d\rho_b}{dT_9} = h_\eta T_9^3 \zeta \sum_i Y_i \,, \tag{2.21}$$

while the baryon pressure is given by [44]

$$P_b = h_\eta T_9^3 \left(\frac{2}{3} \zeta T_9 \sum_i Y_i \right) . \tag{2.22}$$

Charged Lepton Degeneracy

The charged lepton ($e^\pm$) degeneracy will depend on the electron chemical potential, which is parameterized through ϕ_e. Like in the case with the electron and positron density and pressure, their number densities are approximated through the modified Bessel functions (from equation 1.15), and the expression for their difference reads

$$n_{e^-} - n_{e^+} = \frac{g_e}{\pi^2} \left[\frac{m_e c^2}{\hbar c} \right]^3 \sum_{n=1}^\infty (-1)^{n+1} \sinh(n\phi_e) L(nz) \,. \tag{2.23}$$

This can also be found by charge conservation, which gives

$$n_{e^-} - n_{e^+} = \mathcal{N}_A h_\eta T_9^3 S, \tag{2.24}$$

where $\mathcal{N}_A$ is the Avogadro number, which by definition is $\mathcal{N}_A = 1/M_u$. Charge conservation limits the charged lepton asymmetry to be of the same order as the baryon asymmetry, meaning that $\mu_e/k_B T \sim 10^{-9}$ prior to $e^\pm$ annihilation, which is illustrated in figure 2.1. By equating the two expressions for the difference between the number densities of electrons and positrons, using that $\sinh(x) \approx x$ for $x \ll 1$ and inserting the dimensionless variable $z = m_e c^2/k_B T$, we find for the initial value of ϕ_e:

$$\begin{aligned} \phi_e(T_{9,i}) &\approx \frac{\pi^2}{2} \frac{(k_B \hbar c)^3}{M_u} \frac{h_\eta(T_{9,i}) Y_{p,i}}{(10^9 z_i)^3} \frac{1}{\sum_{n=1}^\infty (-1)^{n+1} n L(nz_i)} \\ &\approx 3.568 \cdot 10^{-5} \cdot \frac{h_\eta(T_{9,i}) Y_{p,i}}{z_i^3 \sum_{n=1}^\infty (-1)^{n+1} n L(nz_i)} \,, \end{aligned} \tag{2.25}$$

where the subscript i means initial value, and we have used that prior to BBN the baryon budget consisted of only protons and neutrons, thus

$$\sum_i Z_i Y_i = Z_n Y_n + Z_p Y_p = 0 \cdot Y_n + 1 \cdot Y_p = Y_p. \tag{2.26}$$

Initial Abundances

The initial abundances of protons and neutrons are described by the distribution functions

$$Y_p(T_i) = \frac{1}{1 + e^{-Q/T_i}} \,, \qquad Y_n(T_i) = \frac{1}{1 + e^{Q/T_i}} \,, \tag{2.27}$$

where Q is the difference between the neutron and proton masses, which was encountered in equation 1.38. These values are thus naturally dependent on the neutron-to-proton ratio at temperature T_i. The initial time is found by (approximation for $T \to \infty$ and $t \to 0$ [47])

$$t_i = (12\pi G \sigma c^{-2})^{1/2} T_{9,i}^{-2} \approx (0.09615 \cdot T_{9,i})^{-2} \,, \tag{2.28}$$

where σ is Stefan-Boltzmann's constant and G is Newton's gravitational constant.

---

[2] The difference between the actual mass of the nuclide and its mass number in atomic mass units.

2.1.2 Modified Cosmological Scenarios

Several unknown physical processes may influence the evolution of the early universe. *AlterBBN* has the options of modifying the number of neutrino families and impose a neutrino degeneracy among the standard model neutrinos, in addition to modifying the expansion rate and entropy content directly. Moreover, it can apply reheating models with a resulting entropy production. These modified cosmological scenarios influence the properties of the early universe in different ways, and in the following we will explain the physics and how they are implemented in the program. In this discussion I will set $k_B = \hbar = c = 1$.

Adding equivalent neutrinos and a Non-Zero Neutrino Degeneracy

Adding equivalent neutrinos alone has the effect of speeding up the expansion of the universe through an increased energy density. The extra radiation is absorbed into the neutrino energy density, given by equation 2.14, through the definition of N_{eff} (see chapter 1.1.6). Using a non-zero neutrino degeneracy, on the other hand, will lead to a more involved calculation of the neutrino energy density. In chapter 1.1 we gave a detailed description of the neutrino degeneracy parameter ξ and explained that due to mixing of the standard model neutrinos, one usually assumes that the chemical potential of the three species are equal, thus writing $\xi = \xi_e = \xi_\mu = \xi_\tau$. However, *AlterBBN* gives the user the option to provide differing values of ξ_e, ξ_μ and ξ_τ. We also mentioned that any contribution to the expansion rate ($S \neq 0$) emerging from a non-zero neutrino degeneracy is very small, and is likely to yield differences in the relic abundances smaller than the observationally imposed uncertainties. Although this may be true we still need to keep track of it, since the combined effect of multiple small modifications to the standard cosmology scenario may lead to significant changes in the abundances. In *AlterBBN* this effect is implemented by modifying the neutrino density to [44]

$$\rho_{\nu_\alpha, \bar{\nu}_\alpha} = \frac{1}{2\pi^2} T_\nu^4 \int_0^\infty dx \frac{x^3}{1 + \exp(x \mp \xi_{\nu_\alpha})} \,, \tag{2.29}$$

where it is assumed that the three species share the same temperature, and the total neutrino density is found by summing over the three neutrino species ν_α, $\alpha = e, \mu, \tau$. The minus sign in the exponential is for the neutrinos and the plus sign is for the anti-neutrinos. Integrating this expression is quite time consuming, so that in the case of a very small neutrino degeneracy ($\xi \leq 0.03$) the approximation [44]

$$\rho_{\nu_\alpha} + \rho_{\bar{\nu}_\alpha} = \frac{\pi^2}{15} T_\nu^4 \left(\frac{7}{8} + \frac{15}{4\pi^2} \xi_{\nu_\alpha}^2 + \frac{15}{8\pi^4} \xi_{\nu_\alpha}^4 \right) \tag{2.30}$$

is used, while the approximation [44]

$$\rho_{\nu_\alpha} + \rho_{\bar{\nu}_\alpha} = \frac{1}{8\pi^2} (T_\nu \xi_\nu)^4 \left[1 + \left(\frac{2\pi^2}{\xi_\nu^2} \right) \right] \tag{2.31}$$

is used for very large values ($\xi \geq 30$). For $0.03 < \xi < 30$ equation 2.29 must be integrated numerically.

The most important effect of a non-zero neutrino degeneracy is the altered neutron-to-proton ratio through charged current weak interactions involving the electron neutrinos and anti-neutrinos. This leads to a modification of the weak rates controlling the $p \leftrightarrow n$ reaction, and the initial abundances of protons and neutrons are changed from the ones given in 2.27 to

$$Y_p(T_i) = \frac{1}{1 + e^{-Q/T_i - \xi_{\nu e}}} \,, \qquad Y_n(T_i) = \frac{1}{1 + e^{Q/T_i + \xi_{\nu e}}} \,. \tag{2.32}$$

Modified Expansion Rate

Contributions to the total relativistic energy at the time of BBN will change the expansion rate of the universe and consequently the primordial abundances. In *AlterBBN* one can parameterize any such

phenomena by adding an effective dark energy density ρ_D to the first Friedmann equation, which is then modified from equation 1.6 ($k = 0$) to

$$H^2 = \frac{8\pi G}{3}(\rho_{\text{tot}} + \rho_D) \,.$$ (2.33)

As a parameterization for ρ_D the code adopts, as described in [49] [50],

$$\rho_D = \kappa_\rho \rho_{\text{tot}}(T_0) \left(\frac{T}{T_0}\right)^{n_\rho} \,,$$ (2.34)

where $k_B T_0 = 1$ MeV. κ_ρ is then the ratio of effective dark density over the total energy density, and $n_\rho = 3(1 + w)$ is a constant parameterizing the density behavior, depending on whether it behaves like radiation ($n_\rho = 4$), matter ($n_\rho = 3$), vacuum energy ($n_\rho = 6$) etc. (see chapter 1.1.2 for the definition of w, and [49] for more information about n_ρ).

Modified Entropy Content

The entropy content can also receive various contributions from unknown sources, e.g. from exotic particles that annihilate during BBN and heats the photons relative to the neutrinos or vice versa. In the original code any such contribution is parameterized in a generic way by considering an effective dark entropy density s_D, so that the energy conservation is modified from equation 2.5 to

$$\frac{d}{dt}(\rho_{\text{tot}}a^3) + P_{\text{tot}}\frac{d}{dt}(a^3) - a^3 \left.\frac{d\rho_{\text{tot}}}{dt}\right|_{T=const} - T\frac{d}{dt}(s_D a^3) = 0 \,.$$ (2.35)

In the case of no reheating, the parameterization (described in [50])

$$s_D = \kappa_s s_{\text{rad}}(T_0) \left(\frac{T}{T_0}\right)^{n_s}$$ (2.36)

is used, where $k_B T_0 = 1$ MeV, and

$$s_{\text{rad}}(T) = h_{\text{eff}}(T)\frac{2\pi^2}{45}T^3 \,,$$ (2.37)

h_{eff} being the effective number of entropic degrees of freedom of radiation, κ_s the ratio of effective dark entropy density over radiation entropy density, and n_s a constant parameterizing the entropy behavior, depending on whether it is radiation-like, matter-like etc. (see [50] for specific values of this). In the case that a particle annihilates and reheats the plasma, however, there will be additional entropy production. Arbey et al. [51] describes an evolution of the entropy production Σ_D according to

$$\Sigma_D(T) = \kappa_\Sigma \Sigma_{\text{rad}}(T_0) \left(\frac{T}{T_0}\right)^{n_\Sigma} \,,$$ (2.38)

where again $k_B T_0 = 1$ MeV. κ_Σ is the ratio of effective dark entropy production over radiation entropy production while n_Σ describes the behavior of the entropy production, which in most reheating scenarios will be $n_\Sigma \sim -1$ (see [51]). The radiation entropy production reads:

$$\Sigma_{\text{rad}}(T_0) = \left(\frac{4\pi^3 G}{5}g_{\text{eff}}(T_0)\right)^{1/2} T_0^2 s_{\text{rad}}(T_0) \,,$$ (2.39)

g_{eff} being the effective number of degrees of freedom of radiation. The dark entropy density is then found by integrating over the entropy production, as

$$s_D(T) = 3\sqrt{\frac{5}{4\pi^3 G}}h_{\text{eff}}T^3 \int_0^T dT' \frac{g_*^{1/2}\Sigma_D(T')}{\sqrt{1 + \frac{\rho_D}{\rho_{\text{rad}}}h_{\text{eff}}^2(T')T'^6}} \,,$$ (2.40)

where

$$g_*^{1/2} = \frac{h_{\text{eff}}}{\sqrt{g_{\text{eff}}}}\left(1 + \frac{T}{3h_{\text{eff}}}\frac{dh_{\text{eff}}}{dT}\right) \,.$$ (2.41)

2.2 Changes to The Original Code

The main tasks of this project were to get the nuclear network of *AlterBBN* up to date and to add new physics to the code. However, working with the original code I soon realized that I had to make some changes to the interface and layout, to facilitate the desired runs and extraction of data. Prior to my work, some changes were made in this regard, and I have built on these modifications plus added some more. In this section I will go through all the changes, up until the inclusion of new physics, which will be discussed in chapter 3. The changes discussed here are

- **New layout/interface**, related to how the program is run. Instead of five main programs for different cosmological scenarios, all the physics is collected into one program, with parameter inputs given in a *.ini*-file. An external *PYTHON* program was made to execute *AlterBBN*. This is very convenient in the case that we want to do multiple runs with *AlterBBN*, varying parameters like the baryon-to-photon ratio, WIMP mass etc.

- **Correction of the initial time** when including extra relativistic degrees of freedom.

- **Extension of the nuclear network**, with the addition of 12 new reactions to the original 88. The new reactions are implemented as in *PArthENoPE* [45].

- **Updated reaction rates** for six important reactions: $H(n,\gamma)^2H$ [52], $^7Be(n,\alpha)^4He$ [53], $^3He(\alpha,\gamma)^7Be$ [54], $^2H(p,\gamma)^3He$ [55], $^2H(d,n)^3He$ [55] and $^2H(d,p)^3H$ [55].

- **The initial value of the electron-positron entropy density**, needed to estimate the initial value of h_η, have been corrected to account for the partial non-relativistic nature of the $e^\pm$-pairs around the time of neutrino decoupling.

In addition to these updates, a few bugs were discovered in the original version. The first one involves the array *double reacparam* in the function *nucl* (and *nucl_failsafe*), where the reactions $^{12}N(\alpha,p)^{15}O$ and $^{13}N(\alpha,p)^{16}O$ (reactions number 92 and 93 in the updated version) were of the wrong reaction type. Those have been changed from type 3 to type 2 (see section 2.2.3) in the updated version. A second error was found in the reaction rate of the reaction $^3H(D,n)^4He$ (number 30), which originally contained a factor $1.8764462 \cdot 10^9 T_9^2$. According to *Serpico et al.* [56] this should be $1.8764462 \cdot 10^9 T_9^3$, and has been changed accordingly in the updated version. Finally, the contribution from thermally excited levels to the reaction $^{13}C(p,\gamma)^{14}N$, which is reaction number 73 in the updated version, was wrongly added to reaction number 72 instead. This has now been corrected.

2.2.1 New Layout/Interface

As discussed in the introduction to this chapter, the original code consists of five main programs concerning different cosmological scenarios. Except from the program computing the parameter-free standard cosmological model, using the CMB-measured value of η, they all require a various number of input arguments. For the two programs involving dark energy/dark entropy density and entropy production, the number of input arguments is quite large (4-6), and having to enter all those arguments for every run can be a source of frustration. As mentioned, a modification to this layout was made prior to my work, by Digvijay Wadekar at the University of Oslo [57]. The five main programs were compressed into two; the first one covering *stand_cosmo*, *alter_eta* and *alter_neutrinos*, requiring the parameters to be given in a separate *.ini*-file (named *input.ini*); the second one covering *alter_standmod* and *alter_reheating*, requiring the parameters to be given in the code itself. I find it convenient to collect all parameters that can be changed by the user in one single file, even though some of them may not be used as much as

others. I also combined the two programs into one, making it more practical both to work with and to use, even though the *main*-part of the code got a bit more involved. The addition of WIMPs (see chapter 3) was also implemented into this new, combined program. The new layout thus consists of only one main code, *primary.c*, using the input file *input.ini* to extract parameter values given by the user.

To differ between the various cosmological models, the executable *primary.x* now takes one input argument. If this argument is **standard** the program will collect the parameters η, τ, N_ν, ΔN_ν, ξ_{ν_e}, ξ_{ν_μ} and ξ_{ν_τ} from the input file, and use those in the computation. Although not a part of *standard* cosmology, I decided to include the neutrino degeneracy parameters in this option to minimize the number of input argument options. If the user do not want to include any neutrino degeneracy, these parameters must therefore be set to zero. Using the argument **darkdens** together with the executable will modify the expansion rate and entropy content, and concerns the parameters κ_ρ, n_ρ, κ_s, n_s, T_ρ and T_s, while the argument **reheating** will modify the expansion rate and add entropy production, thus concerning the parameters κ_ρ, n_ρ, κ_Σ, n_Σ and T_r. By default, the different cut-off temperatures are set to 0, which means that the program will take equations 2.34, 2.36 and 2.40 into consideration throughout the whole run, but the user is free to change these parameters through the input file. To invoke simulations including WIMPs the user may give the argument **wimp**. The parameters that need to be set through the input file in this setting is the WIMP mass, the type of WIMP, its coupling to the standard model particles, and its chemical potential. Further details of these parameters will be given in chapter 3. Finally, the user may run the executable without giving any arguments. The program will then run the parameter-free standard cosmology scenario with $\eta_{10} = 6.10$, $\tau = 880.3$ and $N_{eff} = N_\nu = 3.046$. Note that for the options **darkdens** and **reheating** the parameters η, τ, N_ν, ΔN_ν, ξ_{ν_e}, ξ_{ν_μ} and ξ_{ν_τ} are also set through the *.ini*-file. A combination of the options **darkdens**, **reheating** and **wimp** is possible, since there might exist interesting cases where e.g. a light WIMP with specified properties is combined with extra radiation/entropy of an unspecified nature. Beware that with this combination implemented, it is essential that all parameters controlling the **darkdens** and **reheating** options are set to zero when a "combination-less" WIMP run is made. For all individual options (**standard**, **darkdens** and **reheating**), on the other hand, none of the parameters that are not part of the option are included in the calculation.

AlterBBN does not come with the functionality of internally varying any of the parameters that go into the computation. Such an option is necessary if we want to study the change in the resulting abundances by varying e.g. the baryon-to-photon ratio. Instead of modifying the program itself to do this, I wrote an external *PYTHON* program for compiling and executing *AlterBBN*, which I have called *ARES*. This interacts with the input file, and enables the user to run *AlterBBN* for as many times as desired while varying a parameter of choice. The parameters that are allowed to vary is the baryon-to-photon ratio (η), both the equivalent number of neutrinos (ΔN_ν) and the effective number of neutrinos (N_{eff}) as well as all the neutrino degeneracy parameters (ξ_e, ξ_μ and ξ_τ), the neutron lifetime (τ_n), the WIMP mass (m_χ) and the WIMP electron chemical potential parameterized as a degeneracy parameter (ϕ_χ). A switch may be used to show a plot of the light element abundances of D, ^4He, ^3He and ^7Li as a function of η if this is chosen as the free parameter (see figure 1.4). The results from all the runs are written to the file *alterdata.txt*, which may then be used to make plots etc.

The program may also be used in the case that all parameters are fixed (single *AlterBBN* run). This way the user do not have to compile *AlterBBN* before running, rather just execute *ARES*. Also, a switch to direct the results from the terminal to the output-file *alterdata.txt* is included, in the case that the user want to use those after running *AlterBBN* in the fixed parameter case.

ARES is executed by giving a minimum of two input arguments; the first one determining the type of run (**single** or **multi**); the second one determining the type of cosmology (**paramfree**, **standard**, **darkdens**, **reheating** or **wimp**). The **paramfree** option is equivalent to running *AlterBBN* with no input argument, using the parameter-free SBBN scenario with $\eta_{10} = 6.10$, $\tau_n = 880.3$ and $N_{eff} = N_\nu = 3.046$. The other options are thoroughly explained in the above discussion. The default settings are η as the parameter to vary, with 25 values between the limits $\eta_{min} = 10^{-10}$ and $\eta_{max} = 10^{-9}$, as well as a log distribution of the 25 points. The default settings may be temporarily changed by providing further input

arguments. For an explanation of all the possible options, the program may be run with the one input argument **info**.

2.2.2 Correction of the Initial Time

The initial time for the BBN calculation is given by equation 2.28. However, this approximation is true only in the standard scenario. The original code includes the option of adding extra relativistic degrees of freedom to the mix, in the form of an unspecified "dark density". A positive value of the dark density will contribute to an increased expansion rate, leading to less elapsed time for a given temperature than in the SBBN scenario. It will not affect the abundances, since the dynamic variables T_9, h_η and ϕ_e only depends on the time-steps and not the absolute time at where they are analyzed. However, there are situations where we would want to keep track of the cosmic time. For example, in chapter 3 we plot the time evolution of the photon temperature for standard and WIMP scenarios, where it is essential to know the initial time.

The correction is based on the assumption that for high temperatures the expansion rate is inversely proportional to the time, or $H \propto t^{-1}$. This is a valid assumption at the high temperatures for our purposes, knowing that it will not impose uncertainties on the light element abundances. The new initial time is then given by

$$t_{\text{new}} = t_{\text{SBBN}} \frac{H_{\text{SBBN}}}{H_{\text{new}}} \, , \tag{2.42}$$

where t_{SBBN} is given by equation 2.28. Note that *AlterBBN* does not assume $H \propto t^{-1}$ when calculating the expansion rate, since this is not entirely true, and would impose uncertainties on the calculation of the relic abundances of the light elements. Thus H_{SBBN} is given by the energy densities of photons, neutrinos, $e^\pm$-pairs and baryons, while H_{new} also includes the dark density. In case that we (also) want to include WIMPs, there will be an (additional) correction factor for their contribution to the total energy density at the starting time (see chapter 3).
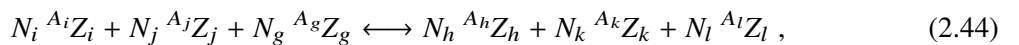
2.2.3 Extension of the Nuclear Network

In table 2.6 I have listed the full nuclear network of *AlterBBN*, including the new reactions, (marked by an asterisk). The change in the element abundances from extending the nuclear network can be seen in table 2.1, where the results are obtained from SBBN runs. We see that extending the nuclear network has a very small effect on the abundances. The largest differences are found in the estimates of D and ^6Li, but we also note that the uncertainties in these two predictions have increased.

The nuclear network in the original code only consists of reactions on the form 2.2, and is not generalized to the case of three-body reactions including three different nuclides. Amongst the new reactions added to the program is

$$^3He + \,^3H \longleftrightarrow n + p + \,^4He \, , \tag{2.43}$$

which includes three different nuclides on the right side. The code therefore had to be modified along the same lines as *NUC123* and *PArthENoPE* to cover this type of reaction as well. All reactions are now on the form

$$N_i \,^{A_i}Z_i + N_j \,^{A_j}Z_j + N_g \,^{A_g}Z_g \longleftrightarrow N_h \,^{A_h}Z_h + N_k \,^{A_k}Z_k + N_l \,^{A_l}Z_l \, , \tag{2.44}$$

and this leads to a simple extension of equation 2.3, which now reads

$$\frac{dY_i}{dt} = \sum_{j,g,h,k,l} N_i \left(-\frac{Y_i^{N_i} Y_j^{N_j} Y_g^{N_g}}{N_i! N_j! N_g!} \Gamma_{ijg \to hkl} + \frac{Y_h^{N_h} Y_k^{N_k} Y_l^{N_l}}{N_h! N_k! N_l!} \Gamma_{hkl \to ijg} \right) \, . \tag{2.45}$$

	Org. code	Ext. network
Y_p *	0.2472	0.2471
ΔY_p †	-	-0.04
δY_p ‡	0.045	0.045
$[D/H]_p \times 10^5$	2.5730	2.5780
$\Delta[D/H]_p$	-	0.19
$\delta[D/H]_p$	1.40	1.56
$[^3He/H]_p \times 10^5$	1.0240	1.0250
$\Delta[^3He/H]_p$	-	0.10
$\delta[^3He/H]_p$	4.29	3.55
$[^7Li/H]_p \times 10^9$	0.4567	0.4546
$\Delta[^7Li/H]_p$	-	-0.46
$\delta[^7Li/H]_p$	7.14	5.93
$[^6Li/H]_p \times 10^{14}$	1.1220	1.1350
$\Delta[^6Li/H]_p$	-	1.16
$\delta[^6Li/H]_p$	87.02	91.19
$[^7Be/H]_p \times 10^9$	0.4290	0.4269
$\Delta[^7Be/H]_p$	-	-0.49
$\delta[^7Be/H]_p$	7.25	5.93

Table 2.1: *The resulting abundances for two different AlterBBN runs. The first run was made with the original code, while the results from extending the nuclear network from 88 to 100 reactions are shown in the rightmost column. Both runs were made assuming SBBN, with $\eta_{10} = 6.10$, $N_\nu = 3.046$ and $\tau_n = 880.3$.*
* Central abundance value.
† Change in the abundance relative to the run made with the original code, given in percent.
‡ Linearly calculated abundance uncertainty, relative to the central abundance, given in percent.

Extending the program to be able to handle reactions on the form 2.43 involved modifying the function *int linearize* found in the routine *bbn.c*. In appendix A we discuss the relevant theory for making the extension from four to six nuclides. In table 2.2 I have listed the different reaction types found in the updated version of *AlterBBN*, together with the corresponding equations for finding $\Gamma_{ijg \to hkl}$ (equation A.11) and $\Gamma_{hkl \to ijg}$ (equation A.12). I have also given the values of the variables CN1, CN2, CN3, CN4, CN5 and CN6, which are needed in the numerical integration of equation 2.45. This involves building a matrix equation for the abundance changes, and the relevant steps in solving this matrix equation are given in [44]. A detailed discussion of this is beyond the scope of this project, but since we need the values of CN1-CN6 for the new type of reaction, I will briefly explain this step from the numerical recipe. By comparing equation E.7 in [44] with the method used in *PArthENoPE* (which is the same method as the one used in *AlterBBN*, except that in *PArthENoPE* the variables are written out in their full form), we find that

$$CN1 = \frac{N_i Y_i^{N_i-1} Y_j^{N_j} Y_g^{N_g}}{(N_i + N_j + N_g) N_i! N_j! N_g!} \Gamma_{ijg \to hkl} \ . \tag{2.46}$$

For CN2 and CN3 we have the same expression, only we switch i with j and i with g respectively. Likewise, we get

$$CN4 = \frac{N_h Y_h^{N_h-1} Y_k^{N_k} Y_l^{N_l}}{(N_h + N_k + N_l) N_h! N_k! N_l!} \Gamma_{hkl \to ijg} \ , \tag{2.47}$$

and we similarly switch h with k and h with l to find CN5 and CN6 respectively.

The energy output Q, and the reverse reaction coefficient C_{rev} are calculated externally and put into the matrix *double reacparam*, which is defined in the function *nucl* (and *nucl_failsafe*). The energy output from the reaction is simply the difference in excess masses, that is

$$Q = N_i dm_i + N_j dm_j + N_g dm_g - N_h dm_h - N_k dm_k - N_l dm_l \ , \tag{2.48}$$

Type	$(N_i,N_j,N_g,N_h,N_k,N_l)$	$\dfrac{\Gamma_{ijg \to hkl}}{\hat{f}_{ijg}}$	$\dfrac{\Gamma_{hkl \to ijg}}{C_{\text{rev}}\hat{f}_{ijg}e^{-11.605Q_6/T_9}}$	$\dfrac{(CN1,CN2,CN3)}{\Gamma_{ijg \to hkl}}$	$\dfrac{(CN4,CN5,CN6)}{\Gamma_{hkl \to ijg}}$
0	(1,0,0,0,0,1)	-	-	(1,0,0)	(0,0,1)
1	(1,1,0,0,0,1)	ρ_b	$0.987 \cdot 10^{10} T_9^{3/2}$	$(Y_j/2,Y_i/2,0)$	(0,0,1)
2	(1,1,0,0,1,1)	ρ_b	ρ_b	$(Y_j/2,Y_i/2,0)$	$(0,Y_l/2,Y_k/2)$
3	(1,0,0,0,0,2)	-	-	(1,0,0)	$(0,0,Y_l/2)$
4	(1,1,0,0,0,2)	ρ_b	ρ_b	$(Y_j/2,Y_i/2,0)$	$(0,0,Y_l/2)$
5	(2,0,0,0,1,1)	ρ_b	ρ_b	$(Y_i/2,0,0)$	$(0,Y_l/2,Y_k/2)$
6	(3,0,0,0,0,1)	ρ_b^2	$0.974 \cdot 10^{20} T_9^3$	$(Y_i^2/6,0,0)$	(0,0,1)
7	(2,1,0,0,0,1)	ρ_b^2	$0.974 \cdot 10^{20} T_9^3$	$(Y_jY_i/3,Y_i^2/6,0)$	(0,0,1)
8	(1,1,0,0,1,2)	ρ_b	$1.013 \cdot 10^{-10} T_9^{-3/2} \rho_b^2$	$(Y_j/2,Y_i/2,0)$	$(0,Y_l^2/6,Y_kY_l/3)$
9	(1,1,0,0,0,3)	ρ_b	$1.013 \cdot 10^{-10} T_9^{-3/2} \rho_b^2$	$(Y_j/2,Y_i/2,0)$	$(0,0,Y_l^2/6)$
10	(2,0,0,0,2,1)	ρ_b	$1.013 \cdot 10^{-10} T_9^{-3/2} \rho_b^2$	$(Y_i/2,0,0)$	$(0,Y_lY_k/3,Y_k^2/6)$
11 (new)	(1,1,0,1,1,1)	ρ_b	$1.013 \cdot 10^{-10} T_9^{-3/2} \rho_b^2$	$(Y_j/2,Y_i/2,0)$	$(Y_kY_l/3,Y_hY_l/3,Y_hY_k/3)$

Table 2.2: First column: The 12 different reaction types in the updated AlterBBN *version. Second column: The number of nuclides involved in each reaction type, according to equation 2.44. Third column: The forward reaction rate used in equation 2.45, given by equation A.11 (divided by the tabulated reaction rate). Fourth column: The reverse reaction rate used in equation 2.45, given by equation A.12 (divided by the tabulated (forward) reaction rate, the reverse reaction coefficient and the exponential in the reverse rate equation, which are all common factors for all reaction types). Fifth column: The three variables CN1, CN2 and CN3 given by equation 2.46 (divided by the forward reaction rate). Sixth column: The three variables CN4, CN5 and CN6 given by equation 2.47 (divided by the reverse reaction rate). The reaction p ↔ n (type 0) is computed in a separate function in the routine bbnrate.c, which gives Γ as output. The rest of the weak reaction rates are independent of temperature and tabulated as constants in the form of Γ. Hence $\Gamma = \hat{f}$ and we do not have to use equations A.11 and A.12 for reactions of types 0 and 3.*

where dm_i is the excess mass of nuclide i. While computing C_{rev} and Q for the new reactions, I did a consistency check on the values used in the original code, and realized that they did not entirely correspond. Doing SBBN runs with both the original and new set of values, varying η in the range $[10^{-10},10^{-9}]$, I found a relative difference of up to $\sim 2\%$ for C_{rev} and $\sim 0.2\%$ for Q. There might be some discrepancies between some of the input parameters in *AlterBBN* and how they are computed in *PArthENoPE* [58]. In *PArthENoPE*, C_{rev} and Q are calculated inside the program by using equations A.10 and 2.48. It is difficult to explain a $\sim 2\%$ difference in the values of C_{rev} simply by round-offs to a lower precision, thus I suspect that further simplifications of equation A.10 have been made to obtain the values found in *double reacparam* in the original *AlterBBN* code. In table 2.1 I have listed the resulting element abundances for a parameter-free SBBN run, using both the old and the new set of values for C_{rev} and Q, only including the original nuclear reaction network. Notice that the change in abundances going from the old set to the new set reach a maximum of 0.5% which is well within the theoretical uncertainties on the reaction rates. However, I do not like to impose unnecessary uncertainties where it could be avoided, so the updated *AlterBBN* will use equation A.10 for the reverse reaction coefficient together with my updated values for the energy output.

2.2.4 Updated Nuclear Rates

The task of computing the light element abundances from BBN relies heavily on the nuclear reaction cross sections. In fact, theoretical uncertainties in the abundance predictions are dominated by uncertainties imposed by the nuclear rates, except for the prediction of the ^4He abundance, which is dominated by uncertainties in the neutron lifetime and Newton's gravitational constant [59]. In table 2.3 I have listed the leading nuclear reactions in the predictions of the abundances (left table) and the leading nuclear re-

actions in the predictions of the uncertainties (right table) [59]. Most of the reaction rates in the original code regarding these reactions are taken from Serpico et al. 2004 [56], the exceptions being reaction 28 and 29 (Pisanti et al. 2007 [45]).

Reaction number	Reaction
1	$p \longleftrightarrow n$
12	$p(n,\gamma)D$
20	$D(p,\gamma)^3He$
28	$D(D,n)^3He$
29	$D(D,p)^3H$
16	$^3He(n,p)^3H$
30	$^3H(D,n)^4He$
31	$^3He(D,p)^4He$
27	$^3He(\alpha,\gamma)^7Be$
26	$^3H(\alpha,\gamma)^7Li$
17	$^7Be(n,p)^7Li$
24	$^7Li(p,\alpha)^4He$

Reaction number	Reaction
28	$D(D,n)^3He$
29	$D(D,p)^3H$
20	$D(p,\gamma)^3He$
27	$^3He(\alpha,\gamma)^7Be$
31	$^3He(D,p)^4He$

Table 2.3: Left table: The nuclear reactions dominating the predictions of the light element abundances. Right table: The nuclear reactions dominating the prediction of the uncertainties. The reaction number is the number each reaction is given in AlterBBN*, as presented in table 2.6.*

Recent work by Coc et al. 2015 [55] has provided more precise rates for the deuterium destruction reactions number 20, 28 and 29, which I have added to *AlterBBN*. The article presents tabulated values of the reaction rates for temperatures between 0.001 and 10 GK (see table B.3 in appendix B). For temperatures above 10 GK I set both the reaction rates and the uncertainties to zero, which is a valid assumption for all rates except the weak reaction(s) that transform $p \leftrightarrow n$ [60]. At high temperatures the nuclei disintegrate as soon as they form, that is, they are in nuclear statistical equilibrium. This means that their abundances do not depend on the reaction rates. Of course, there are small deviations from nuclear statistical equilibrium already at temperatures ~ 10 GK. However, since it is difficult to measure rates at such high temperatures we often rely on extrapolations from lower temperatures, which may impose large uncertainties on the estimates. The other extreme is that the program may run below the tabulated temperatures, in which case I have set the rates and uncertainties for reactions number 20, 28 and 29 equal to the values corresponding to the lowest temperatures. However, there is no apparent reason for running *AlterBBN* to temperatures below 0.001 GK, since BBN has run its course by then.

New data is also available for reaction rate number 12 through the work of Ando et al. 2004 [52]. This is the reaction that produces deuterium from protons and neutrons and thus a key step in the production of the other light elements. Best-fit formulas for the reaction rate and the corresponding uncertainty are found in appendix B. The authors report a very good agreement between their work and previous theoretical estimations for energies below 0.1 MeV. However, at $E = 0.5$ and $E = 1.0$ MeV they find significant differences from other theoretical estimations they are comparing with, suggesting better experimental measurements of the n/p-capture cross sections at these energies before any conclusion can be made. Therefore I use this rate only for $T_9 < 1.5$, which correspond to ~ 0.13 MeV. This is right before the deuterium bottleneck is breached, so the new rate will cover the most important stages of BBN. For

	Org. rates	Rate 12	Rate 19	Rate 20	Rate 27	Rate 28	Rate 29	**All new**
Y_p *	0.2471	0.2471	0.2471	0.2471	0.2471	0.2471	0.2472	**0.2472**
ΔY_p †	-	0.00	0.00	0.00	0.00	0.00	0.04	**0.04**
δY_p ‡	0.045	0.045	0.045	0.045	0.045	0.045	0.045	**0.045**
$[D/H]_p \times 10^5$	2.5780	2.5820	2.5780	2.5290	2.5780	2.5500	2.5140	**2.4560**
$\Delta[D/H]_p$	-	0.16	0.00	-1.90	0.00	-1.09	-2.48	**-4.73**
$\delta[D/H]_p$	1.56	1.55	1.56	1.70	1.56	1.64	1.65	**2.31**
$[^3He/H]_p \times 10^5$	1.0250	1.0250	1.0250	1.0440	1.0250	1.0260	1.0090	**1.0330**
$\Delta[^3He/H]_p$	-	0.00	0.00	1.85	0.00	0.10	-1.56	**0.78**
$\delta[^3He/H]_p$	3.55	3.55	3.55	3.63	3.55	3.60	3.56	**4.54**
$[^7Li/H]_p \times 10^9$	0.4546	0.4520	0.4601	0.4712	0.5079	0.4617	0.4576	**0.5383**
$\Delta[^7Li/H]_p$	-	-0.57	1.21	3.65	11.73	1.56	0.66	**18.41**
$\delta[^7Li/H]_p$	5.93	5.95	5.84	5.95	6.22	5.89	5.88	**7.53**
$[^6Li/H]_p \times 10^{14}$	1.1350	1.1360	1.1350	1.1130	1.1350	1.1230	1.1070	**1.0810**
$\Delta[^6Li/H]_p$	-	0.09	0.00	-1.94	0.00	-1.06	-2.47	**-4.76**
$\delta[^6Li/H]_p$	91.19	91.20	91.19	91.38	91.19	91.36	91.24	**86.57**
$[^7Be/H]_p \times 10^9$	0.4269	0.4243	0.4322	0.4437	0.4784	0.4342	0.4305	**0.5095**
$\Delta[^7Be/H]_p$	-	-0.61	1.24	3.94	12.06	1.71	0.84	**19.35**
$\delta[^7Be/H]_p$	5.93	5.94	5.84	5.96	6.26	5.89	5.89	**7.76**

Table 2.4: The change in abundances (central values) from updating the reaction rates. Second column: Reference run, same as last run in table 2.1. Third-eight column: Adding each of the new nuclear rates separately. Ninth column: The effect of including all six updated nuclear rates. All runs were made with the SBBN parameters $\eta_{10} = 6.10$, $N_\nu = 3.046$ and $\tau_n = 880.3$. Note that the reference run in the second column is not the original code, but the one with extended nuclear network from the last column in table 2.1. Thus the value in the second row for each "element box" must not be confused with being the overall change relative to the original code. The overall changes are found in table 2.5.
* Central abundance value. For Y_p this is relative to the total baryon abundance, while the rest is given relative to the hydrogen abundance.
† Change in the abundance relative to the reference run in column two, given in percent.
‡ Linearly calculated abundance uncertainty, relative to the central abundance, given in percent.

Y_p	$[D/H]_p$	$[^3He/H]_p$	$[^7Li/H]_p$	$[^6Li/H]_p$	$[^7Be/H]_p$
0.00	-4.55	0.88	17.88	-3.65	18.77

Table 2.5: The overall relative changes in the prediction of the primordial abundances for all the updates made to AlterBBN regarding the nuclear network and the reaction rates.

higher temperatures I follow the suggestion from Serpico et al. 2004 [56] [3] and use the reaction rate from Smith et al. [61].

Finally, I have updated the rates of the ^7Be production/destruction reactions $^3He(\alpha, \gamma)^7Be$ [54] (number 27) and $^7Be(n, \alpha)^4He$ [53] (number 19). The authors of both papers have provided best-fit formulas which are used here, and can be found in appendix B. However, the uncertainties for reaction number 19 are evaluated for specific temperatures, restated in table B.1, and extended to a continuous set of temperature ranges in the code. This reaction is not listed in table 2.6, since it is not among the most important reactions for the predictions of the abundances and the uncertainties. However, although it is not important for the predictions of deuterium and helium, it will have a non-trivial effect on the prediction of primordial ^7Li. The lithium problem can not be explained solely in terms of a "nuclear solution" (see chapter 1.2), but more accurate nuclear reaction rates may shorten the gap between the observed and

---

[3] This is where the previous rate for the reaction was taken from, also valid only for $T_9 < 1.5$.

the predicted abundance. The $^7Be(n,\alpha)^4He$ reaction is amongst the key sources of ^7Be destruction [53], which highly affects the post-BBN ^7Li abundance (chapter 1.2). The original *AlterBBN*-adopted rate of this reaction is from Wagoner 1969 [43]. Work done by Hou et al. 2015 [53] suggests that Wagoner overestimates the rate by a factor of ten, and is only to be considered as an upper limit. Experimental results regarding the rate and uncertainty of this reaction are listed in table B.1 in appendix B, together with the best-fit parametric formula used in calculating the reaction rate. As concluded in ref. [53], the new rate is more accurate but worsens the lithium problem by 1.2%.

The effect on the relic abundances from including the new reactions is seen in table 2.4. Be aware that the column marked "Org. rates" is not a run made with the original code, but with the extended nuclear network, seen in the last column in table 2.1. The overall changes in the predictions of the primordial abundances are listed in table 2.5.

2.2.5   The Initial Electron-Positron Entropy Density

From equation 2.4 we see that we need to know the entropy density of the $e^\pm$-pairs at the starting temperature in order to estimate the initial value of h_η. In the original code the $e^\pm$-pairs are assumed to be highly relativistic at the onset of the calculations, thus the ratio of their entropy density to the photon entropy density is $s_{e^\pm}/s_\gamma = 7/4$. For very high starting temperatures this is a very good assumption indeed. However, since it is recommended to start the iterations at around neutrino decoupling (see discussion in section 2.3), a natural starting point is for temperatures in the range $T_{9,i} \sim 20-30$. At 2.0 MeV the entropy ratio is reduced to 6.95/4 [23] since the $e^\pm$-pairs have started to become non-relativistic. In the right panel in figure 2.1 the deuterium yield is plotted for different starting temperatures, assuming an instantaneous neutrino decoupling temperature of 2.3 MeV. The blue solid line in the main window is the yield results from using the corrected entropy density, while the results from using the ultra-relativistic assumption is shown as the dashed orange line. The light blue lines on each side of the corrected yields shows the uncertainty in the predictions, while the horizontal band correspond to the observational constraints. There is a $\sim 0.7\%$ increase in the deuterium abundance for $T_{9,i} = 27$, while the difference is slightly larger using lower starting temperatures.

The correction of the initial $e^\pm$ entropy density is calculated using the full expressions for their energy density (equation 2.17) and pressure (equation 2.18). These equations need the electron degeneracy parameter ϕ_e as input, which again is dependent on h_η, so we have come to a full circle. However, looking at the left panel in figure 2.1 we see that ϕ_e is vanishingly small at the high starting temperatures, and we can safely set this to zero.

2.3   Iteration Parameters: General Remarks And Recommended Values

The general consensus is that Big Bang Nucleosynthesis happens between ~ 1 MeV and ~ 70 keV, which are the temperatures of a more or less fully freeze-out of the weak interactions and the end of the deuterium bottleneck respectively. The weak freeze-out is not an abrupt process, and as mentioned in chapter 1.1.6, the freeze-out process starts already at temperatures $\sim 2-3$ MeV. Enqvist et al. [62] recommend using $T_{\nu d} = 2.3$ MeV for the decoupling temperature when assuming instantaneous neutrino decoupling. Starting the iteration at the time of neutrino decoupling simplifies some of the physics implemented in the program, so I have decided to use $T_{9,i} = 27$ as the initial temperature for the calculations in this project. In chapter 3 we will discuss the results of Nollett & Steigman [48] [25] in the light of the implementation of light WIMPs in *AlterBBN*, and their calculations are based on an instantaneous neutrino decoupling temperature of $T_{\nu d} = 2.0$ MeV. Although the effect is very small, we see in the right panel of figure 2.1 that the resulting deuterium abundance is somewhat sensitive to the starting temperature. For unknown reasons the uncertainty seems to fluctuate a bit for differing initial temperatures,
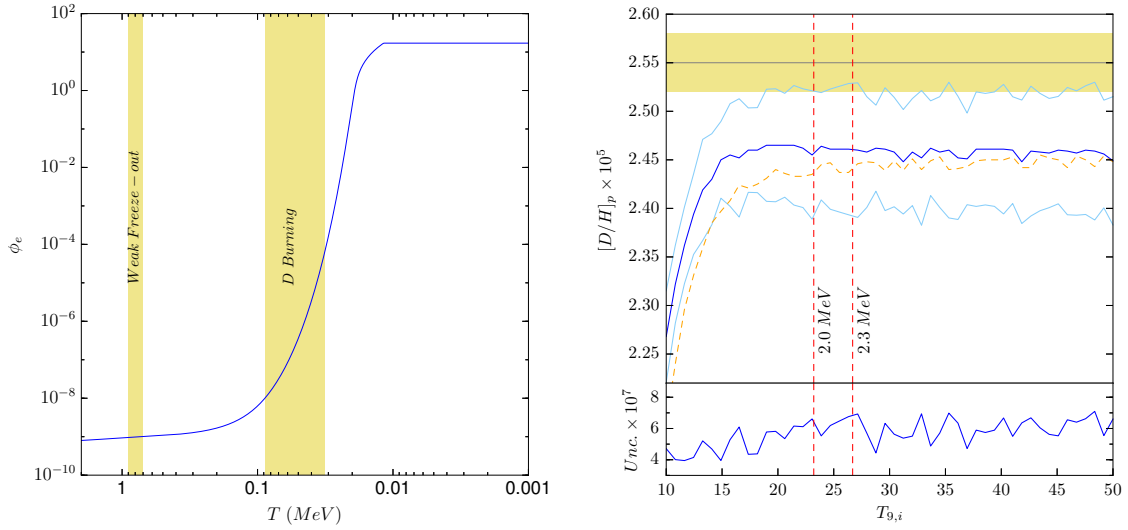
Figure 2.1: Left panel: The electron degeneracy parameter $\phi_e = m_e/T_9$ plotted against the temperature, with the colored vertical bands corresponding to the times of weak n/p freeze-out and deuterium burning (effective BBN) respectively. Right panel: The deuterium yield, plotted for different initial temperatures, assuming instantaneous neutrino decoupling at $T_{\nu d} = 27$ (~ 2.3 MeV) and SBBN. The blue solid line in the upper window is the yield from using the corrected $e^\pm$ entropy density, while the dashed orange line is for the assumption of highly relativistic $e^\pm$-pairs. The lighter blue lines show the uncertainty in the predictions, which is also plotted in the bottom window. The horizontal band is the observed constraint on the primordial deuterium abundance.

tending towards lower uncertainties for lower starting temperatures. This is shown in the bottom window in the right panel of the figure. At around 15 MeV the electrons and positrons start annihilating, and one should avoid starting any later than this, as it would underestimate the expansion rate.

There are good reasons not to start the integration process even earlier, aside from the obvious fact that the computational time goes down, and that not much of importance happens when all the BBN-relevant particles are still in thermodynamic equilibrium. Starting at e.g. $T_{9,i} \sim 100$ the muons may still be semi-relativistic ($m_\mu = 105.7$ MeV) and not fully annihilated. This introduces extra relativistic degrees of freedom and a potential error when employing entropy conservation in finding the initial value of h_η (equation 2.4). At the time of weak freeze-out, the mouns have become fully non-relativistic, and we don't have to take them into account. In the scenario of including light WIMPs it is necessary to deal explicitly with neutrino decoupling, and it is therefore convenient to start the iterations right after neutrino decoupling. Also in the standard scenario it is a useful assumption, since it simplifies the set of equations governing the iteration. Knowing this is crucial in the case where the user would want to start the iterations at a higher temperature. Not only is η found by conservation of entropy at the time of neutrino decoupling, but the expression for the neutrino energy density is based on the assumption that $T_\nu \propto a^{-1}$, which is strictly true only after the neutrinos have decoupled. In the case of a neutrino coupled WIMP, however, it was necessary to promote T_ν to a dynamic variable, similar to T_9, since the annihilation of the WIMP will heat the neutrinos relative to the photons. The necessary changes in this case are discussed in chapter 3.

The initial temperature may be changed by the user through the *.ini* input-file, but I have found no reason to include this option for the final temperature. I have set this to $T_{9,f} = 0.01$, which corresponds to ~ 1 keV. By this time the BBN has ended in earnest, and the light element abundances have frozen out (except from the decay of ^3H and ^7Be into ^3He and ^7Li respectively).

In the main function *nucl* a set of iteration parameters that controls the adaptive step-size for the Runge-Kutta driver are defined. Each time-step is determined by the requirement that the abundances and temperature do not change too much, and the controlling parameters are

- CY - the maximum change in the abundances, $(dY/dt)_{max}$;

- CT - the maximum change in the temperature, $(dT/dt)_{max}$;

- DT0 - initial time-step;

- NITMAX - maximum number of recorded iterations;

- INC - maximum number of increments before recording.

It is important to have a set of parameters which ensures that the iteration process runs all the way from the initial to the final temperature, otherwise the iteration may stop before the BBN has ended. As a default, the original program uses the values $CY = 0.1$, $CT = 0.01$, $DT0 = 10^{-4}$, $NITMAX = 1000$ and $INC = 50$ for the calculation of the abundances. However, for the uncertainty estimation the default values are $CY = 0.5$, $CT = 0.1$, $DT0 = 10^{-2}$, and $NITMAX = 10$, keeping INC unaltered. If the uncertainties computed in the default scenario do not satisfy some specified conditions, the function *nucl_failsafe* "kicks" in. This function is a copy of the function *nucl*, except that the iteration parameters are adjusted to the values they have for the abundance calculation. In my view, the conditions for activating *nucl_failsafe* is too conservative if one is interested in getting a good estimate of the uncertainties. Comparing runs where the default iteration parameters are used, with runs where the uncertainties are analyzed with the same time-steps as for the abundance calculation, the resulting uncertainties may differ by several percent. For this reason, when the uncertainties are of interest, I will use the same set of iteration parameters for both the abundance and uncertainty calculation. This way, we ensure that they are analyzed at the same points. When only the abundances are of interest, the default values may just as well be used to shorten the computation time.

2.4   Discussion

With the updates and changes of *AlterBBN* there have been a significant decrease in the predicted deuterium abundance. In the original code this was estimated to $[D/H]_p = 2.573 \pm 0.036 \cdot 10^{-5}$ assuming SBBN, while the updated *AlterBBN* have seen this drop by $\sim 4.5\%$ to $2.456 \pm 0.057 \cdot 10^{-5}$, still just within the suggested observational constraint of $2.55 \pm 0.03 \cdot 10^{-5}$. We also note that the lithium problem is worsened, with a major increase in both the relic ^7Li and ^7Be yields. The ^4He abundance was not affected at all, still being $Y_p = 0.2472 \pm 0.0001$, which is within the suggested observational constraint of 0.2449 ± 0.004. Except for ^4He and ^6Li there have been an overall increase in the uncertainties, with the uncertainty in the deuterium prediction now being 2.3%, mainly arriving from the extended nuclear network and the rates for the reactions $D(p,\gamma)^3He$, $D(D,n)^3He$ and $D(D,p)^3H$ from Coc et al. [55]. It is evident that accurate nuclear rates are essential for predicting the light element abundances, as we have seen significant impacts on the predictions and the uncertainties only by updating six of the reaction rates.

Since the initial value of several of the parameters needed in the iteration relies on entropy conversion at the time of neutrino decoupling, it is recommended to start the iterations here. In relaxing the assumption of ultra-relativistic $e^{\pm}$-pairs at the corresponding temperatures, we found an increase by $\sim 0.7\%$ in the resulting deuterium yield, with a minor dependence on the initial temperature.

nb	ref	reaction	nb	ref	reaction	nb	ref	reaction
1	[61]	$n \leftrightarrow p$	35*	[70]	$^3He + {}^3H \rightarrow \gamma + {}^6Li$	69	[44]	$^8Li + p \rightarrow n + \alpha + {}^4He$
2	[63]	$^3H \rightarrow e^- + \nu + {}^3He$	36*	[67]	$^6Li + D \rightarrow n + {}^7Be$	70	[44]	$^8B + n \rightarrow p + \alpha + {}^4He$
3	[64]	$^8Li \rightarrow e^- + \nu + 2{}^4He$	37*	[67]	$^6Li + D \rightarrow p + {}^7Li$	71	[68]	$^9Be + p \rightarrow D + \alpha + {}^4He$
4	[65]	$^{12}B \rightarrow e^- + \nu + {}^{12}C$	38*	[68]	$^3He + {}^3H \rightarrow D + {}^4He$	72	[68]	$^{11}B + p \rightarrow 2\,\alpha + {}^4Be$
5	[66]	$^{14}C \rightarrow e^- + \nu + {}^{14}N$	39*	[68]	$^3H + {}^3H \rightarrow 2\,n + {}^4He$	73	[43]	$^{11}C + n \rightarrow 2\,\alpha + {}^4He$
6	[64]	$^8B \rightarrow e^+ + \nu + 2{}^4He$	40*	[68]	$^3He + {}^3H \rightarrow n + p + {}^4He$	74	[43]	$^{12}C + n \rightarrow \gamma + {}^{13}C$
7	[65]	$^{11}C \rightarrow e^+ + \nu + {}^{11}B$	41*	[71]	$^7Li + {}^3H \rightarrow n + {}^9Be$	75	[43]	$^{13}C + n \rightarrow \gamma + {}^{14}C$
8	[65]	$^{12}N \rightarrow e^+ + \nu + {}^{12}C$	42*	[56]	$^7Be + {}^3H \rightarrow p + {}^9Be$	76	[43]	$^{14}N + n \rightarrow \gamma + {}^{15}N$
9	[66]	$^{13}N \rightarrow e^+ + \nu + {}^{13}C$	43*	[56]	$^7Li + {}^3He \rightarrow p + {}^9Be$	77	[69]	$^{13}N + n \rightarrow p + {}^{13}C$
10	[66]	$^{14}O \rightarrow e^+ + \nu + {}^{14}N$	44	[43]	$^7Li + n \rightarrow \gamma + {}^8Li$	78	[68]	$^{14}N + n \rightarrow p + {}^{14}C$
11	[66]	$^{15}O \rightarrow e^+ + \nu + {}^{15}N$	45	[43]	$^{10}B + n \rightarrow \gamma + {}^{11}B$	79	[69]	$^{15}O + n \rightarrow p + {}^{15}N$
12†	[52]	$H + n \rightarrow \gamma + {}^2H$	46	[67]	$^{11}B + n \rightarrow \gamma + {}^{12}B$	80	[68]	$^{15}O + n \rightarrow \alpha + {}^{12}C$
13	[43]	$^2H + n \rightarrow \gamma + {}^3H$	47	[68]	$^{11}C + n \rightarrow p + {}^{11}B$	81	[69]	$^{12}C + p \rightarrow \gamma + {}^{13}N$
14	[43]	$^3He + n \rightarrow \gamma + {}^4He$	48	[69]	$^{10}B + n \rightarrow \alpha + {}^7Li$	82	[69]	$^{13}C + p \rightarrow \gamma + {}^{14}N$
15	[67]	$^6Li + n \rightarrow \gamma + {}^7Li$	49	[69]	$^7Be + p \rightarrow \gamma + {}^8B$	83	[68]	$^{14}C + p \rightarrow \gamma + {}^{15}N$
16	[56]	$^3He + n \rightarrow p + {}^3H$	50	[68]	$^9Be + p \rightarrow \gamma + {}^{10}B$	84	[68]	$^{13}N + p \rightarrow \gamma + {}^{14}O$
17	[56]	$^7Be + n \rightarrow p + {}^7Li$	51	[69]	$^{10}B + p \rightarrow \gamma + {}^{11}C$	85	[68]	$^{14}N + p \rightarrow \gamma + {}^{15}O$
18	[68]	$^6Li + n \rightarrow \alpha + {}^3H$	52	[69]	$^{11}B + p \rightarrow \gamma + {}^{12}C$	86	[68]	$^{15}N + p \rightarrow \gamma + {}^{16}O$
19†	[53]	$^7Be + n \rightarrow \alpha + {}^4He$	53	[68]	$^{11}C + p \rightarrow \gamma + {}^{12}N$	87	[69]	$^{15}N + p \rightarrow \alpha + {}^{12}C$
20†	[55]	$^2H + p \rightarrow \gamma + {}^3He$	54	[43]	$^{12}B + p \rightarrow n + {}^{12}C$	88	[68]	$^{12}C + \alpha \rightarrow \gamma + {}^{16}O$
21	[68]	$^3H + p \rightarrow \gamma + {}^4He$	55	[69]	$^9Be + p \rightarrow \alpha + {}^6Li$	89	[43]	$^{10}B + \alpha \rightarrow p + {}^{13}C$
22	[69]	$^6Li + p \rightarrow \gamma + {}^7Be$	56	[69]	$^{10}B + p \rightarrow \alpha + {}^7Be$	90	[68]	$^{11}B + \alpha \rightarrow p + {}^{14}C$
23	[56]	$^6Li + p \rightarrow \alpha + {}^3He$	57	[43]	$^{12}B + p \rightarrow \alpha + {}^9Be$	91	[69]	$^{11}C + \alpha \rightarrow p + {}^{14}N$
24	[56]	$^7Li + p \rightarrow \alpha + {}^4He$	58	[68]	$^6Li + \alpha \rightarrow \gamma + {}^{10}B$	92	[68]	$^{12}N + \alpha \rightarrow p + {}^{15}O$
25	[69]	$^2H + \alpha \rightarrow \gamma + {}^6Li$	59	[69]	$^7Li + \alpha \rightarrow \gamma + {}^{11}B$	93	[68]	$^{13}N + \alpha \rightarrow p + {}^{16}O$
26	[56]	$^3H + \alpha \rightarrow \gamma + {}^7Li$	60	[69]	$^7Be + \alpha \rightarrow \gamma + {}^{11}C$	94	[68]	$^{10}B + \alpha \rightarrow n + {}^{13}N$
27†	[56]	$^3He + \alpha \rightarrow \gamma + {}^7Be$	61	[43]	$^8B + \alpha \rightarrow p + {}^{11}C$	95	[68]	$^{11}B + \alpha \rightarrow n + {}^{14}N$
28†	[55]	$^2H + D \rightarrow p + {}^3He$	62	[67]	$^8Li + \alpha \rightarrow n + {}^{11}B$	96	[43]	$^{12}B + \alpha \rightarrow n + {}^{15}N$
29†	[55]	$^2H + D \rightarrow n + {}^3H$	63	[68]	$^9Be + \alpha \rightarrow n + {}^{12}C$	97	[69]	$^{13}C + \alpha \rightarrow n + {}^{16}O$
30	[56]	$^3H + D \rightarrow n + {}^4He$	64	[44]	$^9Be + D \rightarrow n + {}^{10}B$	98*	[72]	$^{11}B + D \rightarrow p + {}^{12}B$
31	[56]	$^3He + D \rightarrow p + {}^4He$	65	[44]	$^{10}B + D \rightarrow p + {}^{11}B$	99*	[72]	$^{12}C + D \rightarrow p + {}^{13}C$
32	[69]	$^3He + {}^3He \rightarrow 2\,p + {}^4He$	66	[44]	$^{11}B + D \rightarrow n + {}^{12}C$	100*	[72]	$^{13}C + D \rightarrow p + {}^{14}C$
33	[56]	$^7Li + D \rightarrow n + \alpha + {}^4He$	67	[68]	$^4He + \alpha + n \rightarrow \gamma + {}^9Be$			
34	[68]	$^7Be + D \rightarrow p + \alpha + {}^4He$	68	[68]	$^4He + 2\,\alpha \rightarrow \gamma + {}^{12}C$			

Table 2.6: The updated nuclear network of AlterBBN.
* New reaction.
† Updated reaction rate.

Chapter 3

New Physics

The observational evidence for dark matter is overwhelming. It suggests that $\sim 26\%$ of the total energy content of the universe, or $\sim 84\%$ of its total mass-energy is in the form of non-luminous matter. The flat rotation curves in spiral galaxies, gravitational lensing effects and X-ray observations of galaxy clusters, to mention a few, indicate that galaxies and galaxy clusters consist of more mass than the eye can see (visit e.g. [73] or [74] for a nice review of the current observational evidence).

We group dark matter into "hot", "warm" and "cold" candidates, depending on their relativistic nature at the time of dark matter decoupling. As they freeze out, particle/anti-particle pairs annihilate, heating the remaining plasma in the process. *Hot dark matter* are particles with the same mass scale as neutrinos ($\ll$ keV), being relativistic at the time they decouple. Due to this property they are not likely to influence the ratio of neutrino-to-photon temperature as no entropy is released to the neutrino or photon fluids. However, they will affect BBN through the contribution to the relativistic energy density and thus the expansion rate of the early universe. Because of their relativistic nature, it is difficult to explain structure formation solely in terms of hot dark matter candidates. They will tend to erase density fluctuations on small scales, while contributing positively to large scale fluctuations. This leads to a very slow, "top-down" structure formation process, where large galaxy clusters are formed late in the history of the universe, before smaller structures, and this is not how we observe the history of the universe through the CMB [75]. Although there is some debate about whether hot dark matter may have been produced non-thermally (not in thermal equilibrium with the standard model particles in the early universe) may explain the observed *hierarchical* structure formation (see e.g. [76]) in agreement with CMB measurements, most models suggest *cold dark matter* candidate(s), or possibly a combined scenario where the majority of the dark matter is cold, with a minor hot/warm contribution (see e.g. [75] and [77]). The cold dark matter consist of particles of hundreds of MeV or heavier that are non-relativistic and thus not influencing the expansion rate at the times relevant for BBN. Their large mass also means that they freeze-out well before neutrino decoupling, leading to an unaltered neutrino to photon temperature ratio (since neutrinos are in equilibrium with the photons). The presence of cold dark matter therefore have no significant impact on the relic light element abundances. *Warm dark matter* provide candidates in the mass-interval between hot and cold dark matter, and may, or may not influence BBN, depending on their relativistic nature as they decouple from the primordial plasma. An example of such a candidate is the earlier introduced sterile neutrinos, which is to be further discussed in this chapter. Candidates that decouple and become non-relativistic (freeze out) in the time between neutrino decoupling and the end of BBN will both affect the expansion rate and the neutrino-to-photon temperature. Such candidates will leave their imprint on the light element abundances, and are therefore of particular interest in BBN analysis.

3.1 Dark Matter Candidates

Several dark matter candidates have been proposed as possible explanations for the missing matter (see e.g. [78] for a short review of the most popular candidates). One of those involves *MACHOs*, or MAssive Compact Halo Objects, suggesting a baryonic fix to the dark matter problem. This is a categorization of all astrophysical objects that may be hidden from our view, like black holes, brown dwarfs and neutron stars. However, observations of gravitational microlensing (the changing brightness of a distant object due to the interference of a nearby object) caused by possible MACHOs in the Milky Way halo has revealed that such objects can only account for a very small percentage of the non-luminous mass in our galaxy (e.g. [79] and [80]). Baryonic solutions to the problem are in general ruled out, since the baryonic matter density emerging from both BBN simulations and CMB measurements is not high enough to explain the growth of the presently observed structures in the universe (e.g. galaxies, clusters, filaments), given the smooth initial conditions observed in the CMB. Instead CMB measurements tell us that the total mass density is about five times that of the baryonic mass density [81], suggesting that we ought to look somewhere else for the missing matter.

The *standard model neutrinos* was long considered a promising dark matter candidate due to their expectedly non-zero masses. However, experiments have shown that, although at least two of the standard model neutrinos must have a non-zero mass [13] [14], the upper limit on the masses are not enough to explain all the missing matter [82], rather just a few percent ($\Omega_\nu \ll \Omega_{DM}$). One possibility is that the left-handed/right-handed standard model neutrinos/anti-neutrinos have yet undetected right-handed/left-handed counterparts. The fact that neutrinos have only been observed (within the margin of error from the uncertainty principle) with left-handed *helicity*, which means that the spin is anti-parallel to the momenta, is unexpected from a particle physics' point of view. All other fermions are known to have both left- and right-handed components so it is a big puzzle that the standard model neutrinos apparently possess this property. If left-handed neutrinos actually do exist, and they interact through the weak force they would have to be very heavy, beyond the scope of today's detection methods. If not, they should have been detected by now.

Sterile neutrinos are hypothetical particles postulated in 1994 by Dodelson and Widrow [83], that do not take part in the weak interactions but only interact gravitationally with the standard model particles. The term usually refers to neutrinos with right-handed helicity, and is therefore linked to the above discussion. Since they are not charged under the weak interaction they may be very light and still be beyond direct detection. They are generally considered to be quite heavy (few keV) compared to the standard model neutrinos and may thus contribute to the BBN as equivalent neutrinos. If so, they could be a significant contributor to the total dark matter density.

Supersymmetry (see e.g. [84] for an introduction on the topic) is a theory that has emerged from particle physics, which imposes a supersymmetric partner for each of the standard model particles, with a spin that differs by one half. This means that there is a fermionic equivalent for each boson, and vice versa. For this theory to be correct there must be a spontaneous symmetry breaking at some high-energy scale, which in general terms means that a physical system in a symmetric state is transformed to an asymmetric state. The reason for this is that in an "unbroken" supersymmetric theory, the supersymmetric partners would have the same mass and internal quantum numbers (except spin) as their equivalents. However, if they had the same mass, they should be discovered by now. The popular description is that the supersymmetric particles have masses that exceeds the present detection methods, and consequently the energy scale of the symmetry breaking must be high. Spontaneously broken supersymmetry may solve many mysteries in particle physics, including the potential of explaining the mass of the Higgs boson and the *hierarchy problem*, which concerns the problem of explaining why the elementary particles have the masses they do. Actually, the 126 GeV mass of the Higgs boson discovered in 2012 [10] is very difficult to explain solely in terms of the standard model, which suggest a much higher mass. Supersymmetry may be able to naturally explain this mass (see [85] for a review of the Higgs mass in the light of supersymmetry), e.g. by using the *Minimal Supersymmetric Standard Model* [84] (see [86]

for a calculation of the Higgs mass in the light of this supersymmetric model), provided that the mass of the lightest supersymmetric particle lies in the ~ TeV range. This is within the range of today's particle accelerator energies which is problematic, since it means that the particle should have been discovered. Nonetheless, the present most favored dark matter candidate, emerging as the lightest supersymmetric particle from many models, is the *neutralino*, which is a mixture of several supersymmetric particles. The lightest supersymmetric particle is usually stable and electrically neutral and is expected to interact with the standard model particles only gravitationally and through the weak force, which is just what we require from a dark matter candidate.

Weakly Interacting Massive Particles (WIMPs) is an generalization of dark matter candidates that interacts very weakly with the standard model particles. The term originally arrives from supersymmetry, implying GeV-TeV particles. If the WIMP is assumed to be a thermal relic, an upper mass bound of ~ 340 TeV can be set, using partial wave-unitarity [87]. Attempts on finding a lower bound have been made (e.g. [88] [89]) which suggest that WIMPs must have masses above ~ GeV. However, this bound may be avoided if the WIMP is kept in thermal equilibrium with, for instance, a light mediator [90]. In this project we will look into the case of a thermally produced light WIMP, in the mass-range $0.01-100$ MeV, that is coupled to *a)* neutrinos, or *b)* photons and $e^{\pm}$-pairs (electromagnetically coupled).

3.2 Including light WIMPs in AlterBBN

The presence of a light WIMP may affect the production of the light elements, provided that it is light enough to contribute to the relativistic degrees of freedom at the time around BBN. A WIMP that annihilates after neutrino decoupling will leave its signature on N_{eff}, through an altered late-time ratio between the neutrino and photon temperatures. Annihilation prior to neutrino decoupling will heat the neutrinos and photons equally much, and will further be non-relativistic during BBN. WIMPs heavier than ~ 20 MeV will have this property, and their negligible impact on the expansion rate will leave the primordial abundances unaltered. The annihilation of a WIMP after the end of BBN will affect N_{eff} and the production of the light elements through its relativistic nature during BBN. However, the impact on the relic abundances is the same for a WIMP that annihilates around the end of BBN ($m_{\chi} \sim 0.01$ MeV) and a WIMP that annihilates much later. This means that for the purposes of its impact on the light element production, the relevant WIMP masses lies in the range $\sim 0.01-20$ MeV. To make sure that the whole relevant range is covered, I will do as Nollett & Steigman [48] [25] and include WIMP masses between 0.01 and 100 MeV.

The type of WIMP, its mass, and its coupling to the standard model particles are provided by the user through the *.ini*-file discussed in chapter 2.2.1. Quantum characteristics like spin, and the coupling to SM particles determines the type of particle (see e.g. [91] for a detailed analytic discussion of the generalizations of these characteristics). In this work we restrict our analysis to spin-0 and spin-1/2 particles, but keeping it general so that other categories of WIMPs can be easily added later. This restriction will cover the following candidates:

- **Real Scalars** are spin-0 bosons and self-conjugate, meaning they are their own anti-particles. This implies that the internal degrees of freedom of real scalars are $g_{\chi} = 1$.

- **Complex Scalars** are also spin-0 bosons, but not self-conjugate, leading to $g_{\chi} = 2$.

- **Majorana Fermions** have spin-1/2 and are self-conjugate, thus $g_{\chi} = 2$.

- **Dirac Fermions** are not self-conjugate. Being spin-1/2 fermions the Dirac fermions possess $g_{\chi} = 4$.

Those are the same candidates as the ones analyzed by Nollett & Steigman in [48] and [25], where the authors have assumed $\phi_\chi = 0$ throughout their work. In section 3.3.2 I will discuss the effects of including a non-zero chemical potential for the WIMPs, but before that I will adopt the assumption of $\phi_\chi = 0$.

Only a few changes to the code were necessary to include the effects of light WIMPs. The WIMP energy density ρ_χ contributes to the total density of the universe and thus have to be included in the Friedmann equation (1.6), which determines the expansion rate of the universe. Depending on the nature of the WIMP (fermion or boson), the energy density is given by the Fermi-Dirac or Bose-Einstein distribution in equation 1.16 [48], with mass m_χ and internal degrees of freedom g_χ. Similarly, equation 1.17 is used to find the WIMP pressure P_χ, needed to compute the entropy of the WIMP. The WIMP pressure and energy density integrals are approximated according to the method used for the electrons and positrons, using the seven first terms of the well-established and accurate Bessel function expansion (see chapter 2.1.1 and appendix C). We will allow for a non-zero chemical potential for the light WIMPs, so that the expressions for the energy density and pressure of particles that are not self-conjugate, like complex scalars and Dirac fermions thus becomes

$$\rho_\chi = Ag_\chi(m_\chi c^2)^4 \sum_{n=1}^{\infty} (-1)^{\beta(n+1)} \cosh(n\phi_\chi)M(nz_\chi) \tag{3.1}$$

$$\frac{P_\chi}{c^2} = Ag_\chi(m_\chi c^2)^4 \sum_{n=1}^{\infty} \frac{(-1)^{\beta(n+1)}}{nz_\chi} \cosh(n\phi_\chi)L(nz_\chi) \,, \tag{3.2}$$

where $\beta = 0$ for bosons and 1 for fermions, $z_\chi = m_\chi c^2/k_B T_9$, where T_9 is the photon/neutrino temperature if the WIMPs are electromagnetically/neutrino coupled, and $A = 11753.913$ for $m_\chi c^2$ given in MeV to have the two expressions presented in units of $g\,cm^{-3}$. In the case that the particle is self-conjugate, like real scalars and Majorana fermions, the hyperbolic cosine factor $\cosh(n\phi_\chi)$ must be replaced with an exponential factor $e^{n\phi_\chi}$. For WIMPs like complex scalars and Dirac fermions we must count both particles and anti-particles, which have chemical potentials with opposite signs, leading to the hyperbolic cosine and an extra factor of 2, which is baked into the definition of g_χ. Self-conjugate WIMPs, on the other hand, are their own anti-particles, and we have only one contribution to the total energy density and pressure.

One of the effects of the additional entropy carried by the WIMPs comes in through equation 2.6. We see that it will depend not only on $\rho_\chi + P_\chi$, but also on the derivative of the WIMP energy density with respect to the temperature. The derivation of $d\rho_\chi/dT_9$ is found in appendix C, and is given by

$$\frac{d\rho_\chi}{dT_9} = Ag_\chi(m_\chi c^2)^4 \frac{1}{T_9} \sum_{n=1}^{\infty} (-1)^{\beta(n+1)} n \left[z_\chi \cosh(n\phi_\chi)N(nz_\chi) - \phi_\chi \sinh(n\phi_\chi)M(nz_\chi) \right] \,, \tag{3.3}$$

where we again must replace both the hyperbolic sine and cosine with an exponential for self-conjugate WIMPs. The other effect comes in through the conversion from the late-time to the initial value of η, needed to compute the initial value of h_η. Adding $s_\chi(T_i)$ to the total initial entropy density, equation 2.4 is therefore modified to (see equation 1.36)

$$h_{\eta,i} \approx 33685.519 \cdot \eta_0 \left(1 + \frac{s_{e^\pm}(T_i) + s_\chi(T_i)}{s_\gamma(T_i)} \right) \,. \tag{3.4}$$

In the presence of a light WIMP we must account for an increased expansion rate, influencing the cosmic time elapsed before we start our iteration. As mentioned in chapter 2.2.2 this was not considered in the original code, despite the fact that it comes with the option of including extra relativistic degrees of freedom in the form of an unspecified dark density. This has been taken care of in the new version by including correction factors for both WIMPs and extra, unspecified dark density.

In chapter 1.1 we encountered the effective number of neutrinos N_{eff} and we saw that equivalent

neutrinos outside the standard model gives a contribution ΔN_ν. Now we will allow for a possible non-neutrino contribution to N_{eff} in the form of light WIMPs. It is convenient to define N_{eff} through the late time $(T_\gamma \rightarrow T_{\gamma 0} \ll m_e)$ radiation energy density, normalized to the energy density in photons alone [48] (see definition 1.43):

$$\left(\frac{\rho'_R}{\rho_\gamma}\right)_0 = 1 + \frac{7}{8}\left[3\left(\frac{T_\nu}{T_\gamma}\right)_0^4 + \Delta N_\nu \left(\frac{T_\zeta}{T_\gamma}\right)_0^4\right] = 1 + \frac{7}{8}\left(\frac{T_\nu}{T_\gamma}\right)_0^4 [3 + \Delta N_\nu^*] \ . \tag{3.5}$$

Note that in chapter 1.1 we assumed equivalent neutrinos that decouple at the same time as the standard model neutrinos. Here we have opened up for the possibility that this may not be the case by introducing $\Delta N_\nu^* \equiv \Delta N_\nu (T_\zeta/T_\nu)_0^4 \leq \Delta N_\nu$, where the equivalent neutrino(s) may have a different temperature than the standard model neutrinos. For sterile neutrinos that decouples with the standard model neutrinos ΔN_ν^* will have integer values (1 for each sterile neutrino), while for bosons that decouple with the standard model neutrinos it will be an integer multiple of 4/7. In general however, in the case that $T_\zeta \neq T_\nu$, ΔN_ν^* need not be an integer or integer multiple of 4/7. For the sake of simplicity we will drop the asterisk when discussing equivalent neutrinos, so that $\Delta N_\nu^* \rightarrow \Delta N_\nu$. Note that the program does not compute ΔN_ν^* from an inputed ΔN_ν. Rather, the value given as an input by the user of the program is in fact ΔN_ν^*. The effect of $T_\zeta \neq T_\nu$ must therefore be computed beforehand.

We now assume instantaneous decoupling of the standard model neutrinos and extremely relativistic electrons/positrons, but later we will relax the latter assumption. We define N_{eff} through

$$\left(\frac{\rho'_R}{\rho_\gamma}\right)_0 \equiv 1 + \frac{7}{8}\left(\frac{4}{11}\right)^{4/3} N_{\text{eff}} \ . \tag{3.6}$$

Equating the two expressions for $(\rho'_R/\rho_\gamma)_0$ we find that

$$N_{\text{eff}} = 3\left[\frac{11}{4}\left(\frac{T_\nu}{T_\gamma}\right)_0^3\right]^{4/3}\left[1 + \frac{\Delta N_\nu^*}{3}\right] \equiv N_{\text{eff}}^0 \left[1 + \frac{\Delta N_\nu^*}{3}\right] \ . \tag{3.7}$$

In the SBBN scenario with no equivalent neutrinos we have $N_{\text{eff}} = N_{\text{eff}}^0$. Relaxing the assumption of extremely relativistic electrons/positrons yields $N_{\text{eff}}^0 = 3.018$ [23], and further relaxing the assumption of instantaneous decoupling of the standard neutrinos results in an increase to 3.046 (see discussion of equation 1.40). However, the latter is true only if we disregard equivalent neutrinos or light WIMPs, and in general N_{eff}^0 will be a function of the WIMP mass (and its nature and coupling to the standard model particles), thus $N_{\text{eff}} = N_{\text{eff}}(m_\chi, \Delta N_\nu)$. As argued by Nollett & Steigman in [25], there are no published detailed calculation of the neutrino phase space distribution that allows for equivalent neutrinos or light WIMPs, and that we therefore do not know the effect it may have on N_{eff}, but it is assumed to be negligible. For this reason we keep the assumption of instantaneous decoupling of the standard model neutrinos whenever we look at light WIMPs or equivalent neutrinos. On the other hand, in the standard scenario this effect is well documented [92], and whenever there are no WIMPs included we will use a value of 3.046 for N_{eff}.

In the presence of a light WIMP χ, N_{eff} depends on the nature of the WIMP (fermion or boson), its coupling to the standard model particles and its mass m_χ. Similar to the works of Nollett & Steigman [48] [25], I will in the following consider light WIMPs that annihilate to photons and electrons/positrons (electromagnetically coupled) or standard model neutrinos (neutrino coupled). As argued in chapter 2.3 I will assume that the neutrinos decouple instantaneously at 2.3 MeV, corresponding to a photon temperature of $T_9 \approx 27$, which is chosen as the initial temperature in the *AlterBBN* analysis.

3.2.1 Electromagnetically coupled light WIMPs

In this scenario we assume that the light WIMPs couple to photons and $e^\pm$-pairs. Right after neutrino decoupling the contributors to the total entropy content are photons, $e^\pm$-pairs and the light WIMPs. At

late-times (but before the end of radiation domination), after the $e^\pm$-pairs have annihilated and the light WIMPs have become non-relativistic, the only contributors are the photons. By entropy conservation (equation 1.30) we know that

$$a_d^3 s_{\text{tot}}(T_{\nu d}) = a_0^3 s_{\text{tot}}(T_{\gamma 0}) , \tag{3.8}$$

where $T_{\gamma 0}$ and a_0 are the late-time temperature and scale factor respectively, and a_d is the scale factor at the time of neutrino decoupling. Since the standard model neutrinos decouple at $T_{\nu d}$, their late-time temperature is given solely in terms of the universal expansion (redshifted according to $T_\nu \propto a^{-1}$). This means that $a_d T_{\nu d} = a_0 T_{\nu 0}$, and we can write

$$\left(\frac{T_{\nu 0}}{T_{\nu d}}\right)^3 = \frac{s_\gamma(T_{\gamma 0})}{s_\gamma(T_{\nu d}) + s_{e^\pm}(T_{\nu d}) + s_\chi(T_{\nu d})} = \frac{T_{\gamma 0}^3 / T_{\nu d}^3}{1 + \frac{s_{e^\pm}(T_{\nu d})}{s_\gamma(T_{\nu d})} + \frac{s_\chi(T_{\nu d})}{s_\gamma(T_{\nu d})}} . \tag{3.9}$$

Using the expression for relativistic entropy (equation 1.28), we can relate the entropy density between photons ($g_\gamma = 2$) and relativistic $e^\pm$-pairs ($g_{e^\pm} = 4$), and between photons and light WIMPs, finding that

$$\frac{s_{e^\pm}^{\text{rel}}(T_{\nu d})}{s_\gamma(T_{\nu d})} = \frac{7}{4} \qquad \text{and} \qquad \frac{s_\chi^{\text{rel}}(T_{\nu d})}{s_\gamma(T_{\nu d})} = \frac{\alpha g_\chi}{2} . \tag{3.10}$$

The factor αg_χ is given by equation 1.29, thus $\alpha = 1$ for bosons and 7/8 for fermions. Note that the entropy density of each particle specie going in to the equations above is the total entropy density of the specie, so it is essential to count both particles and anti-particles. For the light WIMPs, this is implicit in the definition of g_χ. We then use the definition $\phi_{\chi d} \equiv s_\chi(T_{\nu d})/s_\chi^{\text{rel}}(T_{\nu d})$, and the equivalent for electrons/positrons, ϕ_{ed}, which means that we normalize the entropy density of the particle specie to the entropy density it would have if it was to be ultra-relativistic. Thus we can write equation 3.9 as

$$\left(\frac{T_\nu}{T_\gamma}\right)_0^3 = \frac{2}{2 + \frac{7}{2}\phi_{ed} + \tilde{g}_\chi \phi_{\chi d}} , \tag{3.11}$$

where we have defined $\tilde{g}_\chi \equiv \alpha g_{\chi^\pm}$, which in our four cases becomes $\tilde{g}_\chi = (1, 2, 7/4, 7/2)$ for (real, complex, Majorana, Dirac). At $T_{\nu d} = 2 \, MeV$ we have $\phi_{ed} = 0.993$ [23], thus we can finally write

$$N_{\text{eff}}^0 = 3 \left[\frac{11}{4}\left(\frac{T_\nu}{T_\gamma}\right)_0^3\right]^{4/3} = 3 \left[\frac{11}{10.95 + 2\tilde{g}_\chi \phi_{\chi d}}\right]^{4/3} . \tag{3.12}$$

Setting $\phi_{\chi d} = 0$, which means no lights WIMPs are included, we notice that we retain our SBBN value of $N_{\text{eff}}^0 = 3.018$.

We observe that N_{eff}^0 is effectively a function of the WIMP mass, m_χ, since $\phi_{\chi d}$ is a function of $s_\chi(T_{\nu d})$, which again is a function of $\rho_\chi(m_\chi)$ and $P_\chi(m_\chi)$. In figure 3.1, $N_{\text{eff}}^0(m_\chi)$ is plotted for WIMP masses in the range 0.1 to 100 MeV for both electromagnetically (EM) and neutrino coupled WIMPs, while in figure 3.2 $N_{\text{eff}}(m_\chi)$ is plotted in the same mass range for a Majorana fermion only and with three different values of ΔN_ν. The horizontal gray strips are the 1σ and 2σ confidence limits from the CMB respectively (see table 1.1). For the EM coupled WIMPs we notice a lower limit on the WIMP mass for $\Delta N_\nu = 0$ at $\sim 5 - 10$ MeV, depending on the nature of the WIMP. Allowing for equivalent neutrinos we see that this lower limit is shifted towards lower WIMP masses but imposes an upper limit if we add enough equivalent neutrinos. For the case of neutrino coupled WIMPs we see that the lower limits on the WIMP mass is ~ 2 MeV lower than in the EM coupled WIMP scenario, and that in this case the combination with equivalent neutrinos is less favored than in the EM coupled case. I refer to the Nollett & Steigman papers [48] and [25] for a more extensive discussion of these plots.

3.2.2 Neutrino coupled light WIMPs

For WIMPs that annihilate to neutrinos there are two possibilities: 1) The WIMP may heat the standard model neutrinos but not any equivalent neutrinos or 2) it may heat both. The usual assumption is that the

equivalent neutrinos are very weakly coupled to the standard model neutrinos and thereby the neutrino coupled WIMPs. This is likely the situation in the case of sterile neutrinos, which by definition do not take part in the weak interactions. The difference between the two cases is so small anyway, that e.g. in the case of $0 \leq \Delta N_\nu \leq 1$ it is invisible on the scale of figure 3.2 [25], and we see from this figure that larger values of ΔN_ν are disfavored. In this work I will make the same assumption, so unless stated otherwise, whenever I talk about neutrino coupled WIMPs I refer to the case where the WIMPs are coupled only to the standard model neutrinos. However, the nature of hidden neutrino species, if they exist, are by definition not known. Therefore it would not make much sense just to include the case of WIMPs that couple solely to the standard model neutrinos. Both cases are thus implemented in *AlterBBN*, and discussed in this section.

We start with the situation that the WIMPs heat only the standard model neutrinos. The annihilation of the WIMPs will affect the late-time T_ν/T_γ-ratio (neutrinos are heated relative to the photons). In this case the neutrino temperature post decoupling is not simply given by $T_\nu \propto a^{-1}$ anymore. Instead we need to look at the individual entropy conservation for WIMPs+neutrinos ($s_{\nu\chi}$) and photons+$e^\pm$ ($s_{\gamma e^\pm}$). The procedure of finding N_{eff} based on entropy conversion was given in the discussion of the electromagnetically coupled WIMPs. Here, we just state the results, which for WIMPs that only couple to standard model neutrinos is [25] [23]

$$N_{\text{eff}}^0 = 3 \left[\frac{11}{4} \left(\frac{T_\nu}{T_\gamma} \right)_0^3 \right]^{4/3} = 3.018 \left[1 + \frac{4\tilde{g}_\chi \phi_{\chi d}}{21} \right]^{4/3} . \qquad (3.13)$$

Note that in this case $N_{\text{eff}} = N_{\text{eff}}^0 + 3.018(1 + \Delta N_\nu/3)$, contrary to the case of electromagnetically coupled WIMPs, where $N_{\text{eff}} = N_{\text{eff}}^0(1 + \Delta N_\nu/3)$. In the case of WIMPs that heat both the standard model and equivalent neutrinos the expression becomes [25]:

$$N_{\text{eff}}^0 = 3.018 \left[1 + \frac{4\tilde{g}_\chi \phi_{\chi d}}{21 + 7\Delta N_\nu} \right]^{4/3} . \qquad (3.14)$$

Here $N_{\text{eff}} = N_{\text{eff}}^0(1 + \Delta N_\nu/3)$, like in the case of electromagnetically coupled WIMPs.

Since the entropy of the light WIMPs is transferred to the neutrinos during their annihilation process, the task of computing the neutrino temperature becomes a bit more involved. In the case that the WIMPs annihilate only to the standard model neutrinos, the temperature of the equivalent neutrinos are found by their scaling with the baryon density, just as before, and given by equation 2.15. The shared neutrino and WIMP temperature, on the other hand, is promoted to a dynamic variable, just as the photon temperature. This means that equation 2.6 is now split into two separate quantities, dr/dT_9 and $dr/dT_{\nu 9}$, which are individually time-evolved. The former now only includes the photons, $e^\pm$-pairs and the baryons, while the WIMPs are incorporated in the latter, together with the neutrinos. The quantity $dr/dT_{\nu 9}$ requires that we know the derivative of the neutrino energy density with respect to the neutrino temperature. This have been implemented as an individual function in the module *omega.c*, alongside the function for calculating the neutrino energy density. With the separation of the neutrino and equivalent neutrino temperatures, these functions becomes dependent on both temperatures.

3.3 Results

We will now discuss the effects from including light WIMPs, first by comparing a selection of plots with the ones found in the Nollett & Steigman papers concerning electromagnetically coupled [48] and neutrino coupled [25] WIMPs, assuming a zero chemical potential. Then we will go a step further and analyze the effects that a non-zero chemical may have on the relic abundances.
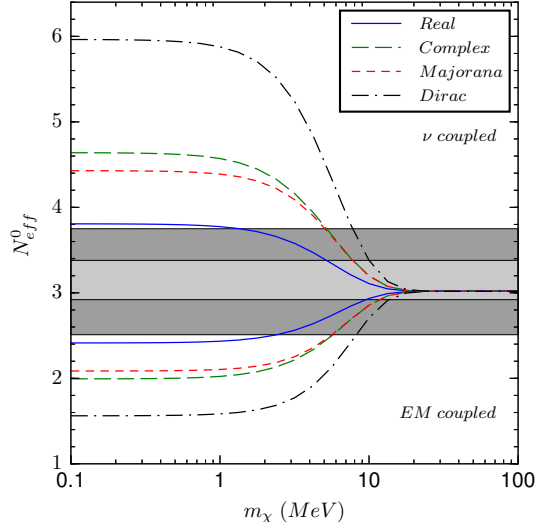
Figure 3.1: N^0_{eff}, the value of N_{eff} for $\Delta N_\nu = 0$, as a function of the WIMP mass for WIMPs that annihilate to photons and $e^\pm$ pairs (lower set of curves) and those that annihilate to the SM neutrinos (upper set of curves). Four different types of WIMPs have been analyzed, and they are real scalars (solid lines), complex scalars (long dashes), Majorana fermions (short dashes) and Dirac fermions (dash-dot). The horizontal bands are the 1σ (lighter gray) and 2σ (darker gray) ranges of the Planck CMB 2015 values [1] of N_{eff} (see table 1.1).
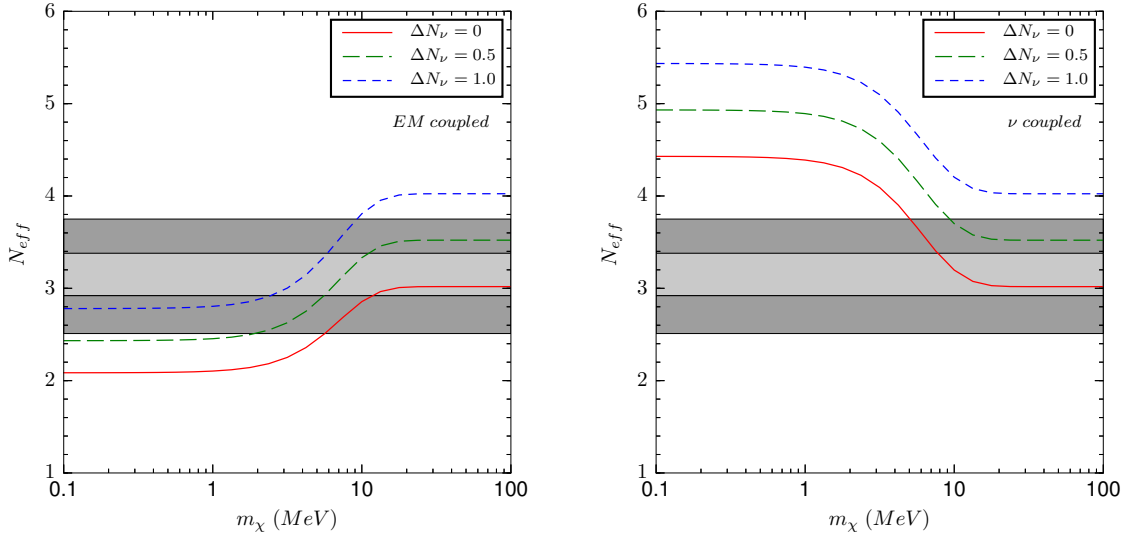

Figure 3.2: The two panels show N_{eff} as a function of the WIMP mass for an electromagnetically coupled Majorana WIMP (left panel) and a neutrino coupled Majorana WIMP (right panel), for $\Delta N_\nu = 0$ (solid), 0.5 (long dashed) and 1 (short dashed) equivalent neutrinos.

3.3.1 Assuming a Zero WIMP Chemical Potential

Since the release of the Nollett & Steigman papers there have been an update on the CMB measured value of $\Omega_b h^2$ and the recommended value of the mean neutron lifetime. The updated values (given in table 1.1), as well as the modified initial temperature for the iterations will impose differences between the results here and those found in the Nollett & Steigman papers. I have run *AlterBBN* with the same settings as these papers and found a very good agreement for all four elements. There are small differ-

ences, likely due to differing reaction rates[1] and the fact that the authors of the papers have implemented Coulomb, radiative and finite-nucleon-mass corrections to the weak rates. The latter will mainly affect the amount of neutrons available for BBN and thus the resulting ^4He abundance, while the former are prone to affect all element abundances. Going from the Nollett & Steigman adopted value of $\eta_{10}=6.026$ to the updated value of $\eta_{10}=6.10$ will not influence the ^4He abundance much, since this is only logarithmically dependent on the baryon-to-photon ratio. However, it will lower the deuterium yield by $\sim 2\%$ and also affect the resulting ^3He and ^7Li abundances. The new and higher value of the neutron lifetime (updated from 880.1 ± 1.1 to 880.3 ± 1.1) will lead to more available neutrons at BBN, resulting in a higher ^4He yield. However, the change is so small that is has a negligible effect on the results.

Comparing figures 3.1 and 3.2 with the corresponding figures found in the Nollett & Steigman paper discussing neutrino coupled WIMPs [25], we see that they are practically identical. This ensures us that the expressions for the WIMP energy density and pressure are implemented correctly (trusting that Nollett & Steigman are right!). The abundance predictions for different WIMP masses using the updated code may be seen in figures 3.3 (electromagnetically coupled) and 3.4 (neutrino coupled). It is here assumed that $\Delta N_\nu = 0$. For both electromagnetically and neutrino coupled WIMPs we see that in the presence of light WIMPs with masses $m_\chi \gtrsim 20$ MeV the abundance yields are unaltered relative to the SBBN scenario. Such high mass WIMPs annihilate before or in the earliest stages of neutrino decoupling and will not affect the late-time neutrino-to-photon temperature ratio, nor will their high mass contribute significantly to the radiation density during BBN.

WIMPs with masses in the range $m_e \lesssim m_\chi \lesssim 7$ MeV will annihilate after or at the end of neutrino decoupling but before BBN, thus leading to an altered late-time neutrino-to-photon temperature ratio compared to the case of SBBN. Electromagnetically coupled WIMPs reduce this ratio and lead to a slower expansion at fixed T_γ. This leaves more time for deuterium and ^3He destruction at the end of BBN, reducing their relic abundances, while one of the main end products of this destruction process, ^7Li, naturally increases its abundance. A $m_\chi \gtrsim 2$ MeV WIMP will mostly have annihilated and become non-relativistic before the time of n/p weak freeze-out. Through the effect of a reduced neutrino-to-photon temperature ratio the expansion is slower compared to SBBN at fixed T_γ, but also the weak rates are slower, inhibiting proton conversion to neutrons even before n/p freeze-out. The weak rates depend on the neutrino temperature, and colder neutrinos will slow down the rates. However, they do not slow $n \to p$ and $p \to n$ conversion rates equally [48]. Colder neutrinos actually suppress proton destruction more than they suppress neutron destruction, leading to less neutrons present than in the case of a higher neutrino temperature. These effects nearly cancels, but we see that there is a somewhat lower relic abundance of ^4He for WIMP masses in the range $2 \lesssim m_\chi \lesssim 20$ MeV due to less available neutrons at BBN. For even lower WIMP masses the direct effect on the relativistic density results in an increased expansion rate compared to SBBN at fixed T_γ, reducing the time available for neutron decay. This increase in neutrons available at BBN leads to an increase in the resulting abundance of ^4He. If the WIMP annihilates after BBN has ended it will affect BBN only through its direct contribution to the relativistic energy, increasing the expansion rate. This will tend to raise the abundances of deuterium and ^3He, while decreasing the ^7Li yield. However, since such WIMPs have not yet annihilated, the value of η will be lower than in the SBBN case, or in the case that the WIMPs annihilate before BBN has ended. This will have the effect of lowering the abundances of deuterium and ^3He, while increasing the ^7Li abundance. We see from figure 3.3 that this is the leading effect for WIMP masses $m_\chi \lesssim 0.1$ MeV.

In the case of neutrino coupled WIMPs the effect on the ^4He yield is that any WIMP mass (below the limit of ~ 20 MeV) will drive the abundance up compared to the case of SBBN (no WIMP). Since the WIMPs annihilate to neutrinos the neutrino-to-photon temperature ratio will increase, in contrast to electromagnetically coupled WIMPs. This will speed up the weak rates in addition to contributing directly to the relativistic energy density. For electromagnetically coupled WIMPs the effect on the weak rates and the energy density nearly canceled, but here they will add up. The increased expansion rate relative to SBBN, for fixed T_γ, during BBN will leave less time for deuterium and ^3He destruction,

---

[1] I do not know what reaction rates Nollett & Steigman uses, and how large their nuclear network is, but their papers was publish before some of the reaction rates updated here was made available, so there must be at least a few differences.
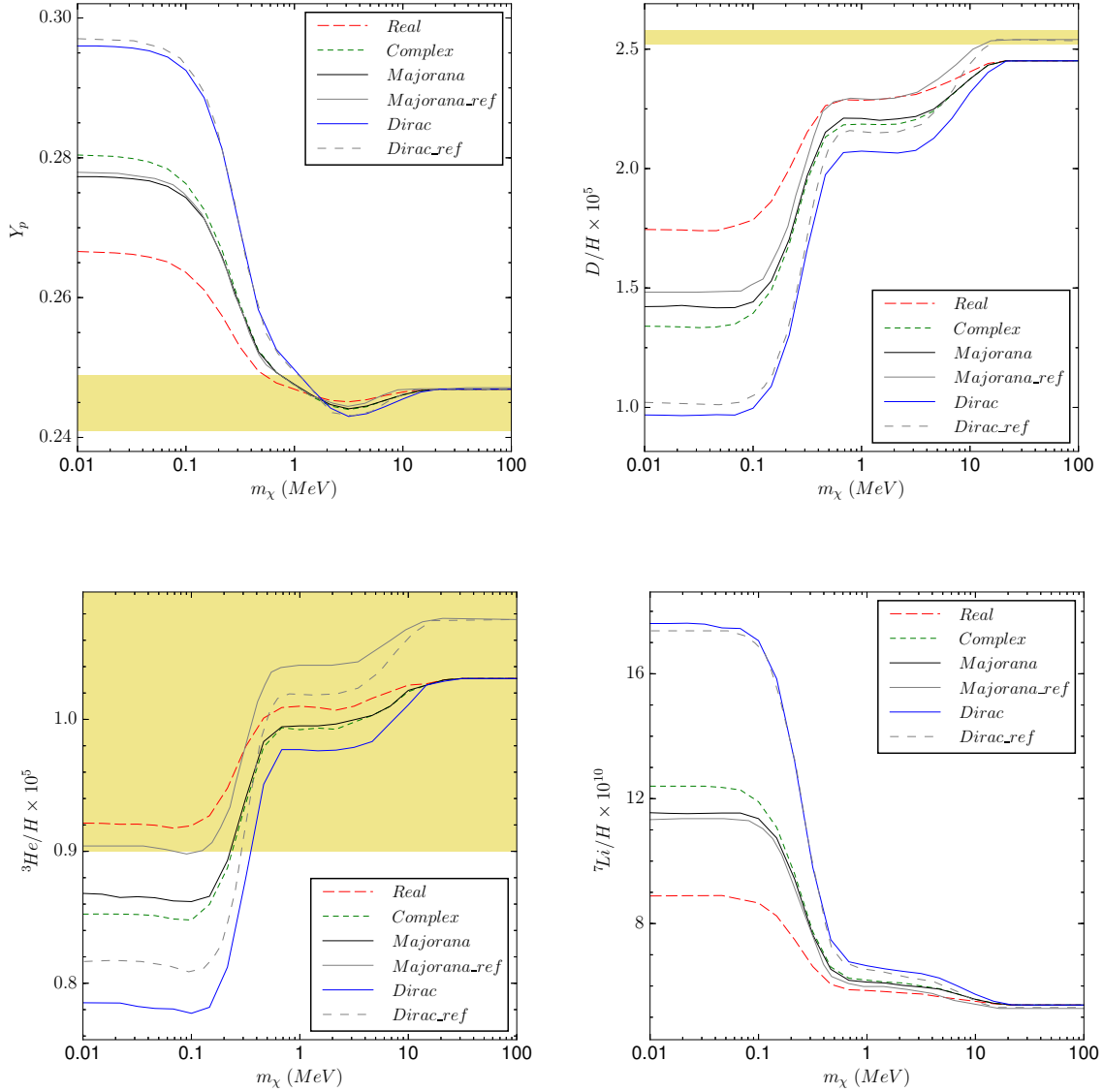
Figure 3.3: Resulting abundances of ^4He and D as a function of WIMP mass for electromagnetically coupled WIMPs. The gray solid and gray dashed lines show the Nollett & Steigman results for Majorana and Dirac respectively. The colored lines shows the results from an AlterBBN run with $\eta_{10} = 6.026$, $N_{\text{eff}} = 3.018$, $\tau_n = 880.1$ and no equivalent neutrinos. For the D and ^3He abundances the ordering for $m_\chi \to 0$ is, from bottom to top: Dirac, complex, Majorana, real. For ^4He and ^7Li the order is switched. The colored horizontal bands show the observational limits discussed in chapter 1.2. Note that the observational limit on ^7Li is $1.6 \pm 0.3 \cdot 10^{-10}$, being outside the plotting range.

leading to higher relic abundances of these two elements. Since ^7Be is still being produced at the end of BBN, a faster expansion will lead to a decrease in its abundance and, conversely, a decrease in the ^7Li abundance. WIMPs that annihilate after BBN will have a reduced effect on the resulting abundances. If the WIMPs are still present at the end of BBN the effect is a decrease of the speed-up effect, since if they had already annihilated, the expansion would be faster. This means that the yield curves for $m_\chi \to 0$ tend towards their value for $m_\chi \to \infty$.

We note that in the case that the WIMP is electromagnetically coupled the ^7Li yield will increase for all WIMP types and masses, compared to the SBBN scenario. Since the opposite is true for neutrino coupled WIMPs, the gap between the observed and predicted primordial abundance of the element is reduced. The effect is biggest for a $0.2 \lesssim m_\chi \lesssim 4$ MeV Dirac WIMP, in which case the ^7Li yield is reduced by $\sim 25\%$. However, this is still 2.5 times the observed value, thus BBN in the presence of a
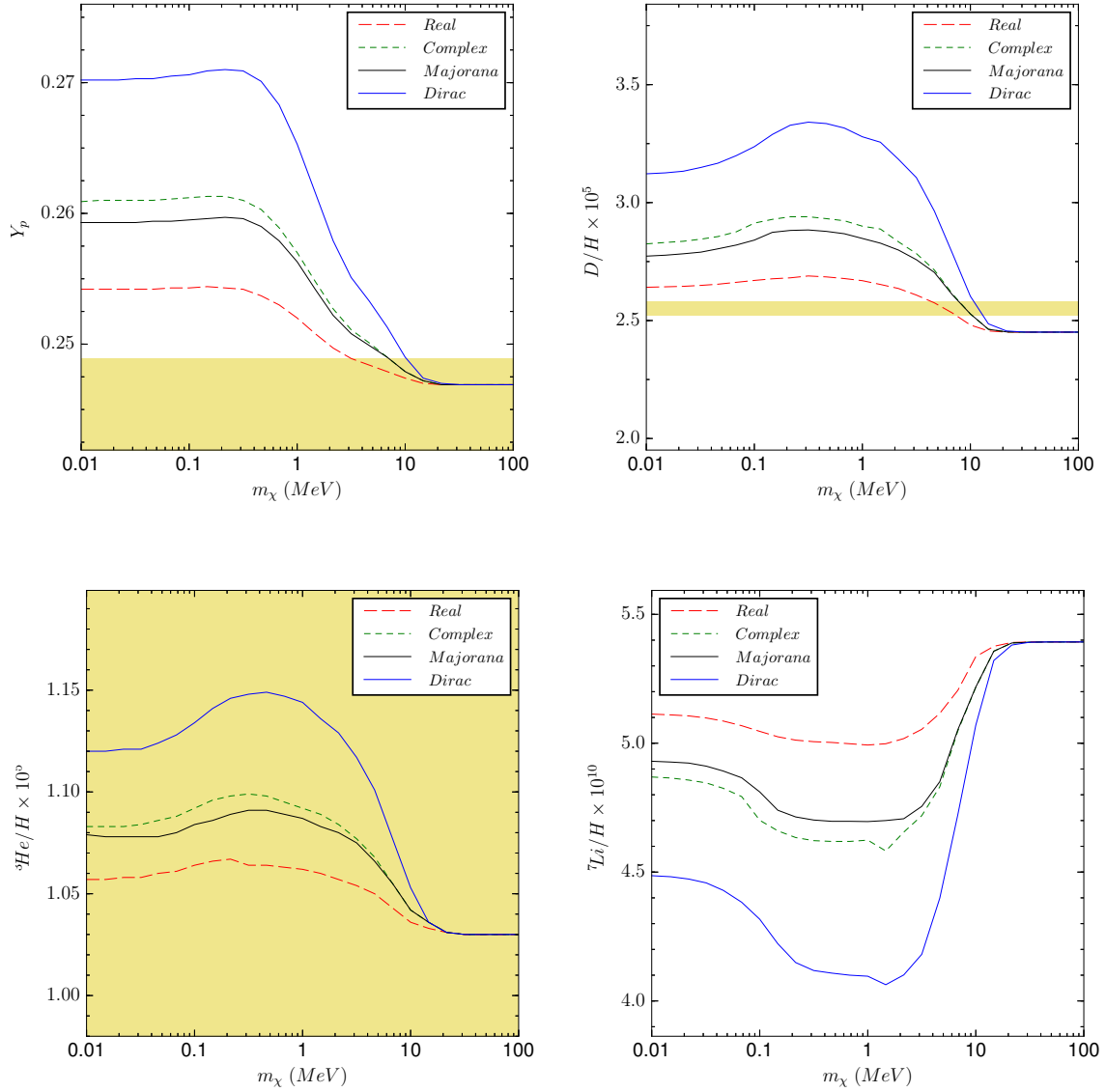
Figure 3.4: Resulting abundances of ^4He and D as a function of WIMP mass for neutrino coupled WIMPs. The colored lines shows the results from an AlterBBN run with $\eta_{10} = 6.026$, $N_{\text{eff}} = 3.018$, $\tau_n = 880.1$, and no equivalent neutrinos. For the ^4He, D and ^3He abundances the ordering for $m_\chi \to 0$ is, from top to bottom: Dirac, complex, Majorana, real. For ^7Li the order is switched. The colored horizontal bands show the observational limits discussed in chapter 1.2. Note that the observational limit on ^7Li is $1.6 \pm 0.3 \cdot 10^{-10}$, being outside the plotting range.

light WIMP does not seem to be able to fix the lithium problem.

The effect that a light WIMP has on the expansion rate is fully understood from figure 3.5, where the time elapsed since the big bang singularity is plotted against the photon temperature for electromagnetically coupled (left panel) and neutrino coupled (right panel) Majorana WIMPs with different masses. This is very nearly the same as plotting the inverse of the expansion rate. The time is normalized to the time elapsed in the SBBN scenario (no WIMP), thus a ratio of unity indicates the same evolution as in SBBN. Similarly, a ratio greater or lower than unity indicates a slower or faster evolution respectively. Here we have assumed $\Delta N_\nu = 0$ as well. We see that a light WIMP will contribute directly to the expansion rate while it is still relativistic, and that this leads to a faster evolution than in the SBBN case. After the WIMP has annihilated to photons and $e^\pm$-pairs (left panel), the ratio of the neutrino-to-photon temperature decreases, which leads to a slower evolution than in the SBBN scenario. We see that as the
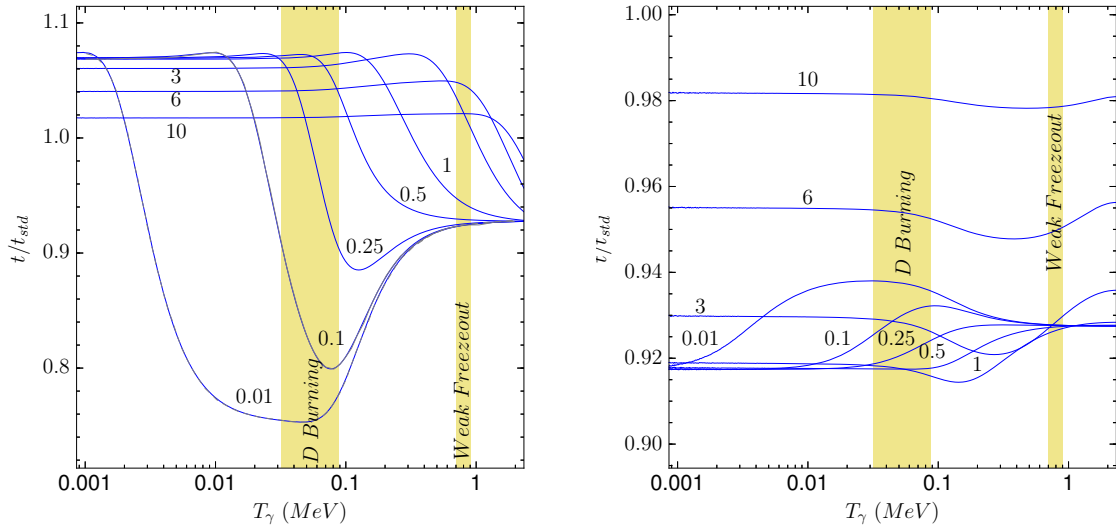
Figure 3.5: Time elapsed since the Big Bang singularity for electromagnetically coupled (left panel) and neutrino coupled (right panel) Majorana WIMPs with with masses between 0.01–10 MeV, normalized to the time elapsed in the SBBN scenario, for the photon temperatures relevant for BBN. We have here set $\Delta N_\nu = 0$. The colored vertical bands correspond to the approximate temperature intervals for deuterium burning and weak n/p freeze-out respectively. A time ratio higher than unity indicates a slower expansion than in the SBBN scenario, while the opposite is true for a lower ratio.

WIMP mass increases, its effect on the time evolution becomes smaller and smaller. A WIMP heavier than ~ 20 MeV will mostly annihilate before neutrino decoupling, not affecting the neutrino-to-photon temperature at late times. Although there is still a small effect from the contribution to the total relativistic energy density for WIMPs with masses around 20 MeV, this effect is diluted for even heavier WIMPs because of their non-relativistic nature at the times of interest. The results of Nollett & Steigman for electromagnetically coupled WIMPs with masses $m_\chi = 0.01$ and 0.1 are shown as gray solid and dashed lines respectively. They are hard to distinguish from the *AlterBBN* results, so we may conclude that the agreement is good.

In the case that the WIMPs are coupled to the neutrinos the expansion will always be faster than in the SBBN scenario, since they will increase the neutrino-to-photon temperature ratio by annihilation, as well as contribute directly to an increased energy density. If the WIMPs annihilate after BBN the effect on the expansion rate through an increased neutrino-to-photon temperature ratio is delayed and the expansion is slower compared to the slightly heavier WIMPs that annihilate before or during BBN.

The results of including light WIMPs are well summarized by combining figures 3.1 and 3.2 with figure 3.6. The latter shows the joint ^4He vs D yields plotted for a Majorana WIMP with masses between 0.01 and 100 MeV, and for three different values of ΔN_ν (0, 0.5 and 1). The blue solid line shows the yields in the $m_\chi \to \infty$ limit, and the left side of this line corresponds to electromagnetically coupled WIMPs, with masses decreasing towards the upper left corner. The continuation of the yield lines over to the right side of the blue solid line marks the $m_\chi \to \infty$ limit for neutrino coupled WIMPs, with masses decreasing towards the $m_\chi \to 0$ limit as they again touch the blue line. Also shown are the yields for electromagnetically coupled WIMPs with the same mass as the electron, as well as joint 1σ and 2σ joint confidence intervals for the observed ^4He and deuterium abundances. The combined confidence intervals are found by finding the points (x,y) that satisfies

$$\left(\frac{x}{\sigma_x}\right)^2 + \left(\frac{y}{\sigma_y}\right)^2 = s \,, \tag{3.15}$$

where s is given by the confidence level. Looking up tables of χ^2 distribution we find that for 2 degrees
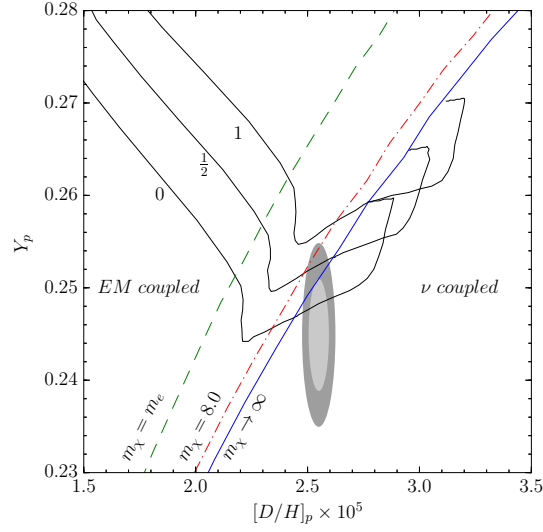
Figure 3.6: The joint Y_P and D yields for WIMP masses in the range 0.01 to 100 MeV, for $N_\nu = 0, 0.5$ and 1.0, assuming a Majorana fermion. Starting from $m_\chi \to 0$ in the top left corner we move along the yield lines for electromagnetically coupled WIMPs, until the $m_\chi \to \infty$ limit is reached as they touch the blue solid line. Continuing on the other side of that line, we move from the $m_\chi \to \infty$ limit for neutrino coupled WIMPs, until they again touch the blue solid line, at a higher value of Y_P, in the $m_\chi \to 0$ limit. Also included are the yields found by varying N_ν, setting the WIMP mass equal to the electron mass (green dashed line), and the best fit mass for an electromagnetically coupled WIMP ($m_\chi = 8$ MeV) found by Nollett & Steigman (red dashed-dotted line). The shaded gray ellipses correspond to the joint Y_P and D observed confidence intervals (1σ and 2σ).

of freedom:

$$P(s < 6.18) = 1 - 0.317 = 0.683 \qquad (1\sigma) \qquad (3.16)$$

and

$$P(s < 2.296) = 1 - 0.045 = 0.955 \qquad (2\sigma) . \qquad (3.17)$$

Thus the width and height of the ellipse is $2\sigma_x \sqrt{s}$ and $2\sigma_y \sqrt{s}$ respectively, where $s = 6.18$ for 1σ and $s = 2.296$ for 2σ. For σ_x and σ_y I have used the uncertainty in the observed deuterium (0.03) and ^4He (0.004) abundances respectively (see chapter 1.2).

The figure is to be compared with figure 13 in the paper of Nollett & Steigman concerning neutrino coupled WIMPs [25]. The yield lines are shifted a bit to the left compared to their work because of the higher value of η used to produce figure 3.6, as well as the effect from updating the reaction rates. Another important difference from their work is the updated observational constraints on D and ^4He, and in particular the constraint on ^4He, which is significantly lower compared to their work.

Summing up the conclusions from their work, they find that an electromagnetically coupled light WIMP slightly favors $m_\chi \sim 8$ MeV for a Majorana type WIMP (also marked in figure 3.6, with a red dashed line), with small variations depending on the type of WIMP. However, the $m_\chi \to \infty$ limit, equivalent to no light WIMP, still remains a good fit. A sufficiently light WIMP ($m_\chi \approx 5$–10 MeV) that is electromagnetically coupled favors $\Delta N_\nu > 0$ and allows one fermionic sterile neutrino ($\Delta N_\nu = 1$), but not two. Neutrino coupled WIMPs, on the other hand, allows $\Delta N_\nu = 0$, but disfavors $\Delta N_\nu \gtrsim 0.5$. Excluding unphysical, negative values of ΔN_ν the best fit for a neutrino coupled WIMP is $m_\chi \geq 35$ MeV, which is equivalent to no WIMP at all. Only in the case that the light WIMP is a real scalar, $m_\chi \ll m_e$ is not strongly ruled out.

We see that the updated results have significantly altered the best fits in the Nollett & Steigman discussion. They now favor much smaller WIMP masses, both in the electromagnetically and neutrino coupled case. This has made a neutrino coupled WIMP more prone to affect the primordial abundances, and an electromagnetically coupled WIMP in combination with $\Delta_\nu = 0$ is now even further disfavored. Monte-Carlo parameter estimations have not been conducted in this project, and is necessary for making any further conclusions regarding best fit WIMP masses and the connections to different values of ΔN_ν.
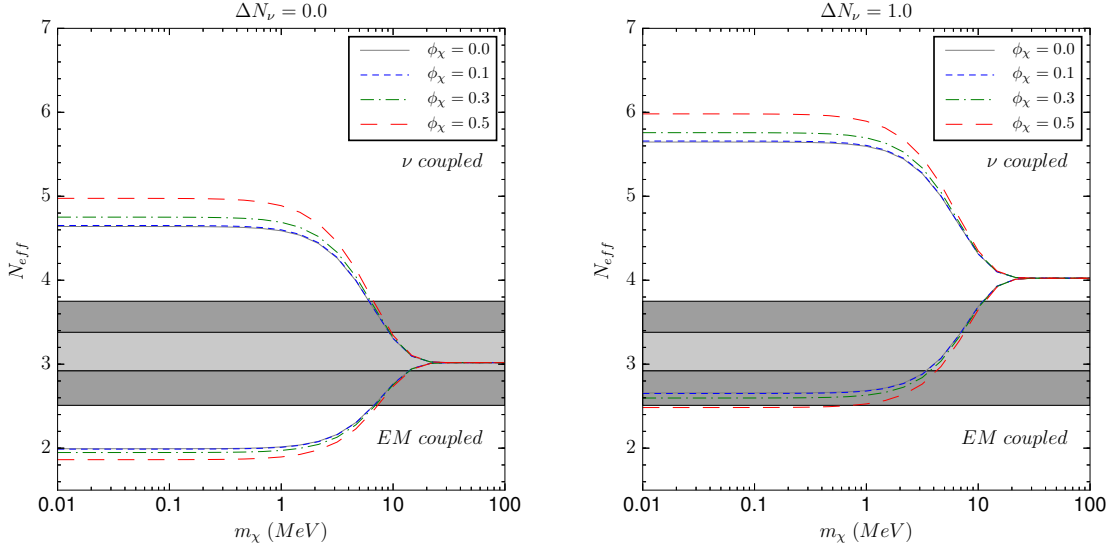
Figure 3.7: The effective number of neutrinos in the presence of a complex scalar with different values for a constant chemical potential. The left panel shows the results for $\Delta N_\nu = 0$, while in the right panel we have added one equivalent neutrino. The colored horizontal bands correspond to the observational 1σ and 2σ constraints on N_{eff}, where the values from table 1.1 have been used.

For now we note that the updated results seem to tend towards a better fit for neutrino coupled WIMPs, and in general a stronger disfavoring of $\Delta N_\nu > 1$.

The differences between a Majorana fermion and a complex scalar is too small to be noticeable on the scale of figure 3.6, as we might have expected from figures 3.1, 3.3 and 3.4. Since Majorana particles are self-conjugate I find it more interesting to consider complex scalars or Dirac fermions when we in the following will discuss the effects of including a non-zero chemical potential for the WIMPs.

3.3.2 Adding a WIMP Chemical Potential

The canonical textbook assumption of a negligible WIMP chemical potential is here investigated through the effect that a relaxation of this assumption may have on the production of the light elements during BBN, as well as its impact on the late-time ratio between the neutrino and photon temperature, quantified through N_{eff}. Dark matter candidates are generally assumed to possess zero charge, or else they would interact electromagnetically with photons today and be easier detectable. Thus, a non-zero chemical potential in the dark sector is not necessary linked to any asymmetry between particles and anti-particles (see chapter 1.1.5). For particles that are not self-conjugate however, a chemical potential may point to an asymmetry, contrary to self-conjugate particles which, from the property of being their own anti-particles, by definition can not have any asymmetry. For this reason the most interesting cases are that of a Dirac fermion and a complex scalar.

In chapter 2.1.1 we saw that we are able to derive two expressions for the total number density of electrons and positrons; one through their distribution function (equation 2.23), dependent on ϕ_e; and one through the assumption of universal charge conservation (equation 2.24), dependent on the baryon density. This enables us to time-evolve the electron degeneracy parameter, an evolution that in the case of SBBN is seen in figure 2.1. For dark matter however, we are unable to make such an assumption without prior knowledge of the annihilation cross-section of the dark matter particle. This might be interesting to look into in the future, by allowing for specific dark matter particles. Looking at at the left panel of figure 2.1 we see that the electron degeneracy parameter $\phi_e \equiv \mu_e/T$ is constant as long as the electrons
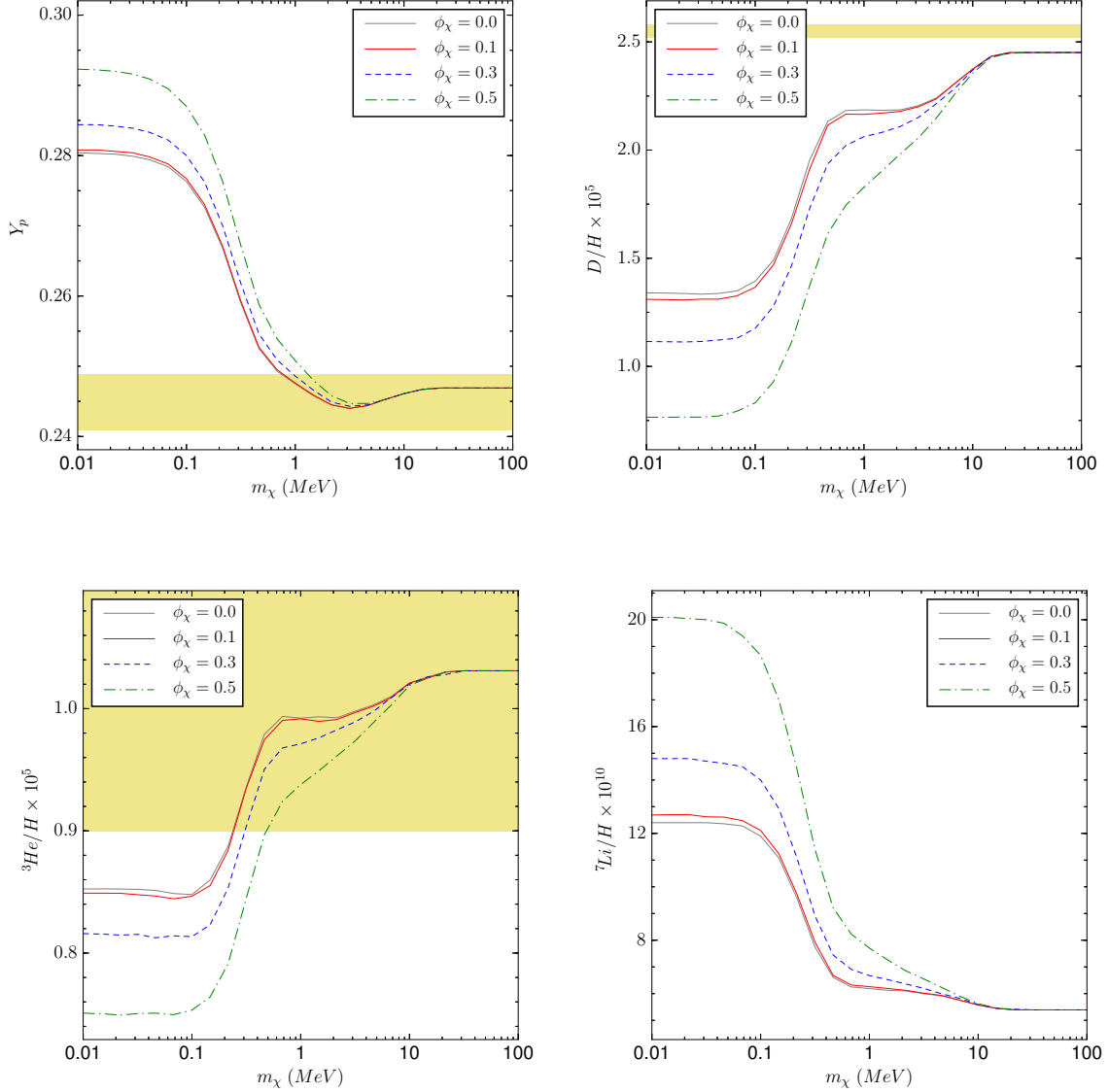
Figure 3.8: The resulting abundances in the presence of an electromagnetically coupled complex scalar with different values for a constant chemical potential, assuming $\Delta N_\nu = 0$. The colored horizontal bands correspond to the observational constraint on the abundances, as discussed in chapter 1.2.

are in thermal (and thus chemical) equilibrium with the rest of the plasma. However, as they start to become non-relativistic and annihilate, ϕ_e evolves quite drastically. After all the positrons are gone, the chemical potential loses its meaning since it is a result of the asymmetry in the electron/positron number densities. The constant value as the electrons have become fully non-relativistic is due to a numerical cut-off, preventing the equations 2.17 and 2.18 from suffering from overflow. If there is a WIMP chemical potential and this stems from an asymmetry in the particle/anti-particle number densities, there will be a similar evolution in the WIMP degeneracy parameter as the particles annihilate. However, allowing for a changing WIMP chemical potential was out of the scope of this project, so we restrict ourselves to constant values here.

We notice from figure 3.7 that a chemical potential will have the effect of increasing the effective number of neutrinos if the WIMP is neutrino coupled, resulting from the fact that the energy density of the WIMP increases compared to the case where its chemical potential is zero. Since the WIMP is
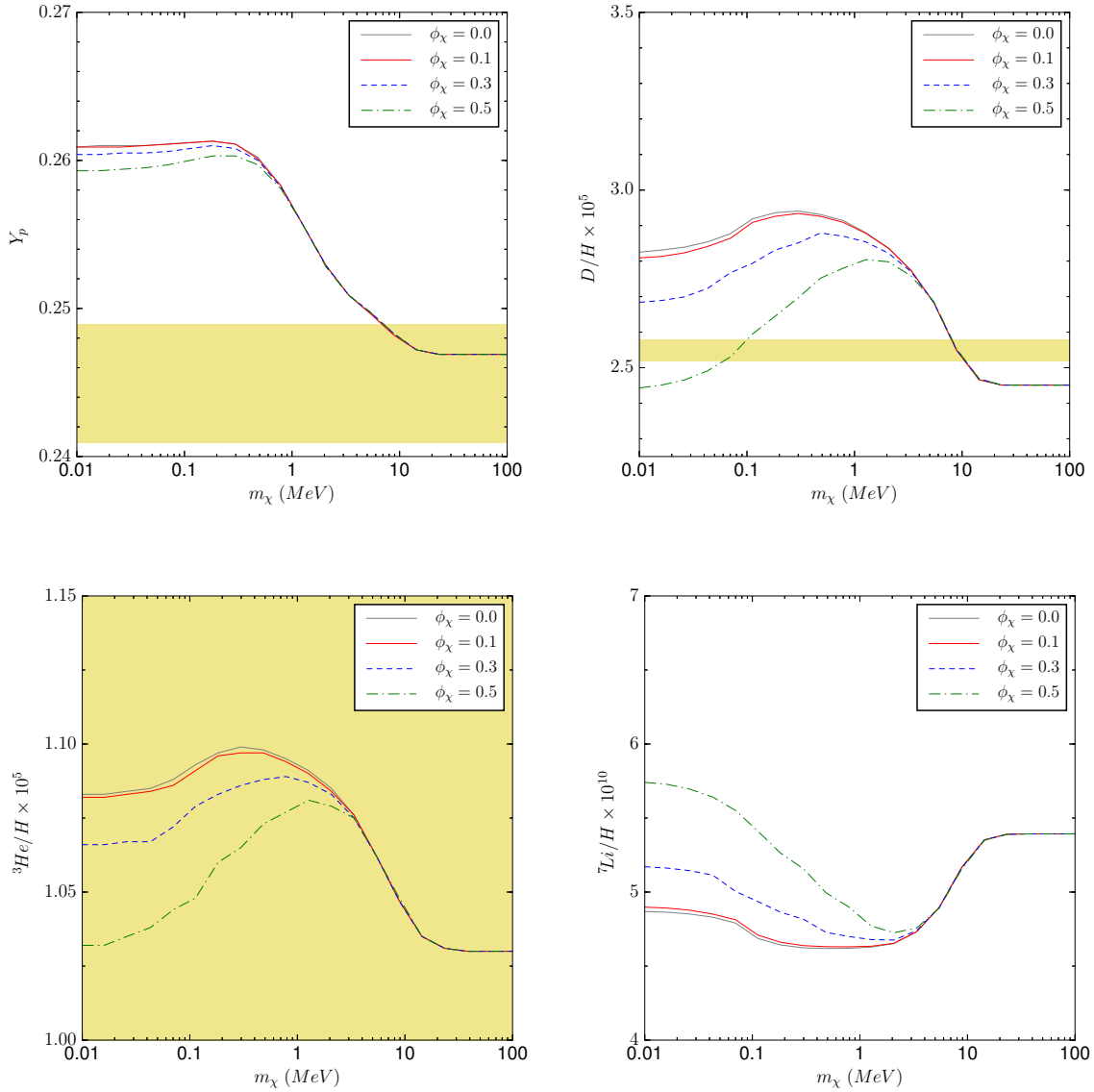
Figure 3.9: The resulting abundances in the presence of a neutrino coupled complex scalar with different values of a constant chemical potential, assuming $\Delta N_\nu = 0$. The colored horizontal bands correspond to the observational constraint on the abundances, as discussed in chapter 1.2.

coupled to the neutrinos but not the photons and $e^\pm$-pairs, the neutrino neutrino-to-photon temperature will be higher, leading to an increase in N_{eff}. For an electromagnetically coupled WIMP the effect is that the photon temperature will increase compared to that of the neutrinos and N_{eff} will consequently decrease.

No equivalent neutrinos

The effect on the resulting light element abundances of D, ^4He, ^3He and ^7Li, assuming $\Delta N_\nu = 0$, is illustrated in figures 3.8 (electromagnetically coupled) and 3.9 (neutrino coupled). For an electromagnetically coupled WIMP with a non-zero chemical potential the tendency is that for all WIMP masses that may affect the resulting abundances, the abundances are driven further away from their observational constraints than in the case of $\phi_\chi = 0$. We see that some masses are still allowed for relatively high chemical potentials when considering the ^4He and ^3He abundances alone. However, considering

the deuterium abundance, any positive value for the chemical potential is less favored than $\phi_\chi = 0$ for any WIMP mass. For a neutrino coupled WIMP we see that a chemical potential corresponding to $\phi_\chi \gtrsim 0.4$ is consistent with the observed deuterium abundance for a small range of WIMP masses, where the allowed mass-range increases with increasing ϕ_χ. Looking at the effect on the ^4He abundance however, we see that although an increasing chemical potential pushes its value towards the observational constraint for $m_\chi \lesssim 1$ MeV, the shift is not enough to make it compatible with the observations. It is however, interesting to see that with an increasing chemical potential, we are able to obtain a deuterium yield compatible with the observations for very light WIMPs ($m_\chi \lesssim 1$ MeV).

The observational constraint on the ^3He yield is so conservative that any of the values analyzed are within the bounds for a neutrino coupled WIMP. Looking at both the resulting ^3He and ^7Li abundances we recognize the same tendency as in the D yield; a chemical potential corresponding to $\phi_\chi \approx 0.5$ for small WIMP masses is equivalent to the $m_\chi \to \infty$ limit.

Allowing for Equivalent Neutrinos

In figure 3.10 the combined D and ^4He yields are plotted for a complex scalar with the same mass-range as in figures 3.8 and 3.9, for $\Delta N_\nu = 0$ (solid lines) and $\Delta N_\nu = 1.0$ (dashed lines). The results are shown for $\phi_\chi = 0$, 0.3 and 0.5. The blue solid straight line illustrates the $m_\chi \to \infty$ limit, and is not to be confused with the $\phi_\chi = 0.5$, $\Delta N_\nu = 0$ line. Also included is the $m_\chi = m_e$ line for electromagnetically coupled WIMPs, in addition to the $m_\chi = m_e$ yield for a $\phi_\chi = 0.5$, $\Delta N_\nu = 0$ neutrino coupled WIMP, illustrated with a black dot. The fact that this coincides with the $m_\chi \to \infty$ limit for $\Delta N_\nu = 1$ WIMPs is a mere coincidence.
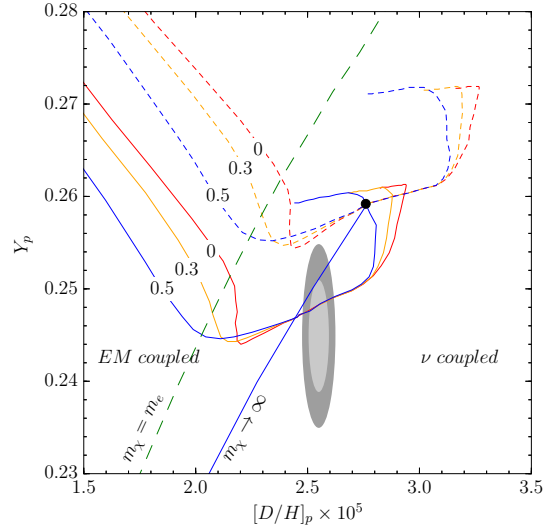

Figure 3.10: The combined $[D/H]_p$ and Y_p yields for three different constant degeneracy parameters ($\phi_\chi = 0.0$, 0.3 and 0.5) for a complex scalar. The solid yield lines correspond to $\Delta N_\nu = 0$, while the dashed ones correspond to $\Delta N_\nu = 1$. The blue solid straight line illustrates the $m_\chi \to \infty$ limit and the green dashed line shows the yields for an electromagnetically coupled WIMP with $m_\chi = m_e$ and varying ΔN_ν and ϕ_χ. Also, the $m_\chi = m_e$ yield is shown as a black dot for a neutrino coupled WIMP for $\Delta N_\nu = 0$ and $\phi_\chi = 0.5$. The gray-shaded ellipses correspond to the joint $[D/H]_p$ and Y_p 1σ and 2σ confidence intervals respectively.

We observe that the $m_\chi \to 0$ limit for the neutrino coupled WIMPs extend beyond the $m_\chi \to \infty$ line as the chemical potential is increased to significant values. As suspected from the individual constraints analyzed in figure 3.9, small WIMP masses ($m_\chi < m_e$) are still not strongly favored, although the fit has become better. It is very interesting to note, however, that by using the Nollett & Steigman observational bound on the ^4He yield, small WIMP masses now fall inside the 2σ constraint also for a complex scalar and a Majorana fermion, provided that $\Delta N_\nu = 0$ and the chemical potential is high enough ($\phi_\chi \approx 0.5$).

This is in contrast to the Nollett & Steigman results, where a $m_\chi < 35$ MeV neutrino coupled WIMP was strongly ruled out, except for a small allowance for a $m_\chi \ll m_e$ real scalar.

Without doing any parameter estimations we may still conclude that adding a chemical potential to electromagnetically coupled WIMPs will not provide any better fit than the $\phi_\chi = 0$ case. In the neutrino coupled case however, we see an increased favoring of small WIMP masses with an increasing chemical potential. Using the Nollett & Steigman-adopted bounds on the ^4He yield this makes an interesting case in combination with the shift in the D values due to the update of η and the reaction rates, since small neutrino coupled WIMP masses now become more favored.

Chapter 4

A New Measurement of the Primordial Deuterium Abundance

In chapter 1.2 we learned that due to its high sensitivity to the total baryon density and its rather simple post-BBN evolution, the deuterium abundance is of particular interest when probing the early universe. There we also briefly discussed the general approach of measuring the primordial abundance of the element. Light emitted from distant quasars may be absorbed in intervening gas clouds before it reaches our telescopes, and gives us information about the elemental composition of the absorption system. We are particularly interested in Damped Lyman α absorbers (DLAs) since the absorption in such systems are high enough to be detected but still low enough to provide distinctive absorption features.

Parallel with the updating of *AlterBBN* I have conducted an analysis of the absorption system towards the quasar *Q1009+2956* (also known as *J101155+294141*) at redshift $z = 2.407$, with the aim of measuring its deuterium content. Due to a complex structure of absorption lines, contaminated by a number of blends from other systems, it has proven difficult to arrive at a satisfactory model for the system. In particular, absorption features from a system at redshift $z = 2.429$ is found to blend with the spectra from the system at $z = 2.407$, resulting in problems of identifying the redshift and dynamic broadening of the absorption lines. The efforts have resulted in the development of a computer code, written in *PYTHON*, that improves the plotting environment of the software used to fit the absorption lines. This combines the spectra and model fits for different observations, removing possible contaminations to the data and re-binning all spectra to the observation with the highest resolution. The different data is weighted by their errors, resulting in a better representation of the real structure of the system analyzed. In this chapter I will discuss this add-on to the absorption line software used, and the present status of the analysis of the absorption system at $z = 2.407$.

4.1 Computational Tools

4.1.1 ALIS

The absorption systems are modeled by a Voigt profile for each of a number of discrete absorbers. The software used is *ALIS* [2], a *PYTHON* program developed by R. Cooke, which uses a modified version of the *MPFIT* package [93]. *MPFIT* employs a Levenberg-Marquardt least-squares minimization algorithm to derive the model parameters that best fit the data (i.e. the parameters that minimize the difference between the data and the model, weighted by the error in the data). *ALIS* has the advantage of being able to fit an arbitrary emission profile for the quasar whilst simultaneously fitting to the

absorption from the Damped Lyman-α system (DLA). Any uncertainty in the continuum is therefore automatically folded into the final uncertainty in the D/H ratio. The model parameters to be fitted for each velocity component are the redshift (z), the column density ($\log(N)$ with N in cm^{-2}), and the dynamic line broadening b (in km s^{-1}). The dynamic broadening is a combination of turbulent motion in the gas an thermal broadening of the lines, given by

$$b^2 = 2\sigma^2 = b^2_{\text{turb}} + 2k_B T/m \, , \tag{4.1}$$

where σ is the Gaussian velocity dispersion of the gas, T its temperature, and m is the mass of the atomic species. For all the transitions, the atomic data compiled by Morton 2003 [94] is used.

4.1.2 A New Program for Stacking the Data

The plotting environment in *ALIS* does not have the functionality of stacking data from different observations, rather each transition of each observation is plotted individually. The individual data may contain bad data (e.g. bad pixels) or suffer from loss of data or other contaminations, and this may e.g. mimic structure where there is none. Such data usually come with large errors, and is consequently given a small weight in the minimization process of *ALIS*. However, for the program to work properly, it is essential to make good initial guesses of the line structure, and although bad data do not influence the χ^2 much it is still evident on the individual plots. For illustration purposes it is therefore convenient to combine all the observational data and fitting models of each transition into one composite spectrum. This helps us to get a better picture of the real structure of the absorption features, as well as reducing the number of plots.

For this reason I have written an external *PYTHON* code for the purpose. The code does not interact with *ALIS*, other than collecting the final model fit results as well as the observational data going into the fitting process. Using the *Barak* environment [95] for *PYTHON*, both the observational data and the model fits are stacked (including the continuum and the zero level), wighted by their error, and presented as seen in the right panel of figure 4.1. The wavelengths are represented as velocity offsets relative to the main absorption line (in km s^{-1}), and the plots of the metal and Lyman transitions separately share the same x-axis, for an easier comparison of the structure. The stacked fitting model is plotted over the stacked data points, with the residuals (the difference between the model and the data) and the error in the observational data alone also included. The size of the residual bar is normalized to the mean size of the residuals and is therefore an indicator of how good the fit for the specific transition is. The error bar (at the bottom of the plots) is included as a hint to where in the fitting interval the main focus should be directed to arrive at a good fit. Small errors combined with large residuals will lead to a large χ^2, while large errors combined with the same residuals will not be as important in the calculation of χ^2. Thus, in the case that the residuals are quite small, the χ^2 may still be significantly affected if the error in the data is also very small.

All absorption lines are named according to the name they are given in the *ALIS* input file. For each transition, the user of *ALIS* must provide a unique ID corresponding to each of the observations covering that transition. The external stacking program demands that the correct transition name is part of this ID to be able to combine the relevant observations for that transition, but the atomic mass may be omitted (a minimum is e.g. SiII1193). The remaining part of this ID is written in the top right corner of the plots, and should therefore provide information about the specific observation (e.g. the full ID should be something like vltSiII1193). This way, the plots provide information on which observations that go into the stacking.

The stacking program also provide plots of the individual observations, since it is often informative to analyze these as well. The design is the same as for the stacked plots, but I have changed the color of the residual bar to be able to distinguish them from each other.

In figure 4.1 I have shown as an example the Al II 1670 transition in the $z = 2.407$ system. In the left panel all three observations that have been used in fitting the absorption lines in this transition are plotted
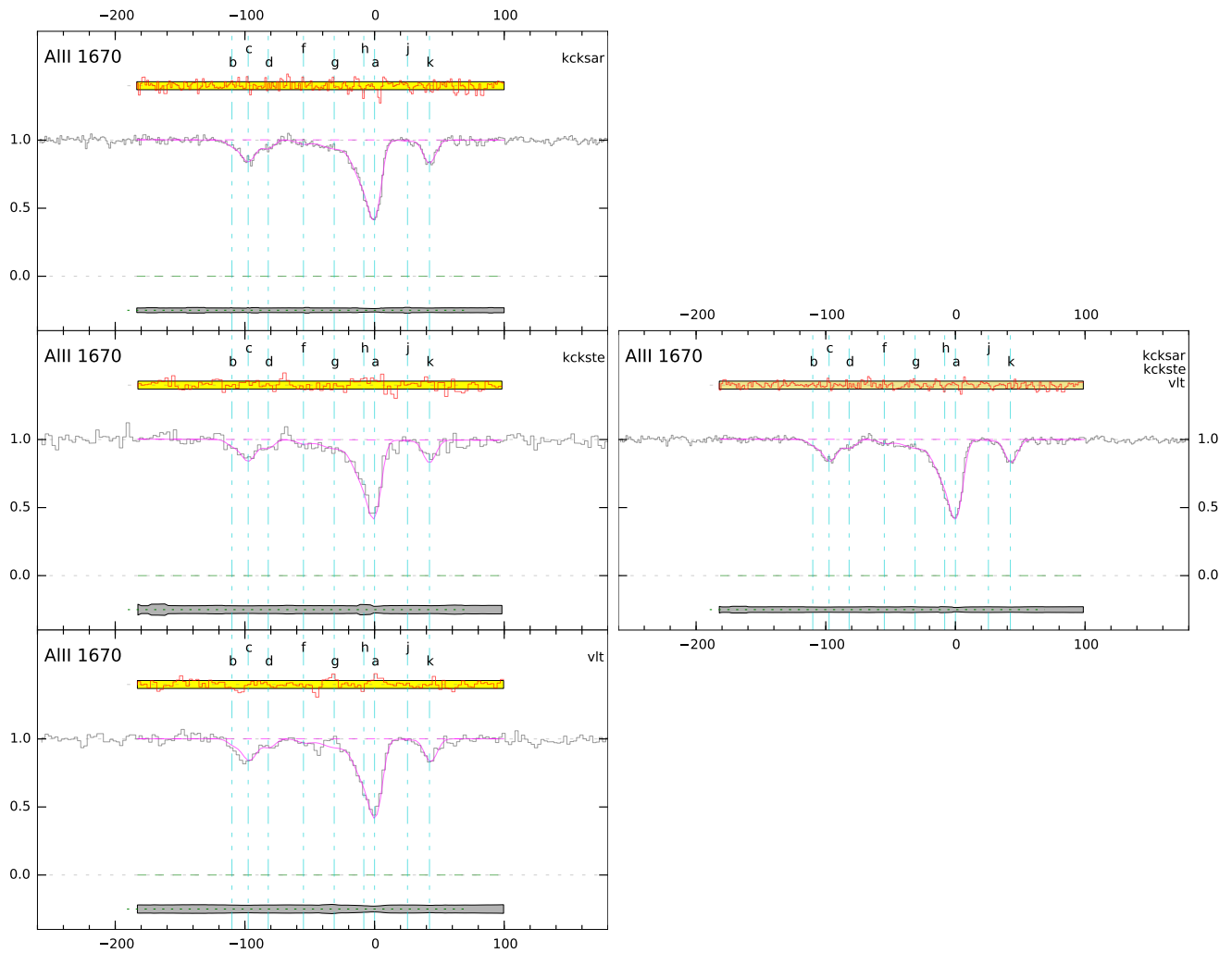
Figure 4.1: Example illustration of how the stacking program works, using the Al II 1670 transition in the z = 2.407 system analyzed in this chapter. Left panel: Individual plots of the three observations that go into the fitting of the transition structure. Right panel: Plot of the composite spectrum and model fit. The stacked model is the blue line plotted over the stacked data. The very dim dashed gray lines correspond to the flux-values 0.0 and 1.0, while the zero-level and continuum are plotted as dashed green and blue lines respectively. The error in the observational data is plotted at the bottom (also stacked), while the residuals are the red lines plotted over the khaki-colored box above the spectrum. The size of the box is normalized to the mean of the residuals. At the very top we find the line IDs for the metal lines, representing each of the absorption lines used in the fitting, plotted as turquoise dash-dotted lines. Hydrogen (^1H) lines are represented by orange dashed lines and deuterium lines (^2H) by blue dash-dotted lines, but neither are found in this example plot. The IDs of the observations that go into the fitting of the transition are printed in the top right corner, while the name of the transition itself is found in the left top corner. The vertical axis shows the normalized flux, and the horizontal axis represents the velocity offset relative to the central redshift, given in km s^{-1}.

individually. As we see the three observations have different resolutions. In the stacking program the data from the observations with the smallest resolution are re-binned on the highest resolution data set (here *kcksar*). In this case the *kcksar* observation has the smallest error of the three and is consequently given the largest weight in the χ^2 minimization process of *ALIS*, as well as in the stacking. Thus the stacked plot to the right resembles this the most. In the *kckste* and *vlt* observations we observe that there are some irregularities. The most prominent ones are found at ~ -70 km s^{-1} (between lines d and f in *kckste*) and at ~ -40 km s^{-1} (two irregularities between lines f and g in *vlt*). The latter two may lead us to think that there is an absorption line (left irregularity) and the total lack of one (right irregularity) respectively, when in fact the other *kcksar* and *kckste* observations point to the opposite. By stacking the

three plots, the two KECK observations are given a much larger weight and we see that in the stacked plot the irregularities in the *vlt* observation are completely washed away. This program makes a powerful tool in detecting the true structure in an absorption system, and is handy for illustration purposes. However, there is a limitation to it that I have not yet been able to reconcile.

If an observation that goes into the analysis is missing data for some wavelength ranges, the stacking process results in the combined error being very large (since the error in the missing data points is set to be very large). This results in the combined residuals for these data points being essentially zero, regardless of the residual vale for the remaining observations. The stacking program allows for a cut-off of the interval for the individual observations, removing the wavelengths in question from the stacking process. However, the interval must still be continuous, so the cut-off have to include all wavelengths to the left or right of the reduced interval. For example, two observations have a continuous set of data points in the interval [4100,4105], and a third set of data is included that are missing data in the interval [4100,4102]. Then this third set may be included with a reduced interval [4102,4105]. However, if the missing data is e.g. in the range [4102,4103], then the stacking program is not able to stack only the observations which have data in that range. Of course, *ALIS* have no problem handling this eventuality, since all observations are fit individually. However, it is worth noting that this is a limitation of the stacking program.

4.2   Observational Data

The observations that have been used are listed in table 4.1. They include two observations from the archives of the High Resolution Echelle Spectrometer (HIRES) at the Keck Observatory[1], as well as one observation from the archives of Ultraviolet and Visual Echelle Spectrograph (UVES) at VLT[2]. The spectra have been normalized to the quasar emission continuum (KECK: [96], VLT: [97]), and it is assumed that the continuum shape does not change abruptly over small ranges compared to the absorption lines. Originally, a fourth set of newly released data (Tytler) from the Keck HIRES instrument was included. However, it did not seem to be fully normalized, and the main absorption feature for all the included Lyman transitions and all but three of the metal transitions was contaminated by several discontinuities. For the VLT observation there exist no data on the Lyman series, thus all Lyman fits are made using only the Sargent and Steidel data. The VLT data has been treated as in Riemer-Sørensen et al. 2015 [32].

We cut off an interval corresponding to a velocity offset of $\sim \pm 200$ km/s for the metals and $\sim \pm 400$

Date	Primary investigator	Instrument	Settings *	Resolving power	Observation time [ks]
2005-04-30	Sargent	Keck HIRES	0.861″, 3101/5980 Å	47700	4x3.0
2005-05-31	Steidel	Keck HIRES	1.148″, 3101/5983 Å	71600	4x1.8
2007-06-05	Murphy	VLT UVES	1.000″, 4159/6210 Å	45000	3.0

Table 4.1: Observational data used in the model fitting.
* Slit width and blue/red wavelength limit.

km/s for the Lyman transitions to simplify the fitting process. The specific intervals varies a bit for each transition, to make sure that we include everything that may affect the model fitting. Ideally we would want the interval to extend to the unabsorbed continuum on both sides of the interval, but we see that this is difficult to achieve for some of the transitions. To account for any uncertainty in the emission

---

[1] `http://www2.keck.hawaii.edu/koa/public/koa.php`
[2] `http://archive.eso.org/cms.html`

continuum modeling[3] I have added a flat continuum to the Voigt profile model around all absorption lines. In the case that the unabsorbed continuum is available on both sides of the interval we allow for a slope on the continuum (C II 1334, Al II 1670, Ly β, Ly δ), otherwise we keep the slope fixed at zero. Due to different settings for the different observations the spectra might be shifted relative to each other. We allow for this possibility by adding the shift as a free parameter to each of the observations.

4.2.1 Lyman Series
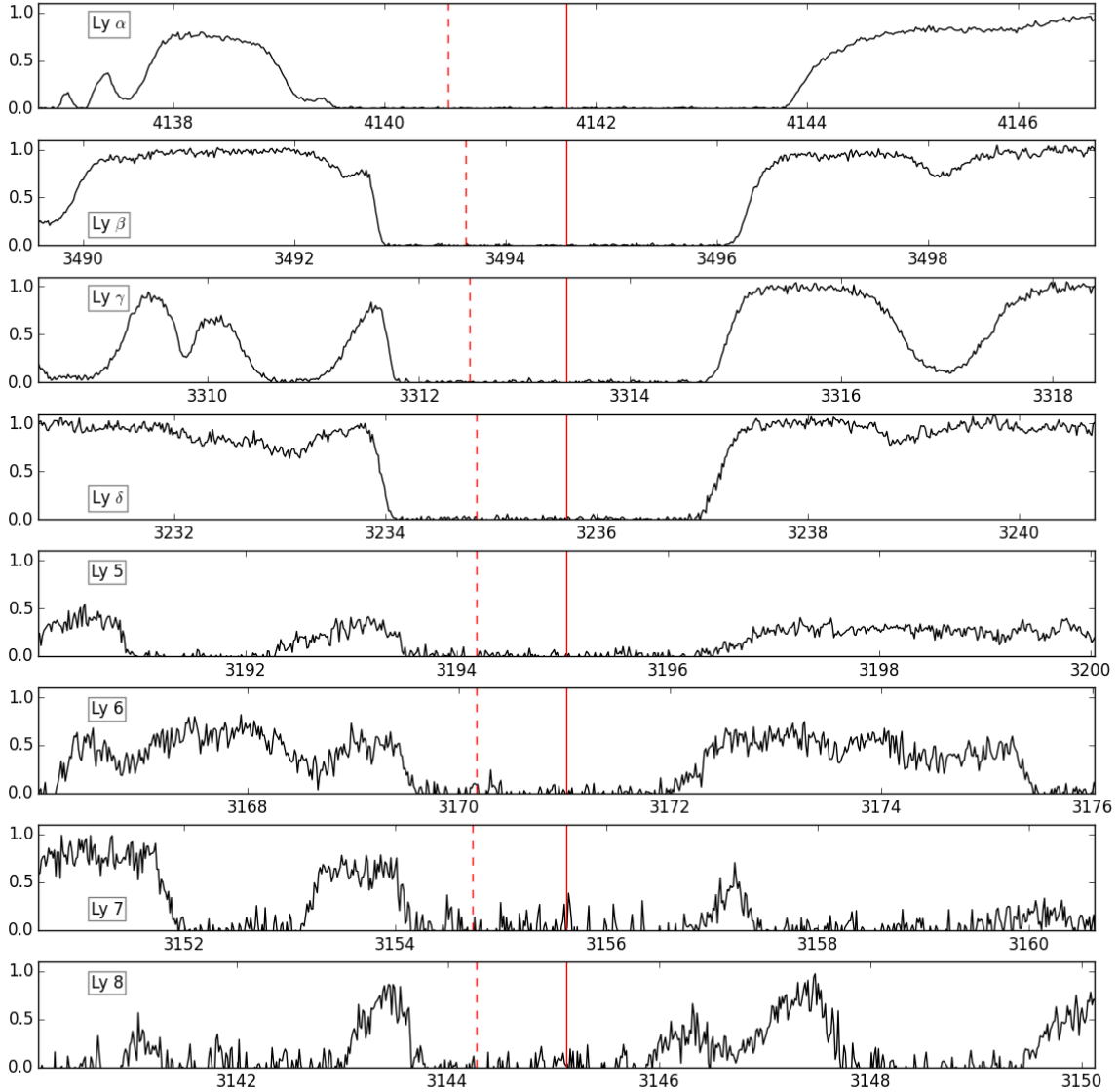
Figure 4.2: The first eight transitions in the Lyman series for the absorption system. The hydrogen line of the main absorber at $z = 2.407$ is shown as a red solid line, while the red dashed line shows the corresponding deuterium line. The Sargent have been is used for this illustration.

I have chosen to include the first eight Lyman transitions in the analysis, plotted in figure 4.2 using the Sargent data. In this figure the central hydrogen line is illustrated by a solid red line, while the corresponding deuterium line, offset by 82.9 km s^{-1}, is shown as a dashed red line. For the rest of the

---

[3] This is a process done by the publishers of the data

series, there is not enough information in the spectra to arrive at a good fit.

4.2.2   Metal Transitions

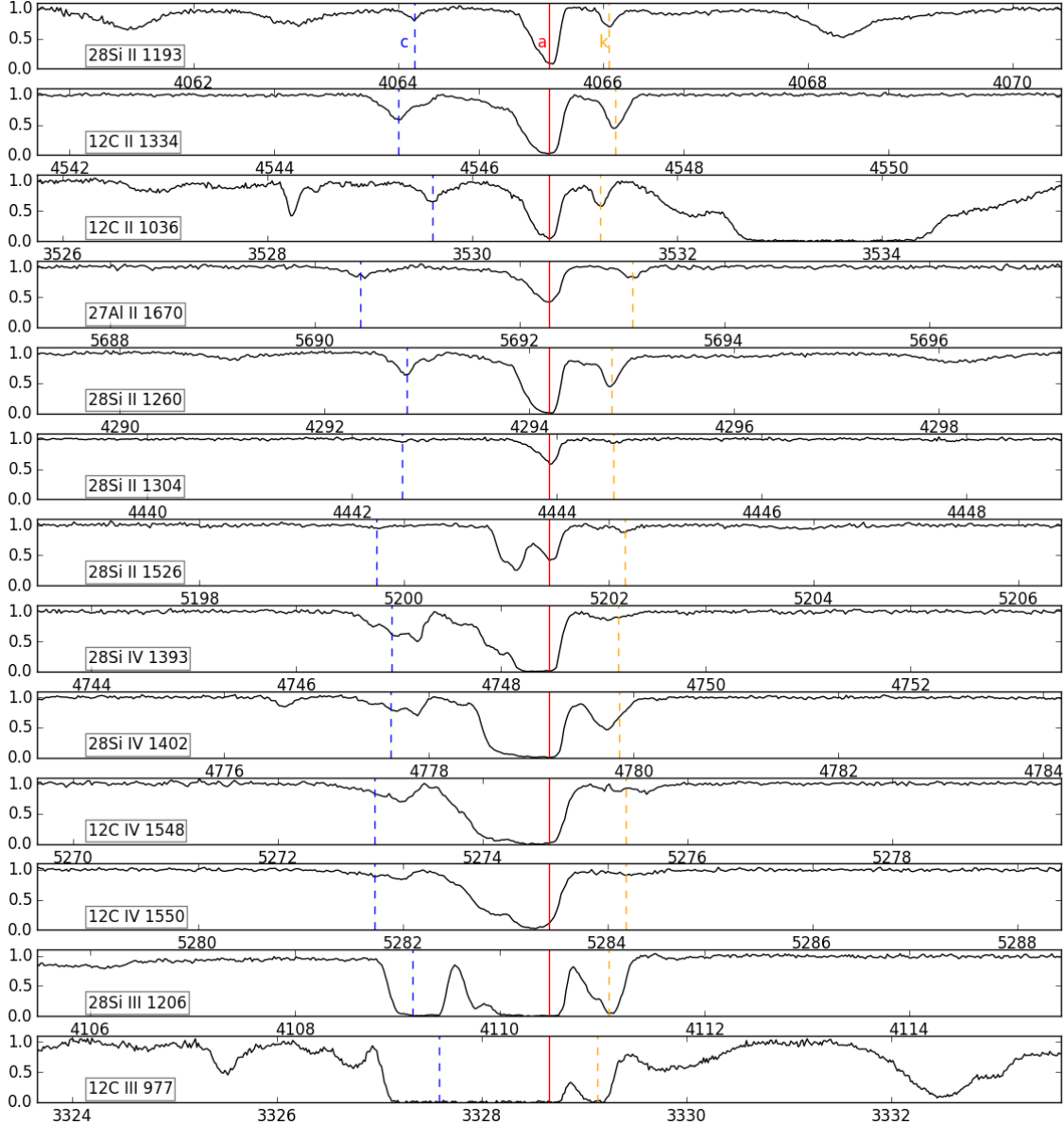*Figure 4.3: The most promising metal transitions for the absorption system. The red solid line shows the location of the main absorber at z = 2.407, label as line a (labels are marked only in the top plot). The asymmetry of the main absorption feature suggests that there are more than one absorber present. Two other absorption features, clearly showing the presence of at least two lines in each, are found at z ∼ 2.4058 (c) and z ∼ 2.4074 (k) and illustrated by a blue and orange dashed line respectively. The Sargent data have been used for this illustration.*

In figure 4.3 I have plotted the most promising metal transitions using the data from the Sargent observation. We see that apart from the central absorption feature around the central line at $z = 2.407$ there are two more features that can be identified in all transitions, one at $z \sim 2.4058$ and one at $z \sim 2.4074$ (although they are present in Si II 1304 the absorption is so low that the features are barely distinguishable from the continuum). The central absorption feature is illustrated by a solid red line and labeled as line a, the feature to the left is illustrated by a dashed blue line and labeled as line c, and the feature to the right is illustrated by a dashed orange line and labeled as line k. The asymmetry of the three features

also tells us that they are made up by at least two absorbers each.

4.3   Analysis

The ultimate goal of the fitting process is to determine the correct column density of ^1H and ^2H for all absorption lines that are part of the system we examine, which requires precise estimates of the redshift and dynamic broadening of the lines as well. Looking at figure 4.2 we see that with this many lines present it is impossible to accurately determine these parameters only by analyzing the Lyman absorption features. The column densities of ^1H and ^2H are generally much higher than the column densities of the different metals, thus the real structure is easier to observe in the metal absorption features. For this reason we want to include as many metal transitions as possible.

4.3.1   Fitting the Metals

In Si II 1193, C II 1036 and Si II 1260 there are some additional structure to the immediate left and right of lines c and k respectively, which suggest that they might be contaminated by at least one blend. Also the two III-transitions at the bottom of figure 4.3 are clearly submission to several blends. For C II 1036 the flux reaches approximately continuum to the immediate right of line k before showing a Lyman-like behavior for higher wavelengths. The wavelengths here do not coincide with any of the Lyman-transitions for the system at $z = 2.407$, nor the system detected at $z = 2.429$, suggesting that another system may be blending in with our data. Cutting the fitting interval at the point where the flux reaches approximately continuum to the right of line k gives a good fit for this absorption feature, combined with the other metal transitions. However, for the features around lines c and a we need to include one blend in each, in addition to a blend to the left of c to make it compatible with the other metal transitions. Looking at the behavior of the flux for this transition, it obviously do not reach the continuum before wavelengths much shorter than the feature around line c, so it does indeed seem likely that this transition is contaminated with a continuous set of blends.

For the transition Si II 1193 it seems that the central absorption feature is unaffected by any blends, and that the problem is confined to the features around c and k. Including two blends to the left and right of these features seem to reconcile the problem, without affecting the absorption features too much. For the transition Si II 1260 however, the whole fitting interval seem to be affected by blends, which is evident from looking at the area between a and k. The blending does not lower the flux by much, but lead to a constant reduction over the whole interval, masking the information needed to fit the transition. Attempts to include this transition led to a much poorer fit of the area around the central absorption line (a) in the other transitions, suggesting that the redshift and dynamic broadening of the blend is not well determined. Consequently, this transition was left out of the analysis. The same constant lowering of the flux is evident at the left wing for the transition Si III 1206. However, fitting this problematic area with two blends gave good agreement with C II 1334, C II 1036 Si II 1193 and Al II 1670 without affecting the metal structure around the c line. C III 977 have a very complex blend structure as well. Trying to fit this it was evident that at least one blend is present around line c, and the whole structure is so saturated that it is difficult to nail down its position. This large saturation also leads to a uncertain determination of the other lines. In the attempt to fit this transition it became clear that the extra structure around 3326.5 Å, as well as the blend to the immediate left of line c, resembles metal lines. This suggests that absorption from another system is blending in with C III 977, since these lines are not evident in any other transition.

We note that the continuum is reached on each side of the cut-off interval for all the Si IV and C IV-transitions. However, fitting these transitions alone, I found that the two Si IV-transitions (Si IV 1393 and Si IV 1402) were not compatible with each other. The feature around k shows a much larger column

density for Si IV 1402 than for Si IV 1393, which cannot be explained without imposing blending, since they are of the same ion and should have similar column densities. An identical problem was apparent also in the central absorption feature. Note the short energy gap between the two Si IV-transitions. By coincidence, this corresponds to a velocity offset from $z = 2.407$ that coincides with the system at $z = 2.429$, with the consequence that the absorption from Si IV 1393 in the latter and the absorption of Si IV 1402 in the former is observed at almost the exact same wavelengths (see figures 4.3 and 4.10). The extra absorption of Si IV 1402 in $z = 2.407$ is actually due to absorption of Si IV 1393 in $z = 2.429$, and information of the real structure of Si IV 1402 is lost.

Combining Si IV 1393 with the two C IV-transitions also led to a considerably poorer fit than using C IV 1548 and C IV 1550 alone. When including both II -and IV-transitions we need to remember that the ionization energies for the two ionization levels are very different. This means that depending on the temperature of the system there might be a considerably different amount of absorption for II -and IV-ions. In table 4.2 I have listed the ionization energies for the levels I, II, III and IV for the relevant elements in the analysis, and we note that the ionization energies for Si IV and C IV also differ significantly. Combining C IV 1548 and C IV 1550 with the II-transitions led to a poor fit, and it seems like the ionization levels contain a rather different structure. The major issue with the C IV-transitions however, is that the main absorption line (a) seem to have a vanishing column density, i.e. it is too cold to lead to significant absorption of these transitions. The prospects of adding too much complexity to the model, and the lack of absorption of the main line led to a removal of all IV-transitions.

Element	Atomic mass	ΔE_1	ΔE_2	ΔE_3	ΔE_4
H	1.01	13.60	-	-	-
D	2.01	14.51	-	-	-
C	12.01	11.27	24.39	47.89	64.50
Al	26.98	6.00	18.83	28.45	119.99
Si	28.09	8.16	16.34	33.49	45.14

Table 4.2: The ionization energies for the elements relevant for the model fitting. ΔE_i is the ionization energy for the ith ionization level in units of eV, while the atomic mass is in units of g mol^{-1}.

The masking of Si IV 1402 by the absorption of Si IV 1393 in $z = 2.429$ was not discovered before until very recently, and I have not had the time to analyze it further. For the problem of fitting the rest of the IV-transitions, there is no obvious blending from the $z = 2.429$ system. However, there have not been enough time to analyze this system properly. In addition, some other systems with the potential of blending with $z = 2.407$ was discovered alongside with the detection of the $z = 2.429$ system. Suffice to say, those need to be analyzed properly before an accurate model of $z = 2.407$ may be achieved.

There is not as much absorption for Al II 1670 as for the other II-transitions, but except for one line in the area between a and k there is still enough information to fit the remaining lines. For Si II 1304 however, the lack of information led to problems in fitting it with the rest of the Si II-transitions, so I had to leave this out as well.

Starting with the Simplest Transitions

Keeping in mind that there are some important issues to be resolved before an accurate estimate of the deuterium abundance in $z = 2.407$ may be found, I continue by presenting the, for now, best model of the spectra from the system, while highlighting the main problems. It is a generally good idea to start with the transitions that seem to have the simplest structure, and that are absent of blends. Moreover, since the different ionization levels may be represented very differently, it is wise to try to determine the basic structure solely by fitting II-transitions. Later, when this is satisfactory determined, we may add III- and IV-transitions to see if there are some extra lines, not evident in the II-transitions. Figure 4.4 shows the best fit of the two simplest transitions. The continuum is reached on both sides of the fitting

interval and there is no sign of any blends in the proximity of the main structure. However, we see that a considerable amount of lines is needed to reveal the basic structure.
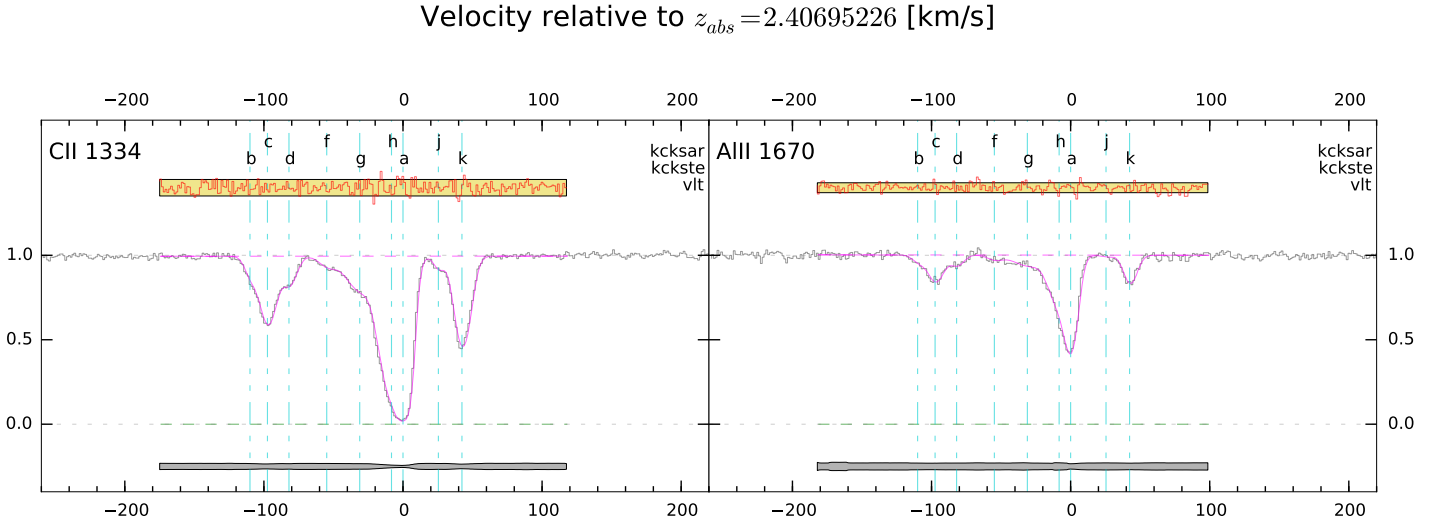

Figure 4.4: The best fit of the two simplest transitions, both devoid of any blends. They provide a good starting point for further fitting, since the basic structure is easily determined in the absence of blends.

Investigating the Structure in III- and IV-transitions

Without making any attempts to optimize the fit, I have added the transitions Si III 1206, C III 977, C IV 1548 and C IV 1550 to the basic model, and the result is seen in figure 4.5. The model parameters in this fit have been fixed, since the purpose is to see how well the structure found in the basic fit applies to other transitions, as well as search for structure in the III- and IV-transitions that may not be evident in the II-transitions. Fixed parameters are labeled with capital letters in *ALIS* and illustrated accordingly by the external stacking program. Looking at the C IV-transitions we observe that although the central absorption feature seem to have a good fit, the residuals are very high, caused by the low error in the data. Adding more lines slightly improved the fit, but it is obvious that they contain some additional structure, making it difficult to accurately determine the model parameters. The area around the main absorption line is particularly problematic, which is best fit with a vanishing column density. However, including an additional line to the right of *k* did fix this part of the spectrum, and was consistent with the rest of the transitions, as well as improving the fit in Si III 1206. Although the two C IV was removed, this additional line was kept in the further analysis.

There are obviously several blends in the C III 977-transition, and the large saturation of the absorption lines results in large uncertainties in the dynamic broadening. What is interesting though, is that the structure between ~ -120 and ~ -240 km s^{-1} is best fit with metal lines. In particular, there is obviously a line to the left of line *b*. Trying to fit this transition, while keeping it consistent with the other transitions, *b* gets an unphysical dynamic broadening ($T \approx 3 \cdot 10^5$ K and $b_{\mathrm{turb}} > 20$ km s^{-1}) without imposing an extra line here. Moreover, an identical problem was recognized in the Lyman transitions at about the same redshift, suggesting that there might be structure here that is part of the system. However, there is a lack of information about this line in the other metal transitions, which causes concern. Looking at the additional structure to the left of this line, it is not unlikely that it is part of another system that blends in at this wavelength, and that the problems in the Lyman transitions are also simply due to a random blend. A more thorough analysis of potential blending systems need to be carried out to be able to determine the structure of this transition. Consequently, C III 977 was left out of the analysis, and the additional lines assumed to be metal absorption from another system blending in with the system at $z = 2.407$.
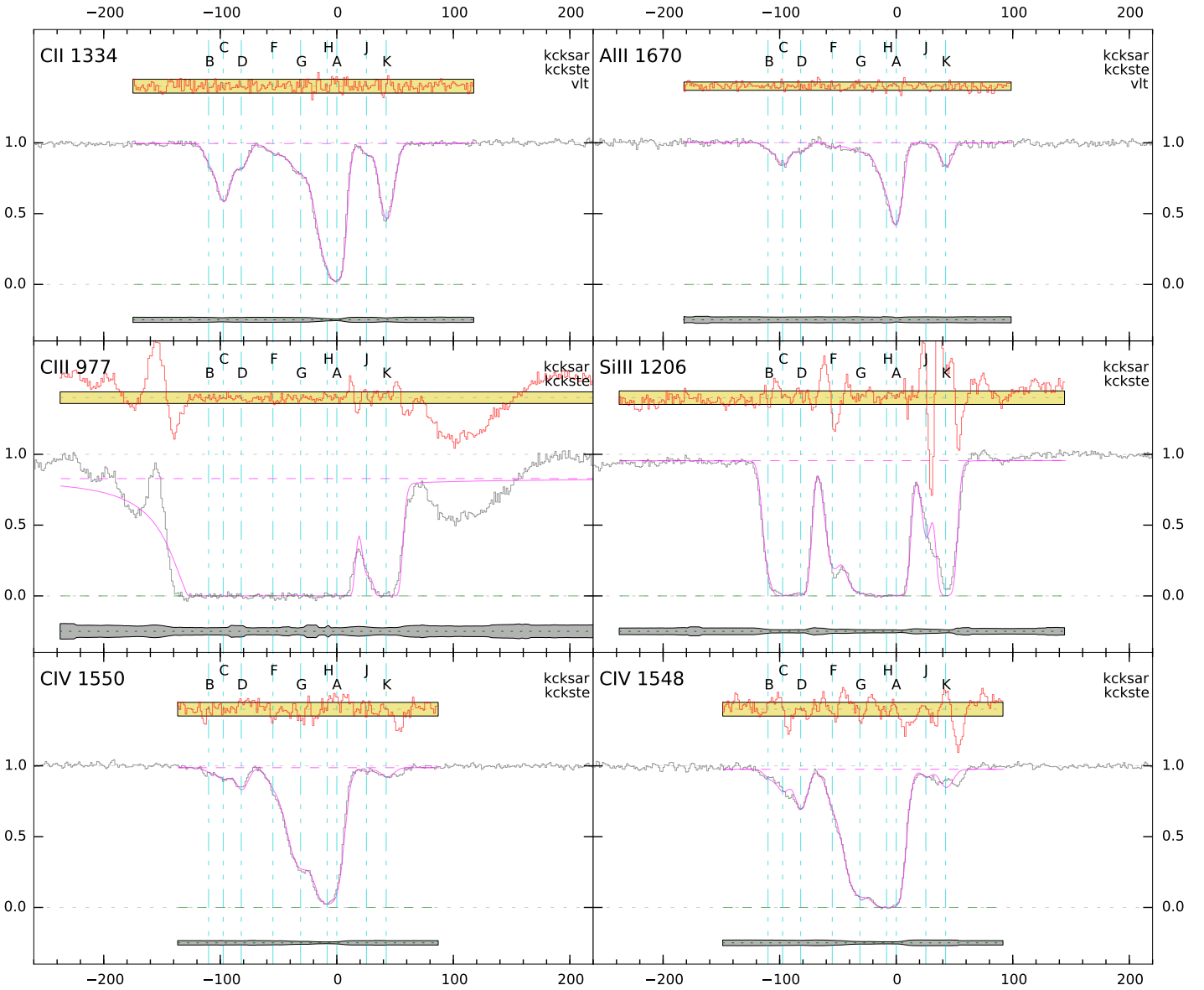
Figure 4.5: Here we have added two III- and two IV-transitions to search for structure that are not evident in the II-transitions. The reason for the capital letters in the absorption line labels are due to a fixing of the redshift in this fit. The purpose here is to spot differences for the ionization levels, thus the all the model parameters (redshift and dynamic broadening) from the basic model in figure 4.4 have been fixed. No attempt to optimize the fit have been made here, and I have omitted obvious blends in C III 977.

Fitting the Full Metal Model

As mentioned earlier in this section we had to remove Si II 1260 and Si II 1304 from the fit, the former due to problematic blends. Combining Si II 1304 with Si II 1193 lead to a poor fit in the central absorption feature. This may be due to the lack of information for several lines in Si II 1304 (the amount of absorption is too low). In the worst case there is something wrong with the fit of Si II 1193. However, this transition lead to a better fit with C II 1334 and Al II 1670 than Si II 1304 do, so I have decided to discard the latter. The Si II 1526 transition was not compatible with any other lower-ionized metal transitions. Looking at figure 4.3 there seems to be some additional structure in the same area as the
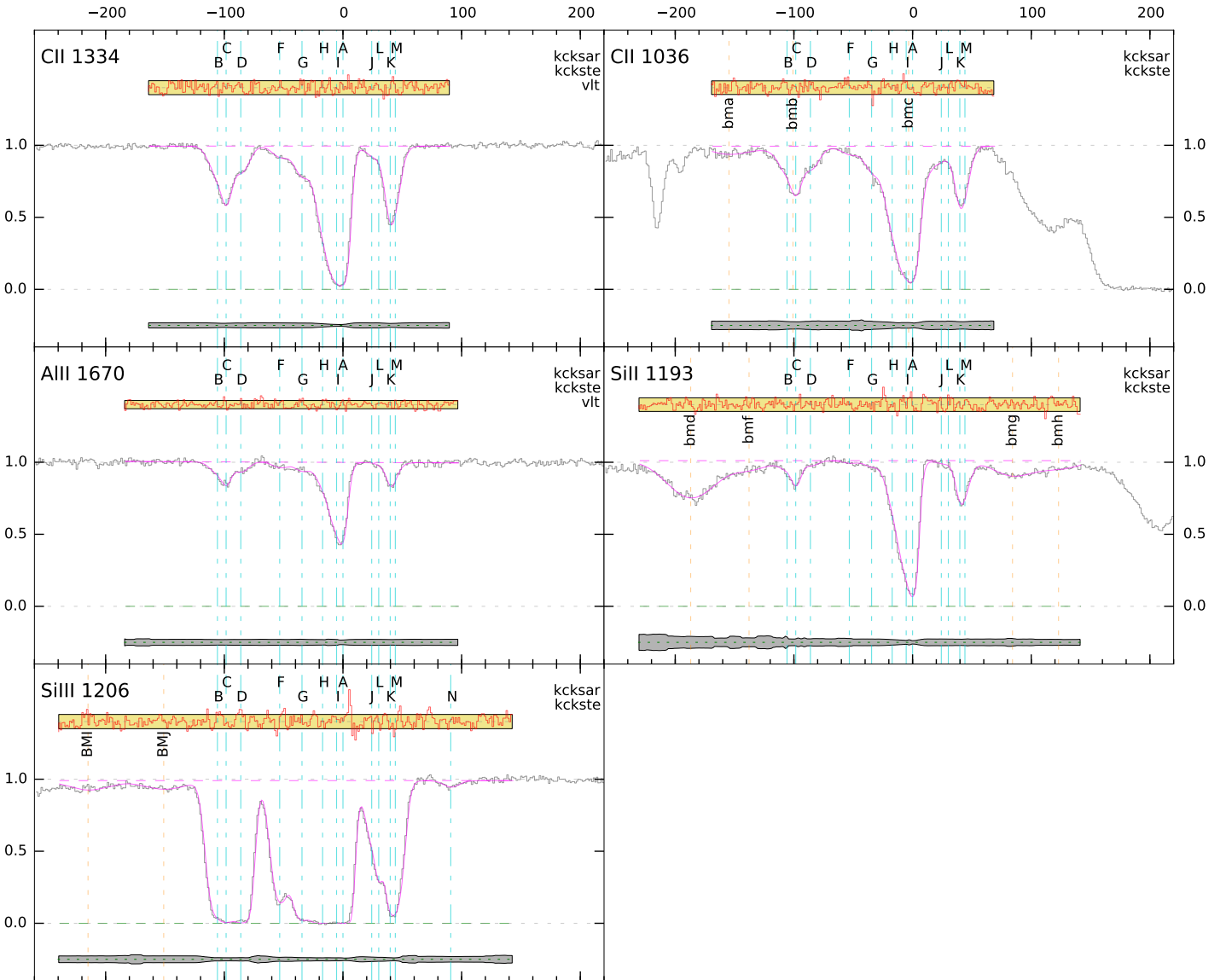
Figure 4.6: *C II 1036 and Si II 1193 added to the basic model from figure 4.4. The transition Si III 1206 was first included, helping identifying some extra structure. Due to problems in the absorption feature around the k line and a vanishing column density for the main absorption line (a) this was later removed, but keeping the extra structure, fixing the line parameters to the ones fitted here. The lines labeled l and n here was not included in the subsequent fitting, imposing too much degrees of freedom to the model. The lines might just be blends, since they are not clearly recognized in the other transitions. The form of the l line suggest that it is indeed a metal line. However, fitting it with the Lyman transitions favored the absence of a line at this redshift by leading to vanishing ^1H and ^2H column densities. Note that the labels of blends not identified as part of the system including the main absorption line is written below the residual box, to better separate the two differing types of absorption lines. All blend labels for the metal transitions start with the same two letters, **b**lend **m**etal, while the third letter is unique for each individual line.*

lines *f* and *g* from the fit in figure 4.4. We mentioned a suspected extra structure here. However, any attempt to combine Si II 1526 with Si II 1193 and the two basic transitions failed. Consequently, this transition was also removed.

In figure 4.6 one can see the result from fitting the four II-transitions C II 1334, C II 1036, Si II 1193

and Al II 1670, in addition to Si III 1206. The latter has a great concordance with the former four in the central and left absorption features. One additional line was needed around the main absorption line, which resulted in a better fit for all transitions. Due to the inclusion of this transition we were able to determine the redshift of lines f and g more accurately. The fact that those have a higher absorption in Si III 1206 reveals that the temperature in this part of the system is quite high compared to e.g. the main absorption line a. However, the extra structure around the k line requires two extra lines, in addition to a line at ~ 90 km s^{-1}. We already suspected an extra line to the immediate right of the k-line due to the apparent asymmetry in this absorption feature, particularly evident in the higher ionization levels. The line n might well be a blend, since it is not obviously present in any other transition. The presence of two extra lines in the absorption feature around the k line led to a "over-fitting" of the other transitions, imposing large uncertainties and unphysical values for one of the four lines (the line this happened for varied from run to run due to the uncertainties in the dynamic broadening). Moreover, since Si III has a larger ionization energy than the II-metals, the cold a line was also here fitted to a vanishing column density after a few runs. In the final model I have therefore removed the Si III 1206-transition, while keeping the line labeled m in figure 4.6 (relabeled l in the following).

4.3.2 Tying the Parameters

It is essential to try to identify lines that have similar dynamic broadening parameters to get a best possible picture of the real structure, as well as reducing the number of degrees of freedom in the model. The lines d, f and g was best fit with a temperature of $\sim 2 \cdot 10^4$ K, and were all tied. However, the b_{turb} of line d seems to be a bit lower than the other two, and was kept free. The same applied to the lines h, i and a. The temperatures was best fit to $\sim 0.8 \cdot 10^4$ K for all of them, but the b_{turb} of line a was much lower than the other two, letting it be kept free. Although not very different from d, f and g, line b showed both a bit higher thermal and turbulent broadening, thus I have not tied it to the other three. The rest of the lines are consistent with a thermal broadening of $\sim 1 \cdot 10^4$ K, however, they show slight differences in turbulent broadening.

The fact that finding reasonable similarities in the full dynamic broadening proves difficult, may point to a weakness of the model. We seek to find a simple model as possible that is able to describe the structure of the system. However, even including only four metal transitions the structure seem to be much more complex than we are able to describe with our 11 absorption lines.

4.3.3 Adding the Lyman Transitions

In figures 4.7, 4.8 and 4.9 the full, present best model is shown. The Lyman transitions comes with a series of blends, which combined with the uncertain line structure in the metal transitions have caused serious problems in determining the real structure of the system. Actual Lyman absorptions that are part of the system are labeled starting with the same five letters, **b**lend **l**yman **com**mon, ending with a unique letter for each of the lines. Other blends that are identified in individual transitions might come from metal or hydrogen absorption in other intervening systems. Those are labeled starting with the letters **b**lend **l**yman, followed by a unique letter for the transition in question (a for Lyman α, b for Lyman β and so on), ending with a unique letter for the individual blend. The common blends *blcomd* and *blcomf* are easily identified. However, the three others are not that easily determined, and it is unclear if there actually are three blends here or if its due to some extra line structure. We also take note of the problem at around -140 km s^{-1}, where an additional blend has been included. Fitting the blend with a fixed zero thermal line broadening, one would expect a b_{turb} around $20 - 25$ km s^{-1}. However, it insists on having a $b_{\mathrm{turb}} < 10$, consistent with a metal absorption in the system. Moreover, looking at the Lyman β fit, it is clear that something is missing in the area where a corresponding deuterium line would fall. A
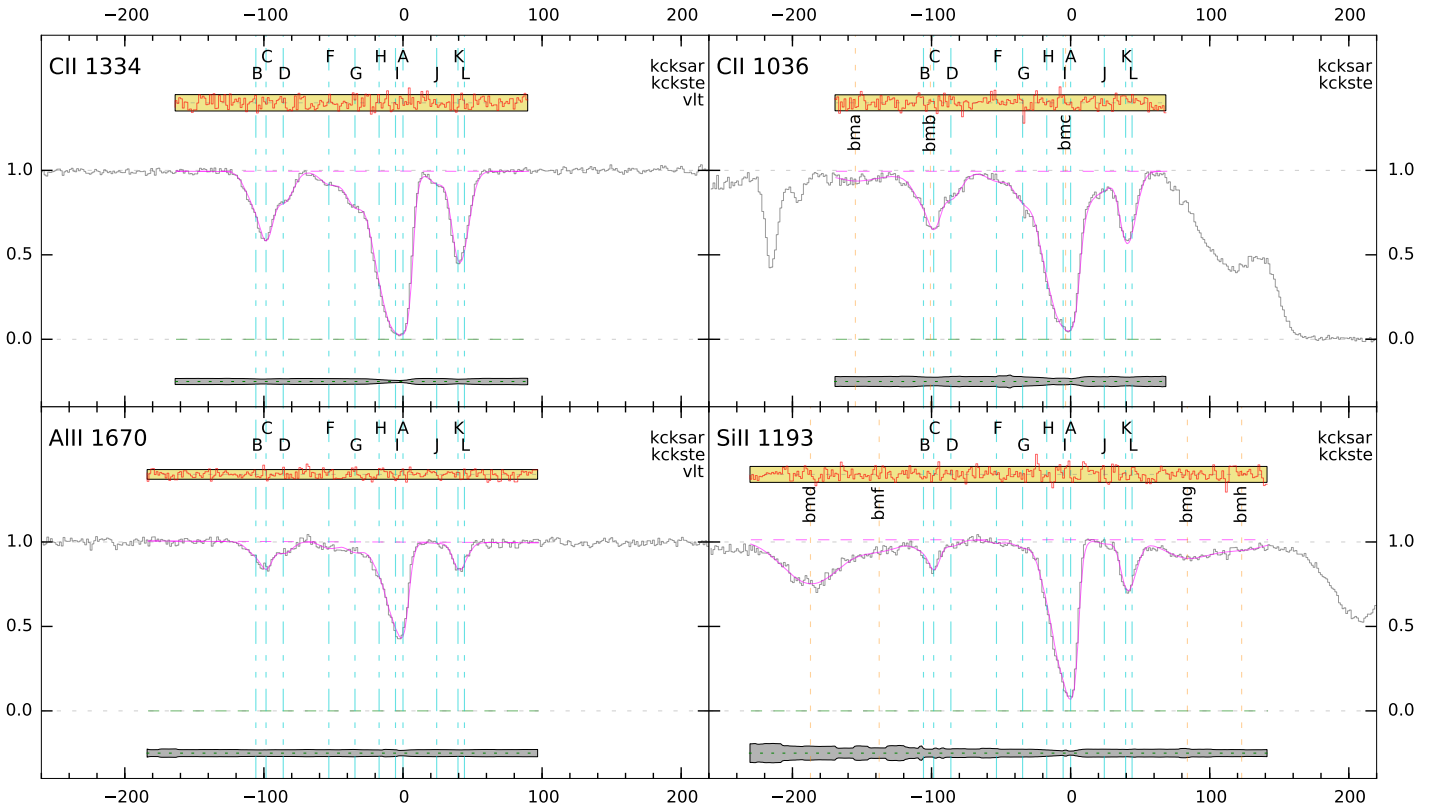
Figure 4.7: All metal transitions part of the present best model.

potential metal line was indeed discovered in C III 977 at about the same redshift, as mentioned earlier. However, it was not recognized in any of the other transitions and is thus probably due to blending. The fact remains that more work have to be conducted in analyzing all potential blending systems before the model can be fully determined.

The group of blends between -260 and -400 km s^{-1} in Lyman α has been identified as Si III 1206 absorption in the system at $z = 2.429$. This transition, along with the other metal transitions as the ones analyzed for $z = 2.407$ are plotted in figure 4.10, and we recognize the Lyman α structure from the system $z = 2.407$ in the spectrum for Si III 1206, which is highly affected by the broad Lorentzian wings of the Lyman α absorption.
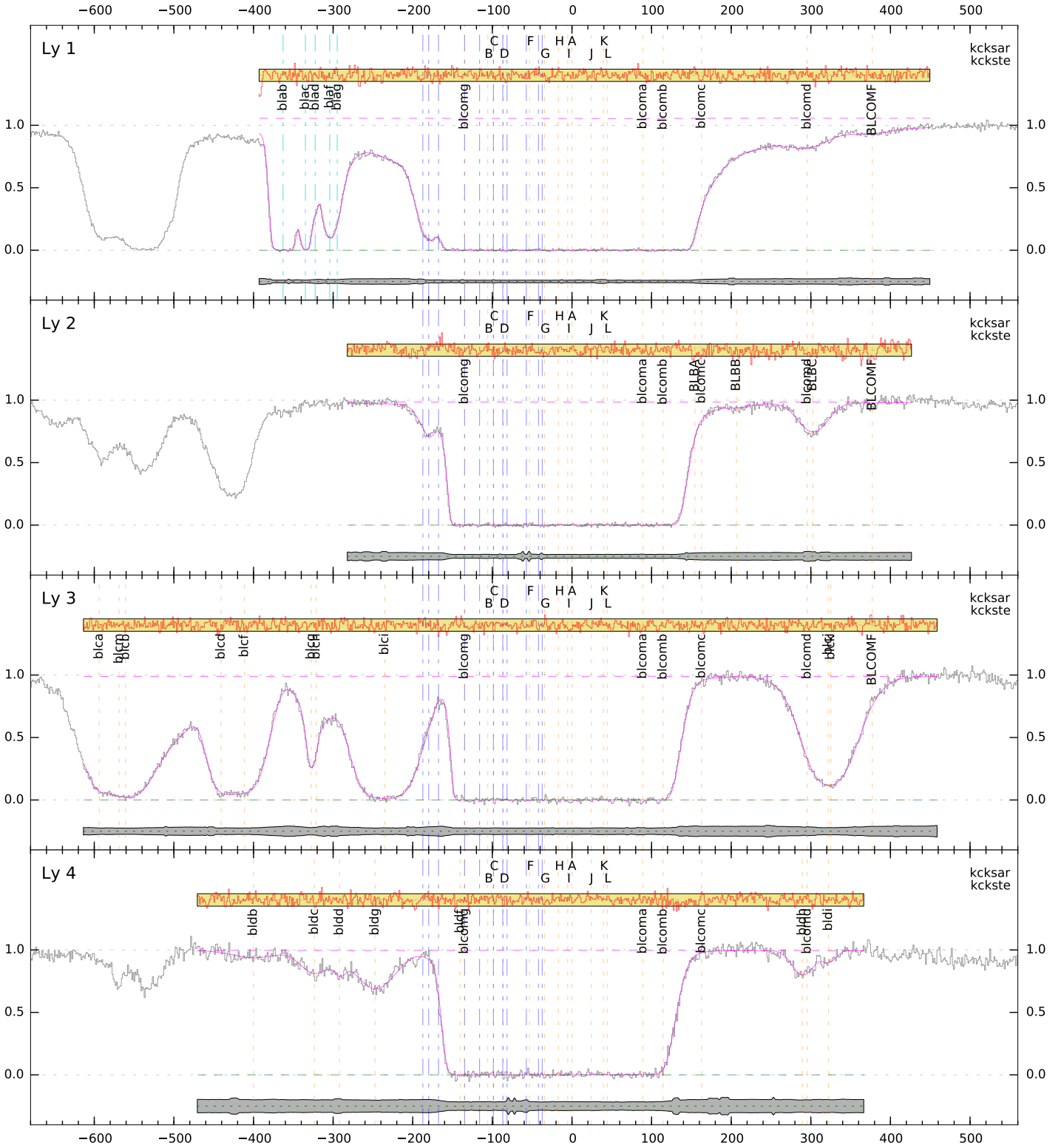
Figure 4.8: The first four of the eight Lyman transitions included in the analysis.
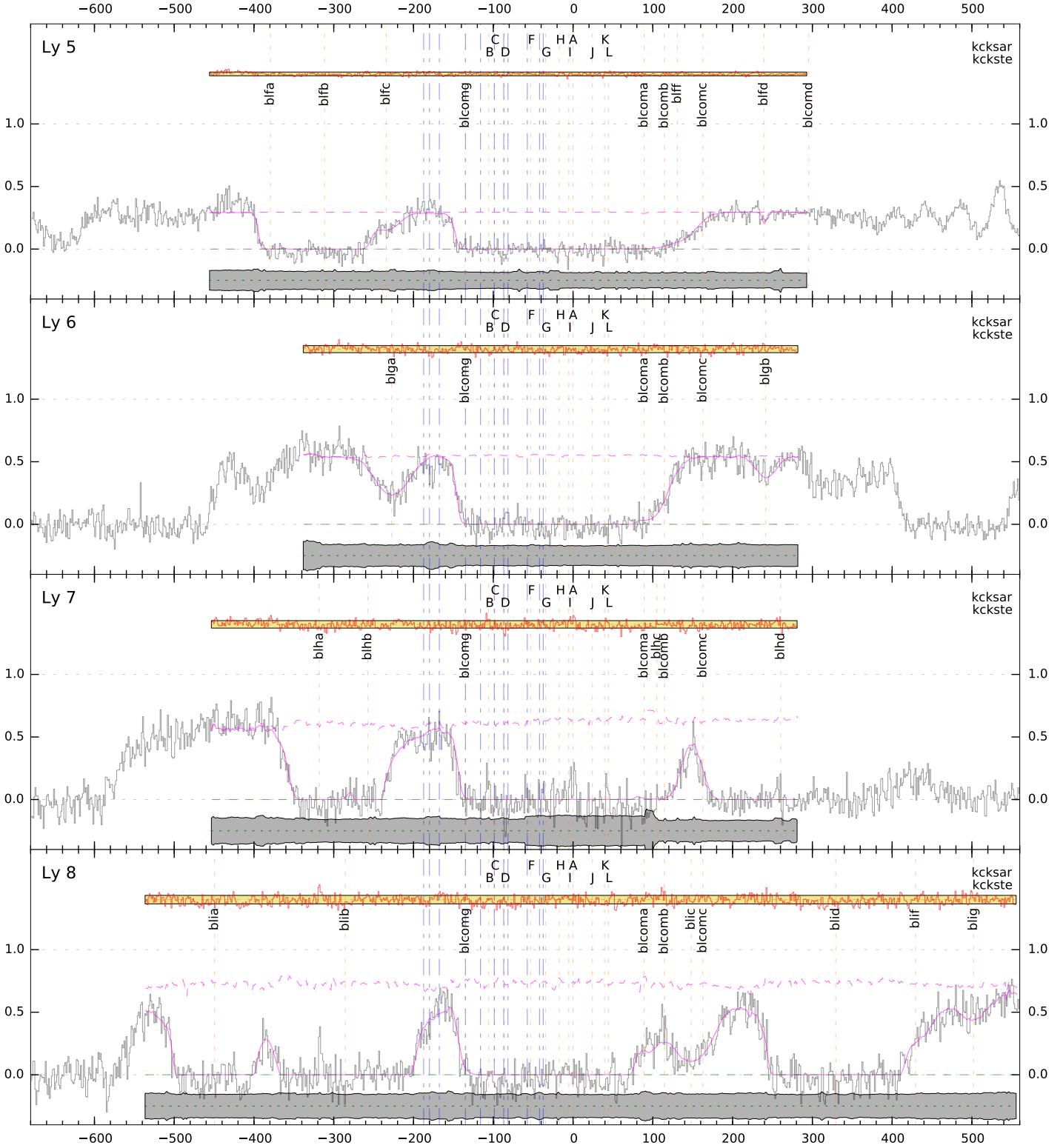
Figure 4.9: The last four of the eight Lyman transitions included in the analysis.
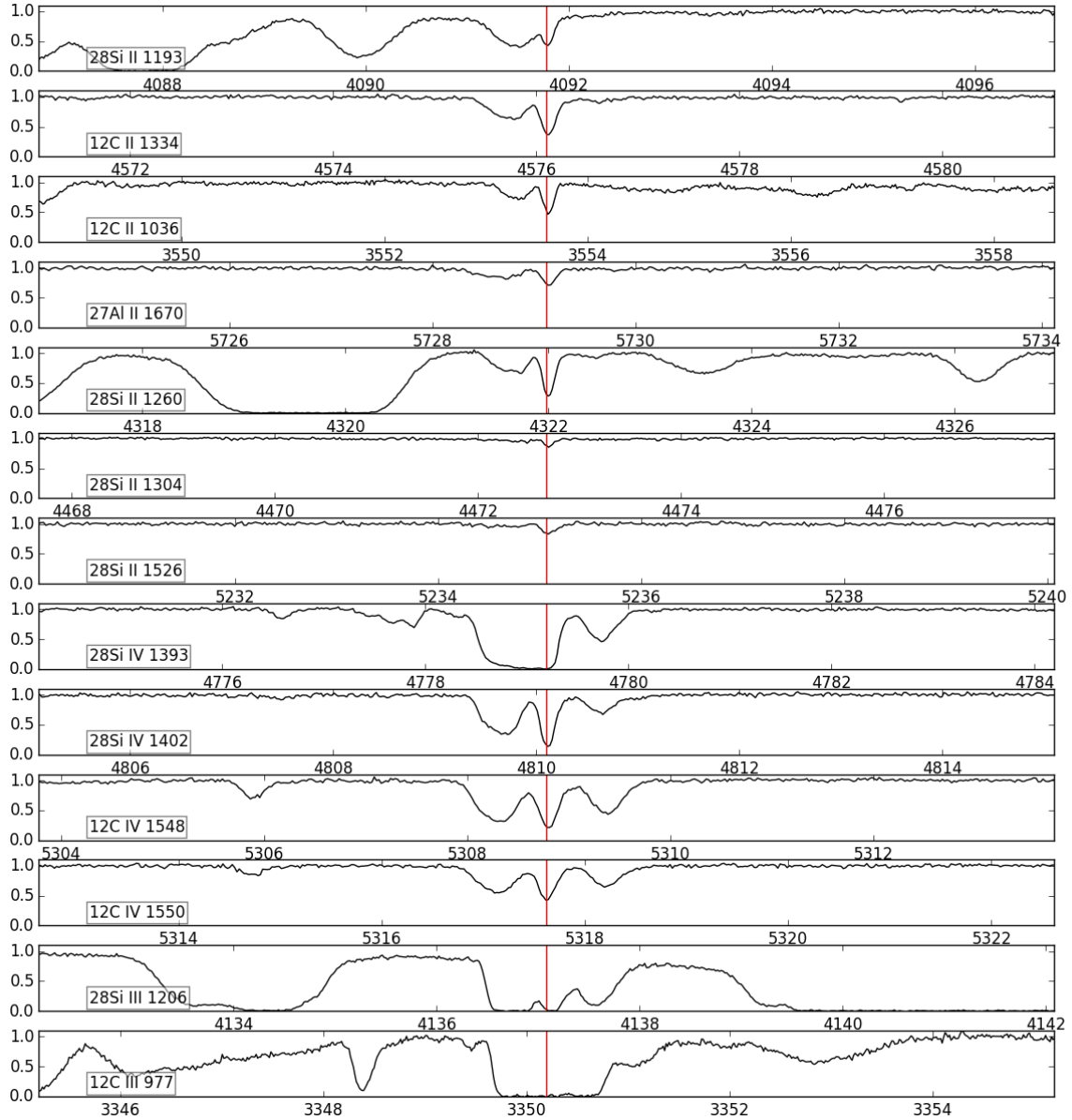
Figure 4.10: Spectra taken from the system towards z = 2.429, for the same transitions that are most prominent in the system of our analysis. Based on this we are able to successfully identify the group of blends in Lyman α as Si III 1206, and we may conclude that the main reason for our problems in arriving at a good model is a major blending with this system.

4.4 Discussion and Outlook

Unfortunately, the line absorption structure of the system at $z = 2.407$ turned out to be a lot more complex than first anticipated. Detecting an absorption system at $z = 2.429$ at a late stage in the process, there was not enough time available to investigate this further. The next step would naturally be to conduct a parallel analysis of the two systems to accurately determine all absorbers that may influence the system at $z = 2.407$, as well as searching for other systems that may produce blending. A solid base model have been produced, but the uncertainty in the column densities of ^1H and ^2H are so high that we are unable to produce a precise estimate of the deuterium abundance at the present time. This high uncertainty is due to a poor determination of the redshifts and dynamic broadening of the different absorbers, as well as the number of absorbers itself. We hope to be able to better determine this when the blending systems have been further analyzed.

Chapter 5

Conclusion

The main focus of this thesis was to get *AlterBBN* up to date, and include generic WIMP candidates to the program. By extending the nuclear network from 88 to 100 reactions and implementing new and updated reaction rates for the six reactions $p(n,\gamma)D$, $D(p,\gamma)^3He$, $D(D,n)^3He$, $D(D,p)^3H$, $^3He(\alpha,\gamma)^7Be$ and $^7Be(n,\alpha)^4He$, we saw in chapter 2.2 that the deuterium yield was reduced by $\sim 4.5\%$, with the uncertainty in the prediction increasing from 1.4% to 2.3%. The prediction of the ^4He abundance was not significantly altered, while the effect on ^3He was only a 0.88% decrease. However, the ^7Li yield saw a major 17.9% increase due to the updates, extending the gap between the predicted and observed value, further disfavoring a nuclear fix to the lithium problem. Strongly linked to the value of the primordial ^7Li abundance, the effect on the ^7Be yield was of a similar size. The significant increase in the uncertainty of the deuterium yield is part due to the extension of the nuclear network (~ 0.16), but most of it arrives from updating the reaction rates. Each and one of the updates do not contribute much, as seen in table 2.4. The new values are reportedly more accurate than previous estimates for the most relevant temperatures for BBN ($\lesssim 2$ MeV), resulting in more precise estimates of the light element abundances. However, the uncertainties in the extrapolation to higher temperatures are obviously higher than in previous measurements. The full nuclear network is a complex system of a large number of inter-dependent reactions, thus small contributions from several sources may arise from updating all six reactions, leading to a significant total increase. This effect is enhanced by the fact that the validity range of the new reactions differ slightly from the old ones.

Nollett & Steigman [48] [25] have previously analyzed the same WIMP candidates as the ones analyzed in chapter 3 here. They found that electromagnetically coupled WIMPs slightly favor $m_\chi \sim 8$ MeV if the WIMP is a Majorana fermion, while the best fit for a neutrino coupled WIMP is $m_\chi \geq 35$ MeV, equivalent to no WIMP at all. In chapter 3.3.1 we used their results to confirm the success of the light WIMP updates to *AlterBBN*, and we saw that the results for a complex scalar is not very different from that of a Majorana fermion. Using the new Planck value of the baryon-to-photon ratio [1] leads to a $\sim 2\%$ reduction in the deuterium yield compared to their work. Due to the extension of the nuclear network and the new reaction rates implemented in *AlterBBN* the deuterium yield is further reduced. This have the effect of shifting the results of Nollett & Steigman towards a better favoring of neutrino coupled WIMPs, lowering the best fit mass for electromagnetically coupled WIMPs. Although no parameter estimations of the best fit WIMP masses have been conducted here, the tendency is evident. However, estimating the parameters is something that have to be done in order to draw any further conclusions.

A constant chemical potential was added to the WIMP candidates in chapter 3.3.2, finding that the parameterized chemical potential must be $\phi_\chi \gtrsim 0.1$ to have any additional effect on the light element abundances compared to the case where ϕ_χ is assumed to be zero. For all types of WIMPs and for both the electromagnetically and neutrino coupling to the standard model particles the effect was to further

enhance the lithium problem, regardless of the value of ϕ_χ. Adding a chemical potential we saw that for a complex scalar, very small masses became increasingly favored with an increasing chemical potential for a neutrino coupled WIMP. For electromagnetically coupled WIMPs, on the other hand, the fits did not seem to improve at all. The next step would naturally be to include the new results in Monte-Carlo chains to find confidence limits on the WIMP masses, allowing for different values of the chemical potential and the number of equivalent neutrinos. This way we would also include the uncertainty on the prediction of the abundances into the considerations.

The task of probing the early universe by analyzing the primordial abundances created during BBN relies heavily on precise measurements of the actual element yields. The simple post-BBN evolution of the deuterium abundance, combined with its large sensitivity to the baryon density, precisely measured through the CMB, makes this element the best probe of BBN. The present status of a measurement of the deuterium abundance in a $z = 2.407$ system towards the quasar *Q1009+2956*, conducted alongside with the update of *AlterBBN*, was discussed in chapter 4. The system has a complex absorption line structure, and the detection of another system at $z = 2.429$ was found to produce several blends in the absorption features, complicating the fitting process. A *PYTHON* program was developed with the purpose of creating composite spectra and models, and acts like an external add-on for the software used in the analysis. By stacking the data from different observations, the error-weighted composite spectra produced by the program simplifies the task of identifying absorption lines. A joint modeling of the two absorption systems is needed to arrive at a precise estimate of the deuterium content in the $z = 2.407$ system, but was out of the scope of this project. However, this is an ongoing process, and we hope to present some results in the near future.

Appendix A

A Short Review of the Theory Behind the Nuclear Reaction Rates

We will now go through a minimum of the theory needed to understand the initialization of the matrix equation built from equation 2.45, which is made in the function *int linearize*. The extension of the nuclear network made it necessary to implement a new type of reaction (see chapter 2.2.3). Here we will derive general formulas for $\Gamma_{ijg \to hkl}$ and $\Gamma_{hkl \to ijg}$ needed for the implementation of equation 2.45, which are valid for any of the reaction types, except for the weak reactions. This discussion is based on the work of Wagoner [43] and Fowler, Caughlan, Zimmerman [98]. The latter also presents an equation that is specific for the case of reactions of the type 2.43. To arrive at a general expression that covers all possible arrangements of 2.44 I have combined information from the two mentioned articles, together with some useful information from Serpico et al. [56] (appendix E). For a broader introduction to the subject of nuclear reactions I recommend the book *Nuclear Physics in Stars* by Iliadis [99].

Many textbooks only consider the general case of two-body reactions,

$$ i + j \longleftrightarrow k + l \,, \tag{A.1} $$

where i and j are the incoming nuclides and k and l are the resulting nuclides (in the case of a photo-ionization process one of the resultants is a photon). In this case the forward reaction rate is defined as

$$ f_{ij \to kl} = \frac{n_i n_j}{(1 + \delta_{ij})} \langle \sigma v \rangle_{ij \to kl} \text{ reactions } cm^{-3} s^{-1} \,, \tag{A.2} $$

where n_i and n_j are the number densities of the reactants, and $\langle \sigma v \rangle_{ij \to kl}$ is the product of the cross section and the velocity, averaged over the appropriately normalized velocity distribution. The factor with the Kronecker delta δ_{ij} covers the possibility that i and j might be the same type of nuclide. To allow for three incoming and/or resulting nuclides we have to extend to the case

$$ i + j + g \longleftrightarrow h + k + l \,. \tag{A.3} $$

It is now convenient to use a terminology where one or more of the reactants/resultants are zero, and instead write the forward reaction rate as

$$ f_{ijg \to hkl} = \frac{n_i^{N_i} n_j^{N_j} n_g^{N_g}}{N_i! N_j! N_g!} \langle \sigma v \rangle_{ijg \to hkl} \,, \tag{A.4} $$

where N_i is the number of nuclides of type i. The reaction rates found in nuclear data catalogs are usually on the form $\hat{f} = \mathcal{N}_A^{N_{in}-1} \langle \sigma v \rangle$ [56], where $N_{in} = N_i + N_j + N_g$ is the total number of incoming

nuclides, and $\mathcal{N}_A = 6.023 \times 10^{23}$ is Avogadro's number. To get the full interaction rate we also have to multiply with $\rho_b^{N_{in}-1}$ [43] [98], resulting in the definition of

$$\Gamma_{ijg \to hkl} \equiv (\rho_b \mathcal{N}_A)^{N_{in}-1} \langle \sigma v \rangle_{ijg \to hkl} \,, \tag{A.5}$$

which goes into equation 2.45. In [99] we find that the forward and reverse rates are defined as (for the simpler case of $i+j \leftrightarrow k+l$)

$$\mathcal{N}_A \langle \sigma v \rangle_{ij \to kl} = \left(\frac{8}{\pi m_{ij}}\right)^{1/2} \frac{\mathcal{N}_A}{(k_B T)^{3/2}} \int_0^\infty E_{ij} \sigma_{ij \to kl} e^{-E_{ij}/k_B T} dE_{ij} \tag{A.6}$$

$$\mathcal{N}_A \langle \sigma v \rangle_{kl \to ij} = \left(\frac{8}{\pi m_{kl}}\right)^{1/2} \frac{\mathcal{N}_A}{(k_B T)^{3/2}} \int_0^\infty E_{kl} \sigma_{kl \to ij} e^{-E_{kl}/k_B T} dE_{kl} \,, \tag{A.7}$$

where m_{ij} is the reduced mass of the i and j nuclide and E_{ij} is the center of mass energy of the forward rate (and conversely for the reverse rate expression). This book also defines the relation between the cross sections of the nuclides to be

$$\frac{\sigma_{kl \to ij}}{\sigma_{ij \to kl}} = \frac{g_i g_j}{g_k g_l} \frac{p_{ij}^2}{p_{kl}^2} \frac{(1 + \delta_{kl})}{(1 + \delta_{ij})} \,, \tag{A.8}$$

where $g_i = (2J_i + 1)$ and J_i is the spin of the appropriate nucleus. p is the "reduced momentum" of the incoming nuclides and is $p = 2mE$ for massive particles and $p = E_\gamma/c^2$ for photons. In the case of three incoming and/or resulting nuclides/photons we may write the relation between the reverse and forward rates as (see both [43] and [98])

$$\frac{\mathcal{N}_A^{N_{out}-1} \langle \sigma v \rangle_{hkl \to ijg}}{\mathcal{N}_A^{N_{in}-1} \langle \sigma v \rangle_{ijg \to hkl}} = \frac{\hat{f}_{hkl}}{\hat{f}_{ijg}} = \mathcal{N}_A^{-N} \left(\frac{N_h! N_k! N_l!}{N_i! N_j! N_g!}\right) \left(\frac{g_i^{N_i} g_j^{N_j} g_g^{N_g}}{g_h^{N_h} g_k^{N_k} g_l^{N_l}}\right) \left(\frac{A_i^{N_i} A_j^{N_j} A_g^{N_g}}{A_h^{N_h} A_k^{N_k} A_l^{N_l}}\right)^{3/2} \times$$

$$\left(\frac{M_u k_B T}{2\pi \hbar^2}\right)^{3N/2} e^{-Q/k_B T} \,, \tag{A.9}$$

where Q is the total energy release of the reaction, N_{out} is the number of outgoing nuclides, and $N = N_i + N_j + N_g - N_h - N_k - N_l = N_{in} - N_{out}$. We define a reverse reaction coefficient, specific for each reaction, as

$$C_{rev} \equiv \left(\frac{N_h! N_k! N_l!}{N_i! N_j! N_g!}\right) \left(\frac{g_i^{N_i} g_j^{N_j} g_g^{N_g}}{g_h^{N_h} g_k^{N_k} g_l^{N_l}}\right) \left(\frac{m_i^{N_i} m_j^{N_j} m_g^{N_g}}{m_h^{N_h} m_k^{N_k} m_l^{N_l} M_u^N}\right)^{3/2} \,, \tag{A.10}$$

where we have used that the atomic mass can be written as $A_i = m_i/M_u$, where $M_u = \mathcal{N}_A^{-1} = 1.66 \cdot 10^{-24}$ g is the atomic mass unit and m_i is the rest mass of nuclide number i. By using equation A.5 we obtain

$$\Gamma_{ijg \to hkl} = \rho_b^{N_{in}-1} \hat{f}_{ijg \to hkl} \tag{A.11}$$

$$\Gamma_{hkl \to ijg} = \rho_b^{N_{out}-1} \hat{f}_{ijg \to hkl} C_{rev} \times 0.987 \cdot 10^{10N} T_9^{3N/2} e^{-11.605 Q_6/T_9} \,, \tag{A.12}$$

where Q_6 is the energy release in MeV. AlterBBN computes the forward rates f in the routine *bbnrate.c*, using tabulated reaction rates $\hat{f}$, while the reverse rates are computed in the function *int linearize* using equation A.12. Note that the reaction rates f computed in *bbnrate.c* are multiplied with $\rho_b^{N_{in}-1}$ in *int linearize* before they are used to calculate the abundance change through $\Gamma_{ijg \to hkl}$ in equation 2.45.

Appendix B

New Reaction Rates and Uncertainties

Six of the reaction rates and their corresponding uncertainties in *AlterBBN* have been updated. Relevant information on the experimental results from [52] $(p(n,\gamma)D)$, [53] $(^7Be(n,\alpha)^4He)$, [54] $(^3He(\alpha,\gamma)^7Be)$ and [55] $(D(p,\gamma)^3He, D(D,n)^3He, D(D,p)^3H)$ is presented below. The reaction number in each caption refers to the number the reaction is given in *AlterBBN* and as listed in table 2.6.

Reaction number 12: $p(n,\gamma)D$

Ando et al. [52] provide best-fit formulas for the reaction rate (in $cm^3 s^{-1} g^{-1}$) and the uncertainty:

$$\hat{f} = 44216.0 \frac{1 + 3.75191 T_9 + 1.92934 T_9^2 + 0.746503 T_9^3 + 0.0197023 T_9^4 + 3.00491 \cdot 10^{-6} T_9^5}{1 + 5.4678 T_9 + 5.62395 T_9^2 + 0.489312 T_9^3 + 0.00747806 T_9^4} \tag{B.1}$$

$$\frac{\delta \hat{f}}{\hat{f}} = 0.00449213 \frac{1 + 3.08947 T_9 + 0.13277 T_9^2 + 1.66472 T_9^3}{1 + 2.75245 T_9 + 1.40958 T_9^2 + 0.8791 T_9^3} . \tag{B.2}$$

Reaction number 19: $^7Be(n,\alpha)^4He$

The experimental results from Hou et al. [53] is summarized in table B.1. The authors provide a best fit formula for the reaction rate, with an error less than 0.4% for temperatures $0.1 - 5$ GK:

$$\hat{f} = \exp(-17.8984 + 0.2711 T_9^{-1} - 23.8918 T_9^{-1/3}$$
$$+ 62.2135 T_9^{1/3} - 5.2888 T_9 + 0.3869 T_9^{5/3} - 22.6197 \ln T_9) . \tag{B.3}$$

The uncertainties are taken from table B.1 since no parametric equation is provided.

Reaction number 27: $^3He(\alpha,\gamma)^7Be$

The best-fit formula of this reaction, given by Cyburt et al. [54], is

$$\hat{f} = \exp(a_0 + a_2 T_9^{-1/3} + a_6 \ln T_9) \frac{\left(1 + n_1 T_9^{2/3} + n_2 T_9^{4/3}\right)}{\left(1 + d_1 T_9^{2/3} + d_2 T_9^{4/3}\right)} , \tag{B.4}$$

where the fit parameters are $a_2 = -12.82707707$, $a_6 = -2/3$, and the rest is given in table B.2. There are different fit parameters corresponding to the central, low and high values, where the latter two are used for the uncertainty calculations.

Reaction number 20, 28 and 29: $D(p,\gamma)^3He$, $D(D,n)^3He$ and $D(D,p)^3H$

No parametric equations are presently available for the three new rates from Coc et al. [55]. However, the reaction rates and their corresponding uncertainties are implemented according to the tabulated experimental results from the paper, which are presented in table B.3.

T (GK)	Present	Wagoner	Ratio
0.1	$(9.6 \pm 8.3) \cdot 10^5$	$7.7 \cdot 10^6$	0.13
0.2	$(1.7 \pm 1.3) \cdot 10^6$	$1.5 \cdot 10^7$	0.11
0.3	$(2.3 \pm 1.7) \cdot 10^6$	$2.3 \cdot 10^7$	0.10
0.4	$(2.9 \pm 2.0) \cdot 10^6$	$3.1 \cdot 10^7$	0.09
0.5	$(3.5 \pm 2.2) \cdot 10^6$	$3.9 \cdot 10^7$	0.09
0.6	$(4.2 \pm 2.4) \cdot 10^6$	$4.6 \cdot 10^7$	0.09
0.7	$(4.9 \pm 2.6) \cdot 10^6$	$5.4 \cdot 10^7$	0.09
0.8	$(5.6 \pm 2.8) \cdot 10^6$	$6.2 \cdot 10^7$	0.09
0.9	$(6.4 \pm 2.9) \cdot 10^6$	$6.9 \cdot 10^7$	0.09
1.0	$(7.2 \pm 3.1) \cdot 10^6$	$7.7 \cdot 10^7$	0.09
1.5	$(1.2 \pm 0.7) \cdot 10^7$	$1.2 \cdot 10^8$	0.10
2.0	$(1.7 \pm 0.4) \cdot 10^7$	$1.5 \cdot 10^8$	0.11
2.5	$(2.1 \pm 0.4) \cdot 10^7$	$1.9 \cdot 10^8$	0.11
3.0	$(2.5 \pm 0.5) \cdot 10^7$	$2.3 \cdot 10^8$	0.11
3.5	$(2.9 \pm 0.5) \cdot 10^7$	$2.7 \cdot 10^8$	0.11
4.0	$(3.2 \pm 0.5) \cdot 10^7$	$3.1 \cdot 10^8$	0.10
4.5	$(3.4 \pm 0.5) \cdot 10^7$	$3.5 \cdot 10^8$	0.10
5.0	$(3.5 \pm 0.5) \cdot 10^7$	$3.9 \cdot 10^8$	0.09

Table B.1: Copy of table II in ref. [53], showing the new rate with uncertainties for temperatures ranging from 0.1 to 5.0 GK. They are compared with the old rate from Wagoner [43], and the fourth column shows the ratio between the two.

Parameter	Low	Central	High
a_0	15.531721	15.609867	15.679639
n_1	-0.100208	-0.020178	0.037757
n_2	0.235187	0.211995	0.196645
d_1	0.114322	0.255059	0.353050
d_2	0.373802	0.338573	0.316019

Table B.2: Fit parameters for reaction number 27, $^3He(\alpha, \gamma)^7Be$ from ref. [54].

T (GK)	$D(p,\gamma)^3He$ reac. rate	f.u	$D(D,n)^3He$ reac. rate	f.u	$D(D,p)^3H$ reac. rate	f.u	T (GK)	$D(p,\gamma)^3He$ reac. rate	f.u	$D(D,n)^3He$ reac. rate	f.u	$D(D,p)^3H$ reac. rate	f.u
0.001	$4.815 \cdot 10^{-14}$	1.038	$1.142 \cdot 10^{-8}$	1.011	$1.173 \cdot 10^{-8}$	1.011	0.140	$1.224 \cdot 10^{1}$	1.038	$5.631 \cdot 10^{5}$	1.011	$5.304 \cdot 10^{5}$	1.011
0.002	$6.409 \cdot 10^{-9}$	1.038	$5.470 \cdot 10^{-5}$	1.011	$5.609 \cdot 10^{-5}$	1.011	0.150	$1.420 \cdot 10^{1}$	1.038	$6.568 \cdot 10^{5}$	1.011	$6.165 \cdot 10^{5}$	1.011
0.003	$4.525 \cdot 10^{-7}$	1.038	$3.021 \cdot 10^{-3}$	1.011	$3.092 \cdot 10^{-3}$	1.011	0.160	$1.628 \cdot 10^{1}$	1.038	$7.559 \cdot 10^{5}$	1.011	$7.072 \cdot 10^{5}$	1.011
0.004	$4.896 \cdot 10^{-6}$	1.038	$3.732 \cdot 10^{-2}$	1.011	$3.814 \cdot 10^{-2}$	1.011	0.180	$2.076 \cdot 10^{1}$	1.038	$9.691 \cdot 10^{5}$	1.011	$9.011 \cdot 10^{5}$	1.011
0.005	$2.444 \cdot 10^{-5}$	1.038	$2.212 \cdot 10^{-1}$	1.011	$2.257 \cdot 10^{-1}$	1.011	0.200	$2.565 \cdot 10^{1}$	1.038	$1.200 \cdot 10^{6}$	1.011	$1.110 \cdot 10^{6}$	1.011
0.006	$8.086 \cdot 10^{-5}$	1.038	$8.546 \cdot 10^{-1}$	1.011	$8.707 \cdot 10^{-1}$	1.011	0.250	$3.941 \cdot 10^{1}$	1.038	$1.842 \cdot 10^{6}$	1.011	$1.682 \cdot 10^{6}$	1.011
0.007	$2.078 \cdot 10^{-4}$	1.038	$2.505 \cdot 10^{0}$	1.011	$2.549 \cdot 10^{0}$	1.011	0.300	$5.505 \cdot 10^{1}$	1.038	$2.555 \cdot 10^{6}$	1.011	$2.309 \cdot 10^{6}$	1.011
0.008	$4.499 \cdot 10^{-4}$	1.038	$6.066 \cdot 10^{0}$	1.011	$6.164 \cdot 10^{0}$	1.011	0.350	$7.225 \cdot 10^{1}$	1.038	$3.318 \cdot 10^{6}$	1.011	$2.974 \cdot 10^{6}$	1.011
0.009	$8.619 \cdot 10^{-4}$	1.038	$1.278 \cdot 10^{1}$	1.011	$1.297 \cdot 10^{1}$	1.011	0.400	$9.076 \cdot 10^{1}$	1.038	$4.119 \cdot 10^{6}$	1.011	$3.663 \cdot 10^{6}$	1.011
0.010	$1.506 \cdot 10^{-3}$	1.038	$2.424 \cdot 10^{1}$	1.011	$2.458 \cdot 10^{1}$	1.011	0.450	$1.104 \cdot 10^{2}$	1.038	$4.946 \cdot 10^{6}$	1.011	$4.371 \cdot 10^{6}$	1.011
0.011	$2.450 \cdot 10^{-3}$	1.038	$4.237 \cdot 10^{1}$	1.011	$4.290 \cdot 10^{1}$	1.011	0.500	$1.310 \cdot 10^{2}$	1.038	$5.792 \cdot 10^{6}$	1.011	$5.089 \cdot 10^{6}$	1.011
0.012	$3.767 \cdot 10^{-3}$	1.038	$6.936 \cdot 10^{1}$	1.011	$7.016 \cdot 10^{1}$	1.011	0.600	$1.748 \cdot 10^{2}$	1.038	$7.517 \cdot 10^{6}$	1.011	$6.543 \cdot 10^{6}$	1.011
0.013	$5.531 \cdot 10^{-3}$	1.038	$1.077 \cdot 10^{2}$	1.011	$1.088 \cdot 10^{2}$	1.011	0.700	$2.212 \cdot 10^{2}$	1.038	$9.260 \cdot 10^{6}$	1.011	$8.001 \cdot 10^{6}$	1.011
0.014	$7.816 \cdot 10^{-3}$	1.038	$1.600 \cdot 10^{2}$	1.011	$1.615 \cdot 10^{2}$	1.011	0.800	$2.700 \cdot 10^{2}$	1.038	$1.100 \cdot 10^{7}$	1.011	$9.448 \cdot 10^{6}$	1.011
0.015	$1.070 \cdot 10^{-2}$	1.038	$2.291 \cdot 10^{2}$	1.011	$2.310 \cdot 10^{2}$	1.011	0.900	$3.207 \cdot 10^{2}$	1.038	$1.272 \cdot 10^{7}$	1.011	$1.087 \cdot 10^{7}$	1.011
0.016	$1.425 \cdot 10^{-2}$	1.038	$3.179 \cdot 10^{2}$	1.011	$3.202 \cdot 10^{2}$	1.011	1.000	$3.729 \cdot 10^{2}$	1.038	$1.442 \cdot 10^{7}$	1.011	$1.228 \cdot 10^{7}$	1.011
0.018	$2.366 \cdot 10^{-2}$	1.038	$5.667 \cdot 10^{2}$	1.011	$5.698 \cdot 10^{2}$	1.011	1.250	$5.093 \cdot 10^{2}$	1.038	$1.850 \cdot 10^{7}$	1.011	$1.565 \cdot 10^{7}$	1.011
0.020	$3.659 \cdot 10^{-2}$	1.038	$9.310 \cdot 10^{2}$	1.011	$9.343 \cdot 10^{2}$	1.011	1.500	$6.522 \cdot 10^{2}$	1.038	$2.235 \cdot 10^{7}$	1.011	$1.882 \cdot 10^{7}$	1.011
0.025	$8.753 \cdot 10^{-2}$	1.038	$2.504 \cdot 10^{3}$	1.011	$2.502 \cdot 10^{3}$	1.011	1.750	$8.000 \cdot 10^{2}$	1.038	$2.595 \cdot 10^{7}$	1.012	$2.181 \cdot 10^{7}$	1.012
0.030	$1.701 \cdot 10^{-1}$	1.038	$5.301 \cdot 10^{3}$	1.011	$5.276 \cdot 10^{3}$	1.011	2.000	$9.517 \cdot 10^{2}$	1.038	$2.932 \cdot 10^{7}$	1.012	$2.461 \cdot 10^{7}$	1.012
0.040	$4.476 \cdot 10^{-1}$	1.038	$1.568 \cdot 10^{4}$	1.011	$1.549 \cdot 10^{4}$	1.011	2.500	$1.265 \cdot 10^{3}$	1.038	$3.546 \cdot 10^{7}$	1.013	$2.976 \cdot 10^{7}$	1.013
0.050	$8.915 \cdot 10^{-1}$	1.038	$3.369 \cdot 10^{4}$	1.011	$3.307 \cdot 10^{4}$	1.011	3.000	$1.587 \cdot 10^{3}$	1.038	$4.093 \cdot 10^{7}$	1.014	$3.440 \cdot 10^{7}$	1.014
0.060	$1.510 \cdot 10^{0}$	1.038	$6.013 \cdot 10^{4}$	1.011	$5.868 \cdot 10^{4}$	1.011	3.500	$1.914 \cdot 10^{3}$	1.038	$4.585 \cdot 10^{7}$	1.014	$3.863 \cdot 10^{7}$	1.014
0.070	$2.302 \cdot 10^{0}$	1.038	$9.527 \cdot 10^{4}$	1.011	$9.246 \cdot 10^{4}$	1.011	4.000	$2.244 \cdot 10^{3}$	1.039	$5.031 \cdot 10^{7}$	1.015	$4.251 \cdot 10^{7}$	1.015
0.080	$3.265 \cdot 10^{0}$	1.038	$1.390 \cdot 10^{5}$	1.011	$1.343 \cdot 10^{5}$	1.011	5.000	$2.905 \cdot 10^{3}$	1.040	$5.816 \cdot 10^{7}$	1.016	$4.946 \cdot 10^{7}$	1.016
0.090	$4.392 \cdot 10^{0}$	1.038	$1.912 \cdot 10^{5}$	1.011	$1.837 \cdot 10^{5}$	1.011	6.000	$3.557 \cdot 10^{3}$	1.042	$6.488 \cdot 10^{7}$	1.017	$5.552 \cdot 10^{7}$	1.017
0.100	$5.676 \cdot 10^{0}$	1.038	$2.513 \cdot 10^{5}$	1.011	$2.404 \cdot 10^{5}$	1.011	7.000	$4.194 \cdot 10^{3}$	1.044	$7.072 \cdot 10^{7}$	1.018	$6.077 \cdot 10^{7}$	1.018
0.110	$7.109 \cdot 10^{0}$	1.038	$3.190 \cdot 10^{5}$	1.011	$3.039 \cdot 10^{5}$	1.011	8.000	$4.812 \cdot 10^{3}$	1.046	$7.583 \cdot 10^{7}$	1.018	$6.529 \cdot 10^{7}$	1.018
0.120	$8.685 \cdot 10^{0}$	1.038	$3.938 \cdot 10^{5}$	1.011	$3.737 \cdot 10^{5}$	1.011	9.000	$5.410 \cdot 10^{3}$	1.047	$8.037 \cdot 10^{7}$	1.018	$6.912 \cdot 10^{7}$	1.018
0.130	$1.040 \cdot 10^{1}$	1.038	$4.753 \cdot 10^{5}$	1.011	$4.493 \cdot 10^{5}$	1.011	10.000	$5.988 \cdot 10^{3}$	1.049	$8.437 \cdot 10^{7}$	1.018	$7.228 \cdot 10^{7}$	1.019

Table B.3: Copy of table XII in ref. [55], showing the new rates and the corresponding uncertainties on rate 20 $(D(p,\gamma)^3He)$, 28 $(D(D,n)^3He)$ and 29 $(D(D,p)^3H)$. Note that the uncertainties are given as the log-normal distributed error f.u

Appendix C

Accurate Expressions for the Number Density, Energy Density and Pressure of WIMPs

The derivation of equations 2.17, 2.18 and 2.23 from equations 1.15 - 1.17 is not documented in the *AlterBBN* manual, nor in the description of the Wagoner or Kawano codes. In his book "An Introduction To The Study Of Stellar Structures", S. Chandrasekhar [100] derives the distribution functions for electrons and positrons in terms of the modified Bessel functions (chapter 5). The implementation of WIMPs in the *AlterBBN* code requires the distribution functions also for massive bosons, since we explicitly look at real and complex scalar candidates. In the following I will derive these expressions, motivated by the method of Chandrasekhar. For completeness, I will also derive the general expressions for fermions, which is needed to include the fermionic WIMPs.

The motion of a particle through spacetime may be described by hyperbolic coordinates in a spacetime (Minkowski) diagram, as described by Einstein's special theory of relativity. In these terms, the Lorentz factor $\gamma = 1/\sqrt{1 - (u/c)^2}$, where $\mathbf{u}$ is the velocity of the particle, is parameterized as

$$\gamma = \cosh \theta \, , \tag{C.1}$$

where θ is the rapidity, defined as the hyperbolic angle in the Lorentz transformation expressions. Squaring the momentum 3-vector $\mathbf{p} = \gamma m \mathbf{u}$, where m is the rest mass of the particle, solving for $(u/c)^2$ and substituting into the Lorentz factor yields

$$\frac{p}{mc} = \sqrt{\gamma^2 - 1} = \sqrt{\cosh^2 \theta - 1} = \sinh \theta \, . \tag{C.2}$$

The energy-momentum relation reads

$$E^2 = (pc)^2 + (mc^2)^2 \, , \tag{C.3}$$

and inserting C.2 we can express the total energy in terms of hyperbolic coordinates as

$$E = mc^2 \cosh \theta \, . \tag{C.4}$$

Noting that the derivatives become

$$dp = mc \cosh \theta d\theta \tag{C.5}$$

and

$$EdE = pc^2 dp = (mc^2)^2 \sinh \theta \cosh \theta d\theta \, , \tag{C.6}$$

and using the earlier established relations $z \equiv mc^2/k_B T$ and $\phi \equiv \mu/k_B T$, we are now equipped to write the distribution functions of a particle in a more convenient way:

$$n = A \int_{mc^2}^{\infty} \frac{(E^2 - m^2 c^4)^{1/2} E dE}{\exp\left[(E - \mu)/(k_B T)\right] \pm 1} = A(mc^2)^3 \int_0^{\infty} \frac{\sinh^2 \theta \cosh \theta d\theta}{\exp\left[z \cosh \theta - \phi\right] \pm 1} \tag{C.7}$$

$$\rho c^2 = A \int_{mc^2}^{\infty} \frac{(E^2 - m^2 c^4)^{1/2} E^2 dE}{\exp\left[(E - \mu)/(k_B T)\right] \pm 1} = A(mc^2)^4 \int_0^{\infty} \frac{\sinh^2 \theta \cosh^2 \theta d\theta}{\exp\left[z \cosh \theta - \phi\right] \pm 1} \tag{C.8}$$

$$P = \frac{A}{3} \int_{mc^2}^{\infty} \frac{(E^2 - m^2 c^4)^{3/2} dE}{\exp\left[(E - \mu)/(k_B T)\right] \pm 1} = \frac{A}{3}(mc^2)^4 \int_0^{\infty} \frac{\sinh^4 \theta d\theta}{\exp\left[z \cosh \theta - \phi\right] \pm 1} \tag{C.9}$$

Here $A = g/2\pi^2(\hbar c)^3$, and to proceed further it is convenient to expand the denominator in series of $e^{-z \cosh \theta + \phi}$. We thus have to distinguish between fermions and bosons.

For **fermions** we have to expand the expression $(e^{z \cosh \theta - \phi} + 1)^{-1}$ in an infinite series. Choosing $x = e^{-z \cosh \theta + \phi}$, the easiest procedure is to first expand $f(x) = (x + 1)^{-1}$, which results in

$$f(x) \approx 1 - x + x^2 - x^3 + O(x^4) \,. \tag{C.10}$$

We then transform back to our original expression by multiplying $f(x)$ by x, that is

$$
\begin{aligned}
\frac{1}{e^{z \cosh \theta - \phi} + 1} &= x f(x) \\
&\approx x - x^2 + x^3 - x^4 + O(x^5) \\
&= \sum_{n=1}^{\infty} (-1)^{n+1} e^{n\phi} e^{-nz \cosh \theta} \,.
\end{aligned}
\tag{C.11}
$$

For **bosons** the procedure is identical, only now we expand the expression $(e^{z \cosh \theta - \phi} - 1)^{-1}$. Multiplying the result this time with $-x$, we finally arrive at

$$\frac{1}{e^{z \cosh \theta - \phi} - 1} = \sum_{n=1}^{\infty} e^{n\phi} e^{-nz \cosh \theta} \,. \tag{C.12}$$

These series expansions are the part that separates fermions from bosons in the final expressions for their various distribution functions, and we see that the only difference is the factor $(-1)^{n+1}$ in the sum.

The time has come to introduce the modified Bessel functions of type two, which are defined as

$$K_\alpha(z) = \int_0^{\infty} e^{-z \cosh \theta} \cosh \alpha \theta \, d\theta \,. \tag{C.13}$$

We can now use the relations

$$\sinh^2 \theta \cosh \theta = \frac{1}{4}(\cosh 3\theta - \cosh \theta) \tag{C.14}$$

$$\sinh^2 \theta \cosh^2 \theta = \frac{1}{8}(\cosh 4\theta - 1) \tag{C.15}$$

to write the distribution functions for the number density and the energy density as

$$n = A(mc^2)^3 \sum_{n=1}^{\infty} (-1)^{\beta(n+1)} e^{n\phi} \int_0^{\infty} e^{-nz\cosh\theta} \left[\frac{1}{4} (K_3(nz) - K_1(nz)) \right] d\theta$$

$$= A(mc^2)^3 \sum_{n=1}^{\infty} (-1)^{\beta(n+1)} e^{n\phi} \left[\frac{1}{4} (K_3(nz) - K_1(nz)) \right]$$

$$\rho c^2 = A(mc^2)^4 \sum_{n=1}^{\infty} (-1)^{\beta(n+1)} e^{n\phi} \int_0^{\infty} e^{-nz\cosh\theta} \left[\frac{1}{8} (\cosh 4\theta - 1) \right] d\theta \tag{C.16}$$

$$= A(mc^2)^4 \sum_{n=1}^{\infty} (-1)^{\beta(n+1)} e^{n\phi} \left[\frac{1}{8} (\cosh 4\theta - 1) \right] , \tag{C.17}$$

where β distinguishes between fermions ($\beta = 1$) and bosons ($\beta = 0$). Finding the pressure distribution requires a bit more involved analysis, since we can not simply write $\sinh^4 \theta$ only in terms of $\cosh \alpha\theta$. The trick is to perform integration by parts, by first doing a change of variables through $x = \cosh\theta$, giving us

$$\int_0^{\infty} e^{-nz\cosh\theta} \sinh^4 \theta \, d\theta = \int_1^{\infty} e^{-nzx} (x^2 - 1)^{3/2} \, dx , \tag{C.18}$$

remembering that $\sinh^2 \theta = \cosh^2 \theta - 1$, and using that $\cosh 0 = 1$ and $\lim_{\theta\to\infty} \cosh\theta \to \infty$. Using integration by parts, defining

$$u = (x^2 - 1)^{3/2} \to du = 3(x^2 - 1)^{1/2} x \, dx, \qquad dv = e^{-nzx} \to v = -\frac{1}{nz} e^{-nzx} ,$$

we find that

$$\int_1^{\infty} e^{-nzx} (x^2 - 1)^{3/2} \, dx = -\frac{1}{nz} e^{-nzx} (x^2 - 1)^{3/2} \Big|_{x=1}^{\infty} + \frac{3}{nz} \int_1^{\infty} e^{-nzx} (x^2 - 1)^{1/2} x \, dx . \tag{C.19}$$

Evaluation of the lower and upper boundary in the first part yields 0, while substituting back to the variable θ in the last part results in the expression having the desired form. Thus we have showed that we can write

$$\int_0^{\infty} e^{-nz\cosh\theta} \sinh^4 \theta \, d\theta = \frac{3}{nz} \int_0^{\infty} e^{-nz\cosh\theta} \sinh^2 \theta \cosh\theta \, d\theta . \tag{C.20}$$

Now we can apply relation C.15 to get the expression of the pressure density on the form

$$P = A(mc^2)^4 \sum_{n=1}^{\infty} \frac{(-1)^{\beta(n+1)}}{nz} e^{n\phi} \int_0^{\infty} e^{-nz\cosh\theta} \left[\frac{1}{4} (\cosh 3\theta - \cosh\theta) \right] d\theta$$

$$= A(mc^2)^4 \sum_{n=1}^{\infty} \frac{(-1)^{\beta(n+1)}}{nz} e^{n\phi} \left[\frac{1}{4} (K_3(nz) - K_1(nz)) \right] , \tag{C.21}$$

The different Bessel functions (different orders) are related though the recurrence formula

$$K_{\alpha+1}(z) - K_{\alpha-1}(z) = \frac{2\alpha}{z} K_\alpha . \tag{C.22}$$

Thus

$$K_3(nz) - K_1(nz) = \frac{4}{nz} K_2 , \tag{C.23}$$

and by also finding $K_4(nz) - K_2(nz)$ and $K_2(nz) - K_0(nz)$ we are able to show that

$$K_4(nz) - K_0(nz) = \frac{2}{nz} [3K_3(nz) + K_1(nz)] . \tag{C.24}$$

Using these results, together with the earlier defined relations of equation 2.16, we arrive at the final expressions for the number density, energy density and pressure distributions for fermions and bosons:

$$n = \frac{g}{2\pi^2} \left[\frac{mc^2}{\hbar c}\right]^3 \sum_{n=1}^{\infty} (-1)^{\beta(n+1)} e^{n\phi} L(nz) \tag{C.25}$$

$$\rho c^2 = \frac{g}{2\pi^2} \frac{(mc^2)^4}{(\hbar c)^3} \sum_{n=1}^{\infty} (-1)^{\beta(n+1)} e^{n\phi} M(nz) \tag{C.26}$$

$$P = \frac{g}{2\pi^2} \frac{(mc^2)^4}{(\hbar c)^3} \sum_{n=1}^{\infty} \frac{(-1)^{\beta(n+1)}}{nz} e^{n\phi} L(nz) \tag{C.27}$$

These are general expressions for both fermions and bosons, where

$$\beta = \begin{cases} 0 & \text{for bosons} \\ 1 & \text{for fermions} \end{cases}$$

We now see where the expressions for the sum of electron and positron energy density and pressure (equations 2.17 and 2.18) and the difference in the electron and positron number density (equation 2.23) come from. Recalling that the electron and positron chemical potentials are related through $\phi_{e^-} = -\phi_{e^+}$, and using the hyperbolic relations

$$\sinh x = \frac{e^x - e^{-x}}{2}, \qquad \cosh x = \frac{e^x + e^{-x}}{2}, \tag{C.28}$$

it is straight forward to obtain these expressions.

In the presence of a light WIMP we also need the derivative of the energy density with respect to the temperature (see chapter 3.2). In the absence of a chemical potential for the WIMPs the only dependence on the temperature in equation C.26 is through z, and the calculation amounts to finding the derivative of $M(nz)$ with respect to T_9. However, we will allow for a non-zero chemical potential, which means that also ϕ_χ is dependent on T_9. For the derivative of the $e^\pm$ energy density this contribution has been neglected (by the author of *AlterBBN*), on the basis of the assumption of a small ϕ_e throughout the analysis. However, this is not entirely true, evident from figure 2.1. Moreover, since there are no constraints on a hypothetical WIMP degeneracy we will include this term in the derivative of the WIMP energy density. The WIMP degeneracy parameter $\phi_\chi \equiv \mu_\chi / k_B T_9$ is a unit-less parameterization of the WIMP chemical potential, similar to the definition of ϕ_e, which leaves the process of finding the derivative of the exponential in equation C.26 a straight forward one. By the definition of $M(z)$ in equations 2.16 we find that

$$\frac{d}{dT_9} M(nz) = \frac{dz}{dT_9} \frac{d}{dz} \left[\frac{1}{nz} \left(\frac{3}{4} K_3(nz) + \frac{1}{4} K_1(nz) \right) \right]$$
$$= -\frac{z}{T_9} \left\{ -\frac{1}{nz^2} \left[\frac{3}{4} K_3(nz) + \frac{1}{4} K_1(nz) \right] + \frac{1}{nz} \left[\frac{3}{4} \frac{d}{dz} K_3(nz) + \frac{1}{4} \frac{d}{dz} K_1(nz) \right] \right\}. \tag{C.29}$$

Differentiating equation C.13 for $\alpha = 1$ and 3, and inserting in the above equation we get

$$\frac{d}{dT_9} M(nz) = \frac{1}{nzT_9} \left[\frac{3}{4} K_3(nz) + \frac{1}{4} K_1(nz) \right]$$
$$+ \frac{1}{T_9} \left[\frac{3}{8} K_4(nz) - \frac{3}{8} K_0(nz) \right] + \frac{1}{T_9} \left[\frac{1}{2} K_2(nz) + \frac{1}{2} K_0(nz) \right], \tag{C.30}$$

and using equation C.22 we finally arrive at

$$\frac{d}{dT_9} M(nz) = \frac{1}{T_9} \left[\frac{1}{2} K_4(nz) + \frac{1}{2} K_2(nz) \right] = \frac{z}{T_9} nN(nz). \tag{C.31}$$

The full expression thus becomes

$$\frac{d}{dT_9}\rho c^2 = \frac{g}{2\pi^2}\frac{(mc^2)^4}{(\hbar c)^3}\frac{1}{T_9}\sum_{n=1}^{\infty}(-1)^{\beta(n+1)}ne^{n\phi}\left[zN(nz) - \phi_\chi M(nz)\right] . \qquad (C.32)$$

Bibliography

[1] Planck Collaboration. "Planck 2015 results XIII. Cosmological parameters". In: *ArXiv e-prints* (2015). arXiv: 1502.01589.

[2] R. Cooke. *ALIS Code*. Documentation not published yet. Incomplete version available upon request. 2015. URL: https://github.com/jbwhit/project-alis.

[3] A. A. Penzias and R. W. Wilson. In: *Astrophys. J.* 142 (1965), p. 419. DOI: 10.1086/148307.

[4] R. H. Dicke et al. In: *Astrophys. J.* 142 (1965), p. 414. DOI: 10.1086/148306.

[5] Planck Collaboration. "Planck 2015 results I. Overview of products and scientific results". In: *ArXiv e-prints* (2015). arXiv: 1502.01582.

[6] D. J. Eisenstein et al. "SDSS-III: Massive Spectroscopic Surveys of the Distant Universe, the Milky Way, and Extra-Solar Planetary Systems". In: *The Astronomical Journal* 142 (2011), p. 72. arXiv: 1101.1529.

[7] G. Lemson and the Virgo Consortium. In: *ArXiv e-prints* (2006). arXiv: astro-ph/0608019.

[8] G. Steigman. "Primordial Nucleosynthesis in the Precision Cosmology Era". In: *Ann. Rev. Nucl. Part. Sci.* 57.1 (2007), p. 463. arXiv: 0712.1100.

[9] L. Canetti, M. Drewes, and M. Shaposhnikov. In: *New Journal of Physics* 14 (2012), p. 095012. arXiv: 1204.4186.

[10] ATLAS Collaboration. In: *Phys. Lett. B.* 716 (2012), p. 1.

[11] LHCb Collaboration. In: *ArXiv e-prints* (2015). arXiv: 1507.03414.

[12] K. A. Olive et al. (Particle Data Group). "The Review of Particle Physics". In: *Chin. Phys. C* 38 (2014), p. 090001. URL: http://pdg.lbl.gov/ (visited on 05/11/2015).

[13] Y. et al. Fukuda. In: *Phys. Rev. Lett.* 81 (1998), p. 1158.

[14] S. Riemer-Sørensen, D. Parkinson, and T. M. Davis. In: *Publications of the Astronomical Society of Australia* 30 (2013). arXiv: 1301.7102.

[15] K. Land and J. Magueijo. In: *Phys. Rev. Lett.* 95 (2005), p. 071301. arXiv: astro-ph/0502237.

[16] E. W. Kolb and M. S. Turner. *The Early Universe*. 1990.

[17] S. M. O'Raifeartaigh. In: (2015). arXiv: 1506.01651.

[18] S. et al. Perlmutter. In: *Astrophys. J.* 517 (1999), p. 565. arXiv: astro-ph/9812133.

[19] S. M. Carroll. "Lecture Notes on General Relativity". In: (1997). arXiv: gr-qc/9712019.

[20] G. Steigman. "Neutrinos and Big Bang Nucleosynthesis". In: *Adv. in High En. Phys.* 2012 (2012). arXiv: 1208.0032.

[21] R.H. Cyburt et al. "Big Bang Nucleosynthesis: 2015". In: *ArXiv e-prints* (2015). arXiv: 1505.01076.

[22] F. E. Wietfeldt and G. L. Green. "Colloquium: The neutron lifetime". In: *Rev. Mod. Phys* 83 (2011), p. 1173.

[23] G. Steigman. In: *Phys. Rev. D* 48 (2013), p. 103517. arXiv: 1303.0049.

[24] S. Hannestad. In: *Phys. Rev. D* 65 (2002), p. 083006. arXiv: astro-ph/0111423.

[25] K. M. Nollett and G. Steigman. In: *Phys. Rev. D* 91 (2015), p. 083505. arXiv: 1411.6005.

[26] K.M. Nollet and S. Burles. In: *Phys. Rev. D* 61 (2000), p. 1.

[27] M. Archidiacono, E. Calabrese, and A. Melchiorri. In: *Phys. Rev. D* 84 (2011), p. 123008. arXiv: 1109.2767.

[28]   A. D. Dolgov et al. In: *Nucl. Phys. B* 632 (2002), p. 363. arXiv: `hep-ph/0201287`.

[29]   R. Ichimasa et al. "Big-bang nucleosynthesis in comparison with observed helium and deuterium abundances: Possibility of a nonstandard model". In: *Phys. Rev. D* 90 (2014), p. 023527. DOI: `10.1103/PhysRevD.90.023527`.

[30]   F. Iocco et al. In: *Phys. Reports* 472 (2009), p. 1. arXiv: `0809.0631`.

[31]   R. I. Epstein, J. M. Lattimer, and D. N. Schramm. "The Origin of Deuterium". In: *Nature* 263 (1976), p. 198.

[32]   S. Riemer-Sørensen et al. "A precise deuterium abundance: Re-measurement of the z = 3.572 absorption system towards the quasar PKS1937â1009". In: (2016). Not yet published. Available upon request.

[33]   I. Dvorkin et al. In: *Monthly Notices of the Royal Astronomical Society: Letters* 458 (2016), p. L104. arXiv: `1602.04831`.

[34]   E. Aver, K. A. Olive, and E. D. Skillman. In: *Journal of Cosmology and Astroparticle Physics* 2015 (2015), p. 011. arXiv: `1503.08146`.

[35]   T.M. Bania, R.T. Rood, and D.S. Balser. In: *Nature* D415 (2002), p. 54.

[36]   E. Vangioni-Flam et al. In: *Astrophys. J.* 585 (2003), p. 611. arXiv: `astro-ph/0207583`.

[37]   F. Spite and M. Spite. In: *Astronomy and Astrophysics* 115 (1982), p. 357.

[38]   E. Vangioni-Flam et al. In: *New Astronomy* 4 (1999), p. 245. arXiv: `astro-ph/9811327`.

[39]   Richard H. Cyburt, Brian D. Fields, and Keith A. Olive. "Solar Neutrino Constraints on the BBN Production of Li". In: *Phys. Rev. D* 69 (2004), p. 123519. DOI: `10.1103/PhysRevD.69.123519`.

[40]   A. Coc and E. Vangioni. "Lithium and Big-Bang Nucleosynthesis". In: *From Lithium to Uranium: Elemental Tracers of Early Cosmic Evolution*. Vol. 1. Proceedings of the International Astronomical Union. 2005, p. 13.

[41]   B. D. Fields. In: *Ann. Rev. of Nucl. and Particle Science* 61 (2011), p. 47. arXiv: `1203.3551`.

[42]   A. Arbey. In: *Comput. Phys. Comm.* 183 (2012), p. 1822.

[43]   R.V. Wagoner. In: *Astrophys. J. Suppl.* 18 (1968).

[44]   L. Kawano. In: *FERMILAB-PUB-92-004-A* (1992).

[45]   O. Pisanti et al. In: *Comput. Phys. Commun.* 178 (2007), p. 956. arXiv: `0705.0290`.

[46]   L. Kawano. In: *FERMILAB-PUB-88/34-A* (1988).

[47]   R. V. Wagoner, W. A. Fowler, and F. Hoyle. In: *Astrophys. J.* 148 (1967), p. 3.

[48]   K. M. Nollett and G. Steigman. In: *Phys. Rev. D* 89 (2014), p. 083508. arXiv: `1312.5725`.

[49]   A. Arbey and F. Mahmoudi. In: *Physics Letters B* 669 (2008), p. 46. arXiv: `0803.0741`.

[50]   A. Arbey and F. Mahmoudi. In: *JHEP* 1005 (2010), p. 051. arXiv: `0906.0368`.

[51]   A. Arbey, A. Deandrea, and A. Tarhini. In: *JHEP* 1005 (2010), p. 078. arXiv: `1103.3244`.

[52]   S. Ando et al. In: *Phys. Rev. C* 74 (2006), p. 025809. arXiv: `nucl-th/0511074`.

[53]   S.Q. Hou et al. In: *ArXiv e-prints* (2015). arXiv: `1502.03961`.

[54]   R. H. Cyburt and B. Davids. In: *Phys. Rev. C* 78 (2008), p. 064614. DOI: `10.1103/PhysRevC.78.064614`.

[55]   A. Coc et al. In: *Phys. Rev. D* 92 (2015), p. 123526. arXiv: `1511.03843`.

[56]   P. D Serpico et al. In: *JCAP* D0412 (2004), p. 010. arXiv: `astro-ph/0408076`.

[57]   W. Digvijay. "AlterBBN Manual". Summer student report. Available upon request. 2014.

[58]   A. Arbey. Private e-mail correspondence. 2015.

[59]   R. H. Cyburt. In: *Phys. Rev. D* 70 (2004), p. 023505. arXiv: `astro-ph/0401091`.

[60]   A. Coc. Private e-mail correspondence.

[61]   M.S. Smith, L.H. Kawano, and R.A. Malaney. In: *Astrophys. J. Suppl.* 85 (1993), p. 219.

[62]   K. Enqvist, K. Kainulainen, and V. Semikoz. In: *Nucl. Phys. B* 374 (1992), p. 392.

[63]   D.R. Tilly, H.R. Weller, and H.H. Hasan. In: *Nucl. Phys. A* 474 (1987), p. 1.

[64]   F. Ajzenberg-Selove. In: *Nucl. Phys. A* 490 (1988), p. 1.

[65]   F. Ajzenberg-Selove. In: *Nucl. Phys. A* 506 (1990), p. 1.

[66]   F. Ajzenberg-Selove. In: *Nucl. Phys. A* 449 (1986), p. 1.

[67]   R.A. Malaney and W.A. Fowler. In: *Astrophys. J.* 345 (1989), p. 5.

[68]   G.R. Caughlan and W.A. Fowler. In: *Atomic data and nuclear data tables* 40 (1988), p. 291.

[69]   C. Angulo et al. In: *Nucl. Phys. A* 656 (1999), pp. 3–187.

[70]   M. Fukugita and T. Kajino. In: *Phys. Rev. D* 42 (1990), p. 4251.

[71]   D Thomas et al. In: *Astrophys. J.* 406 (1993), p. 569. arXiv: `astro-ph/9206002`.

[72]   F Iocco et al. In: *Phys. Rev. D* 75 (2007), p. 087304.

[73]   K. Garrett and G. Duda. In: *Adv. in Astronomy* 2011 (2011), p. 22. arXiv: `1006.2483`.

[74]   K. Freese. In: *EAS Publ. Series* 36 (2009), p. 113. arXiv: `0812.4005`.

[75]   J. R. Primack and M. A. K. Gross. "Current Aspects of Neutrino Physics". In: ed. by D. O. Caldwell. Springer Berlin Heidelberg, 2001. Chap. Hot Dark Matter in Cosmology, p. 287. arXiv: `astro-ph/0007165`.

[76]   K. Sigurdson. In: (2009). arXiv: `0912.2346`.

[77]   J. R. Primack. In: (1997). arXiv: `astro-ph/9707285`.

[78]   G. Bertone, D. Hooper, and J. Silk. In: *Physics Reports* 405 (2004), p. 279. arXiv: `hep-ph/0404175`.

[79]   C. et al. Alcock. In: *Astrophys. J. Lett.* 550 (2001), p. L169. arXiv: `astro-ph/0011506`.

[80]   J. Yoo, J. Chanamé, and A. Gould. In: *Astrophys. J.* 601 (2004), p. 311. arXiv: `astro-ph/0307437`.

[81]   Planck Collaboration. "Planck 2013 results XVI. Cosmological parameters". In: *A&A* 571 (2014), A16. arXiv: `1303.5076`.

[82]   C. Weinheimer. In: (2003). arXiv: `hep-ex/0306057`.

[83]   S. Dodelson and L. Widrow. In: *Phys. Rev. Lett.* 72 (1994), p. 17. arXiv: `hep-ph/9303287`.

[84]   I. J. R. Aitchison. In: (2005). arXiv: `hep-ph/0505105`.

[85]   P. Nath. In: (2015). arXiv: `1501.01679`.

[86]   P. Draper and H. Rzehak. In: (2016). arXiv: `1601.01890`.

[87]   K. Griest and M. Kamionkowski. In: *Phys. Rev. Lett.* 64 (1990), p. 15. DOI: `10.1103/PhysRevLett.64.615`.

[88]   P. Hut. In: *Phys. Rev. Lett. B* 69 (1977), p. 85.

[89]   B. W. Lee and S. Weinberg. In: *Phys. Rev. Lett.* 39 (1977), p. 165. DOI: `10.1103/PhysRevLett.39.165`.

[90]   C. Boehm and P. Fayet. In: *Nucl. Phys. B* 683 (2004), p. 219. arXiv: `hep-ph/0305261`.

[91]   Mikhail P. Solon. *Heavy WIMP Effective Theory: Formalism and Applications for Scattering on Nucleon Targets*. Springer International Publishing, 2015.

[92]   G. Mangano et al. In: *Nucl. Phys. B* 729 (2005), p. 221. arXiv: `hep-ph/0506164`.

[93]   C. B. Markwardt. In: vol. 411. ASPC. 2009, p. 251. arXiv: `0902.2850`.

[94]   D. C. Morton. In: vol. 149. ApJS. 2003, p. 205.

[95]   N. Crighton. *Barak's Documentation*. 2012. URL: `http://nhmc.github.io/Barak/`.

[96]   J. M. O'Meara et al. In: *The Astronomical Journal* 150 (2015), p. 111. arXiv: `1505.03529`.

[97]   J. A. King et al. In: *Monthly Notices of the Royal Astronomical Society* 422.4 (2012), p. 3370.

[98]   W. A. Fowler, G. R. Caughlan, and B. A. Zimmerman. In: *Annual Review of Astronomy and Astrophysics* 5 (1967), p. 525.

[99]   C. Iliadis. *Nuclear Physics of Stars*. 2008.

[100] S. Chandrasekhar. *An Introduction To The Study Of Stellar Structures*. 1939.